Emissions and Stability of Partially Cracked Ammonia Swirling Flames

Jordan Davies

A thesis submitted for the degree of:

Doctor of Philosophy in Mechanical Engineering

Cardiff University

August 2025

Abstract

Renewably produced ammonia is a potential carbon-free fuel as it features well-established global infrastructure for safe distribution, is easy to store as it liquefies at modest pressures and contains significant hydrogen content. However, effective combustion of ammonia faces challenges stemming from its low reactivity and narrow flame stability limits. This problem can be alleviated by partially cracking the molecule, resulting in a fuel blend of ammonia, hydrogen and nitrogen with much improved reactivity. Therefore, the last remaining challenge relates to mitigating its propensity for producing high NOx emissions. This study aims to reduce NOx emissions from partially cracked ammonia flames and understand how to maintain flame stability as thermal power is scaled up towards levels relevant to industrial systems.

To achieve this aim, a laboratory-scale atmospheric swirl burner is employed to assess NOx reduction methodologies such as fuel stratification, humidification and heat loss management. It is also used to evaluate a range of swirlers with varying swirl number and nozzle designs to identify desirable characteristics to mitigate against flame blowoff risk at elevated gas velocities. Experimental gas analysis and chemiluminescence imaging is used in parallel with chemical reactor network modelling to understand the reactions responsible for NOx reduction.

The key findings include that retaining the N_2 produced during the NH_3 cracking process in the fuel blend reduces NOx emissions compared to equivalent NH_3/H_2 flames. Fuel stratified swirl flames exhibited sensitivity to the diffusive equivalence ratio, with slightly lean central H_2 flames producing the lowest combined emissions. Compared to premixed, this case resulted in a 90% NO reduction and 33% NH_3 increase at Φ_G = 1.05. Humidification lowered NO emissions at fuel lean conditions by reducing HNO production by 29%, contributing to a 40% drop in peak NO, and at fuel rich conditions by supplying OH radicals for extra NH_2 formation, increasing NO consumption. It also reduced H_2 emissions at fuel rich conditions by up to 41%, likely due to lower post-flame temperatures reducing thermal cracking of NH_3 in the exhaust. Controlling temperatures by increasing heat loss to the burner face reduced NO emissions at Φ = 1.1 by 67% alongside an 11% increase in unburned NH_3 by shifting NH_2 reactivity closer to its temperature-dependent peak, increasing NO consumption. Shortening the nozzle increased blowoff resistance at 100 kW by widening the flame brush, a desirable characteristic for scaling these flames to higher thermal power applications. These findings advance the understanding of NOx reduction methodologies in partially cracked ammonia swirl flames and their effects on combustion efficiency, while also highlighting findings for scaling them to higher thermal powers.

Contents

Acknowledgements

First and foremost, I would like to thank Prof. Agustin Valera-Medina, Dr. Syed Mashruk and Dr Daniel Pugh for your invaluable guidance, teachings and the many stimulating conversations we've had which have helped shape my research. Your support has been instrumental to my development as a researcher.

I would like to extend my gratitude to Dr. Robin Irons and Dr. Claudia Matz for leading this excellent Centre for Doctoral Training, and to Gina for always being there to help. I'm also thankful to Reaction Engines for their sponsorship of this research project.

A big thank you to Malc and Jon for all the technical support and guidance in the lab. I've appreciated the opportunities to get stuck in and I've learned a lot from you both. Cheers for the help and for showing me the right way to do things.

To the friends I've made along the way, iechyd da! Robin, Elliott, Llywelyn, Ali, cheers for making this process an enjoyable one. I'm not sure we'd have all made it through the PhD without each other and the sanctuary of a certain small yet spirited place, but here we are. Daisuke, you've been a worthy ping pong adversary and our time at the table has definitely boosted my productivity. Thanks for all the hard work in the lab, I think we got plenty of results! Luca, thanks for visiting – it was a fun and fruitful three months.

Mum, dad and the brothers, who would have thought the FLTB would get this far? Thanks for sticking with me and being genuinely interested in my work.

Sarah – thank you for always being there for me. For your love and patience even through the late nights and for making me laugh when I needed it most.

Statement of Authorship of Publications

Article 1:

Experimental and Numerical Investigation of $NH_3/H_2/N_2$ Combustion in a Premixed/Stratified Swirl Burner.

Jordan Davies, Luca Mazzotta, Daisuke Sato, Syed Mashruk, Daniel Pugh, Domenico Borello, Agustin Valera-Medina.

Journal of Engineering for Gas Turbines and Power, Volume 147, 2024, 011006.

Publication status: published work, included with publisher's permission (CC-BY 4.0 Licence).

Presented as Chapter 3.

JD contribution: 80%

JD developed the methodology and conducted experiments with the assistance of DS and LM. DS and LM carried out the numerical work. JD led the investigation, curated and visualised the data and wrote the original draft. SM, DP and AVM reviewed the original draft and supervised.

Article 2:

Emissions Analyses of Humidified Cracked Ammonia Swirling Flames.

Jordan Davies, Syed Mashruk, Luca Mazzotta, Daisuke Sato, Daniel Pugh, Agustin Valera-Medina.

Combustion and Flame, Volume 274, 2025, 113984.

Publication status: published work, included with publisher's permission (Gold Open Access).

Presented as Chapter 4.

JD contribution: 70%

JD developed the methodology and conducted experiments with SM. LM and DS were also present for the experiments. JD led the investigation, curated and visualised the data and wrote the original draft. SM, DP and AVM reviewed the original draft and supervised.

Article 3:

Control of Emissions from Cracked Ammonia Swirling Flames by Heat Loss Management

Jordan Davies, Daisuke Sato, Syed Mashruk, Daniel Pugh, Agustin Valera-Medina.

International Journal of Hydrogen Energy, Volume 168, 2025, 151061.

Publication status: published work, included with publisher's permission (Gold Open Access).

Presented as Chapter 5

JD contribution: 80%

JD developed the methodology and conducted experiments with the assistance of DS. JD led the investigation, curated and visualised data and wrote the original draft. DS reviewed the draft. SM, DP and AVM reviewed the draft and supervised.

Article 4:

Experimental analysis of swirl number and nozzle design for scale-up of partially cracked ammonia flames

Jordan Davies, Daisuke Sato, Syed Mashruk, Agustin Valera-Medina.

Applications in Energy and Combustion Science, Volume 22, 2025, 100338.

Publication status: published work, included with publisher's permission (Gold Open Access).

Presented as Chapter 6

JD contribution: 80%

JD developed the methodology and conducted experiments with the assistance of DS. JD led the investigation, curated and visualised data and wrote the original draft. DS reviewed the draft. SM and AVM reviewed the draft and supervised.

Co-Authored Publications:

1. Sato D, **Davies J**, Mazzotta L, Mashruk S, Valera-Medina A, Kurose R. Effects of Reynolds number and ammonia fraction on combustion characteristics of premixed ammonia-hydrogen-air swirling flames. *Proceedings of the Combustion Institute* 40 (2024) 105283.

2. Mazzotta L, Zhu X, **Davies J**, Sato D, Borello D, Mashruk S, Guiberti TF, Valera-Medina A. Assessing the potential of chemiluminescence and machine learning-based method for the sensing of premixed ammonia-hydrogen-air turbulent flames. *International Journal of Hydrogen Energy* 100 (2025) 945-954.

3. Vigueras-Zuniga MO, Tejeda del Cueto ME, **Davies J**, Mashruk S, Valera-Medina A. Analysis of excited species formation across the flame of various ammonia-hydrogen fired combustor geometries. *Energy Technology* 13 (2025) 2401404.

4. Agwu N, **Davies J**, Sato D, Mashruk S, Valera-Medina A. Machine learning driven chemiluminescence-based modelling of combustion parameters in premixed swirling NH_3/H_2 flames. *International Journal of Hydrogen Energy* 145 (2025) 717-731.

5. Sato D, **Davies J**, Lee S, Mashruk S, Valera-Medina A, Kurose R. Radiative characteristics of premixed coke oven gas-ammonia swirling flames. *Fuel* 401 (2025) 135741

6. B Aravind, Sadasivam S, **Davies J**, Mashruk S, Valera-Medina A. Experimental demonstration of in-situ cracked premixed NH_3-air flames. *Applied Energy* 401 (2025) 126754.

7. Sato D, **Davies J**, Lee S, Mashruk S, Valera-Medina A, Kurose R. Combustion and emission characteristics of premixed coke oven gas-ammonia swirling flames. *Fuel* 406 (2026) 137001.

8. Sato D, **Davies J**, Mashruk S, Valera-Medina A, Kurose R. Radiative characteristics of premixed ammonia-hydrogen and cracked ammonia swirling flames. Under review for *Applications in Energy and Combustion Science*.

1. Introduction

1.1. Climate Change and the Energy Landscape

Global anthropogenic emissions of greenhouse gasses (GHGs) are at an all-time high, largely from the burning of fossil fuels [1]. This has led to an increase in global surface temperature via the greenhouse effect, resulting in more frequent extreme weather events, droughts and famine. The impacts on the environment and human health are widespread and there is high confidence human systems have already been pushed beyond their ability to adapt [2]. Therefore, it is necessary to decarbonise systems reliant on fossil fuels.

As part of the 2015 United Nations Paris Agreement, nearly all countries have agreed to reduce greenhouse gas emissions to limit global temperature increases to less than 2°C above pre-industrial levels, and ideally to less than 1.5°C [3]. More specifically, the UK has committed to a 68% reduction in emissions by 2030 and to reaching net zero emissions by 2050 [4].

In the UK, Fig. 1.1 [5] shows CO_2 equivalent emissions have been falling steadily over the last 30 years. The most significant reduction has been in electricity supply with a near 80% reduction since 1990. However, other sectors such as industry have seen relatively little reduction in the last 10 years, suggesting more work is needed to tackle these hard-to-abate sectors, which often have high temperature requirements difficult to reach solely with electrification. It is worth noting that a significant portion of the UK's carbon emissions over this period have been offshored by industrial migration. One report [6] suggests as much as 46% of the UK's carbon footprint – driven by manufacturing and services – comes from abroad.

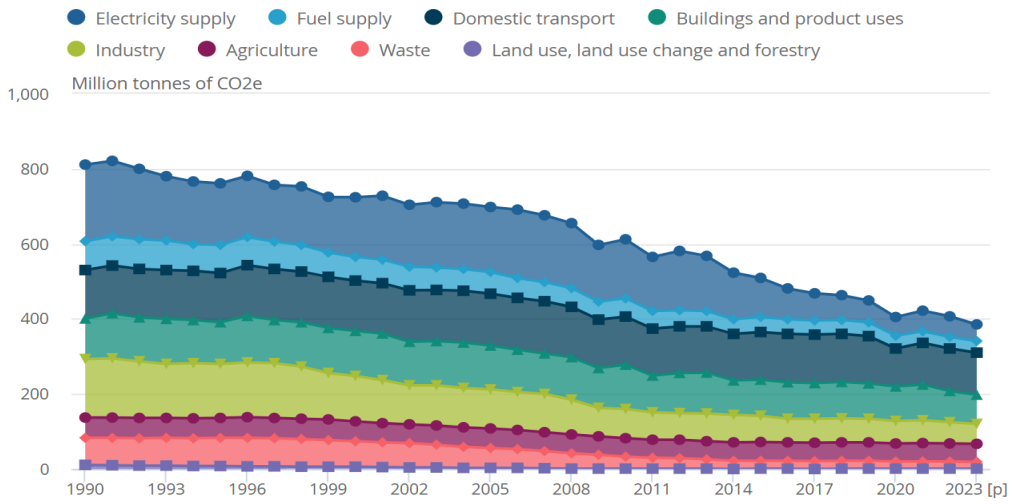

Fig. 1.1: UK CO_2e emissions by sector, reproduced from [5].

1.2. Renewable Intermittency

In 2024, the UK's 142-year dependence on coal powered electricity generation ended. The phase-out of electricity generation from coal has largely been replaced by wind, biomass and solar, as can be seen in Fig. 1.2 [7]. However, the UK's largest single electricity source is still from the combustion of natural gas in gas turbine power stations, and the current amount of electricity generated by gas turbines is not significantly lower than it was in 2012.

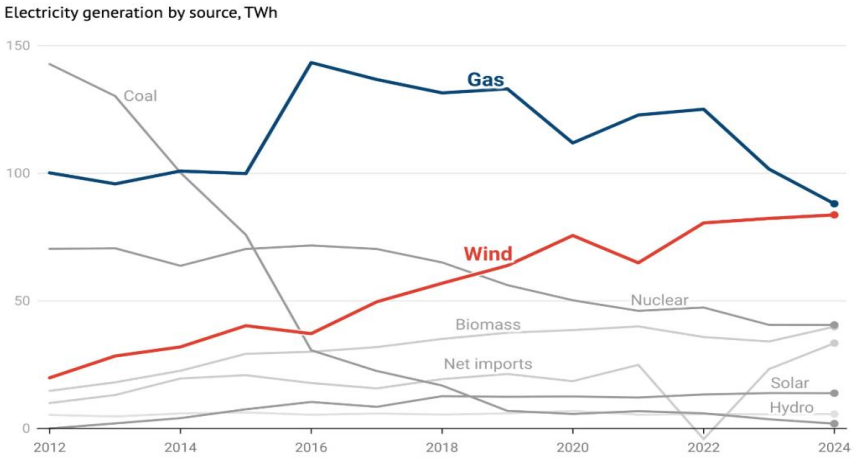

Fig. 1.2: UK electricity generation by source, TWh, 2012-2024. Reproduced from [7]

The intermittency of renewable sources such as wind and solar remains a significant issue to be solved for the UK's electrical grid to be further decarbonised. Wind intermittency is highlighted in Fig. 1.3 [8], which shows that while power output from wind had rapidly increased since 2005, capacity factors have generally remained near 40%. This highlights the key temporal distinction between energy and dispatchability in renewables – they can provide substantial energy over time but cannot always deliver dispatchable power precisely as demand occurs and are therefore considered intermittent electricity sources.

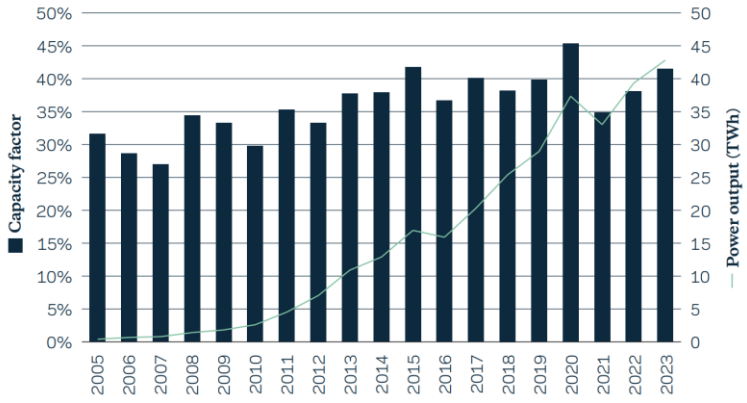

Fig. 1.3: England and Wales offshore wind capacity factor. Reproduced from [8]

Nuclear power stations in the UK are used to supply baseload electricity to the National Grid. These stations generally operate at steady, full power and do not operate flexibly to match instantaneous demand. Power is only reduced or shut down when refuelling, to carry out maintenance or for unexpected safety constraints [9]. Historically, this has been useful – the Grid operators usually know how much power they will be receiving at any one time and can plan accordingly. Compared to gas fired power stations, nuclear is much worse at matching instantaneous demand [10]. Therefore, if wind were to supply most of the electricity to the grid, nuclear power stations are not flexible enough to match sudden changes in electricity demand – such as morning and evening peaks – if electricity supply from wind happened to be lower than expected due to changes in weather, for example. This highlights that although wind turbines offer excellent decarbonisation benefits, an electrical grid will struggle with intermittency issues if it is too reliant on them.

To overcome the issue of intermittency, energy storage and dispatchable power are required. One option is pumped hydroelectric energy storage (PHES), where excess/cheap electricity is used to pump water uphill into a reservoir, increasing potential energy. Then, when demand is high, the water can be released back down through a turbine, converting the stored potential energy into electrical energy with a quick response time. The UK currently operates four such PHES sites. However, future PHES sites in the UK face challenges relating to public opposition, significant land area requirements, geological constraints and payback times being considered too long to justify significant investment [11]. Another option is to replace PHES sites with grid-level battery energy storage systems (BESS) operating on the same principle of supporting wind or solar's intermittency issues. However, recent studies highlight challenges relating to economic feasibility [12].

A third option is chemical storage. In the short-medium term, blue hydrogen from steam methane reforming with carbon capture could be viable. Longer term, green hydrogen produced from electrolysis of water with renewably produced electricity from excess wind power when supply is high and demand is low could be considered an ideal solution. This would enable the continued use of gas turbines to provide electricity when wind supply is low or at peak demand times without any carbon emissions. However, hydrogen is difficult and costly to store, requiring pressurisation to 700 bar or cryogenic cooling to -253°C [13]. Ammonia on the other hand is a hydrogen carrier which can be produced by combining hydrogen with nitrogen, a gas abundant in the air. It can also be liquefied at just 8-10 bar pressure or with cooling to -33°C. Liquid ammonia has a higher hydrogen density at 120 kg-H_2/m^3 than liquid hydrogen at 70.8 kg-H_2/m^3 [14]. As a result, liquid ammonia also has a higher volumetric energy density than pure hydrogen, further

reducing transportation costs. Compared to ammonia, hydrogen has a higher leakage risk due to its high diffusivity and small molecular size. After leakage, hydrogen has significantly wider explosive limits of 4-75 % (vol.) in air, compared to 16-25 % for ammonia and lower ignition energy [15]. Furthermore, hydrogen flames offer little visible emission unless at reduced light levels [16] representing a larger safety risk compared to ammonia flames which are easily visible in daylight, with broadband emission and particularly high intensity in the yellow-orange range [17]. Furthermore, leak detection is made more difficult for hydrogen as it is an odourless gas whereas ammonia has a pungent odour which can be detected by smell at just 2.6 ppmv [18]. Despite ammonia being a toxic and corrosive substance, it is already handled in a mature, global infrastructure of storage and transportation with well-established safety management systems, which are still in development for pure hydrogen [19]. The combustion of ammonia in gas turbines can therefore support and accelerate the deployment of renewable energy sources such as wind turbines. Furthermore, green ammonia can be combusted in industry and other hard-to-abate sectors, which is something that pure electricity options such as PHES and BESS cannot always be used for. Ammonia can also be considered directly as an energy vector, to move decarbonised energy from where it is produced to where it is used. For example, this could be moving energy from renewable rich regions such as Australia, Chile, Northern Africa and the Middle East to industrial demand centres such as East Asia, North America and Europe.

In terms of the energy trilemma – which balances the challenges of energy sustainability, affordability and security – green ammonia has the potential to assist renewable energy in managing all three issues. Reducing reliance on fossil fuel consumption assists with energy sustainability. Using green ammonia production to increase capacity factors of wind turbines when demand is low and supply is high can further reduce the cost of renewable energy. Additionally, this would reduce exposure to the volatile global natural gas markets, potentially improving energy affordability, as well as security – particularly considering geo-political events such as the Russo-Ukrainian war.

1.3. Ammonia: Production, Storage, Use and Combustion

1.3.1. Production

In 2020, global ammonia production reached 184 million tonnes, responsible for 1.3% of global CO_2 emissions [20]. The majority of this ammonia was produced by combining hydrogen and nitrogen in the high temperature and pressure of 450-650 °C and 100-400 bar Haber-Bosch process. The hydrogen feedstock for this process is mostly produced via steam-methane

reforming with some coal gasification, which is carbon intensive. The nitrogen is separated from atmospheric air by cryogenic fractional distillation. This is not a green or renewable process and ammonia production is currently responsible for 450 million tonnes of CO_2 equivalent emissions annually [20]. Ammonia produced via this traditional process is referred to as grey ammonia and as it is not produced from renewable sources, cannot be considered a renewable fuel.

However, significant research is being undertaken to decarbonise ammonia production. In terms of producing green ammonia from renewable electricity, the Haber-Bosch and air separation processes count for 5% of the electricity consumption, while producing green hydrogen via water electrolysis counts for 95% [20]. Although hydrogen production via water electrolysis utilising renewably produced electricity is a mature process, the cost is currently prohibitively high compared to traditional steam-methane reforming. However, the IEA predicts green hydrogen production cost per kg to halve in the next five years, reducing the cost gap to unabated steam-methane reforming and to continue dropping towards 2050 [21]. Novel ammonia production processes to replace Haber-Bosch with less energy intensive methodologies include electrosynthesis at ambient pressures and temperatures [22]. While rapidly advancing, such processes are currently at low technology readiness levels. Nonetheless, the IEA expects ammonia production to increase to 253 million tonnes while reducing CO_2 emissions by between 78% and 96% by 2050, largely depending on electrolysis and carbon capture routes [20].

1.3.2. Storage and Transportation

There exists a global network for production, transportation and storage of ammonia already due to its global utilisation in fertilisation and chemical production. With it comes a global expertise in safe handling of ammonia, with few safety incidents in developed countries with strong government regulation and safety infrastructure [23]. Compared to pure hydrogen, these already developed networks and safety expertise present a significant advantage and significant capital investment saving.

It is moderately easy – notwithstanding toxicity issues – to store and transport ammonia due to its ease of liquification under modest conditions of pressurisation to 10 bar at atmospheric temperatures or refrigeration to -33 °C at atmospheric pressure. This represents significantly lower energy and hence economic costs to achieve and maintain liquification compared to hydrogen being pressurised to 700 bar or refrigerated to -253 °C. Liquid ammonia tanks are also significantly lighter than high pressure hydrogen tanks, further reducing transportation costs. This is shown in Fig. 1.4, which presents the lower and higher heating values of liquid NH_3 and H_2 when

the storage tank weight and volume is considered [24]. It shows that up to 1000kg tank weight, ammonia has a gravimetric LHV of more than double that of hydrogen. Only the very largest tanks of more than 20,000 kg reach energy density parity. In volumetric terms, the difference is even greater.

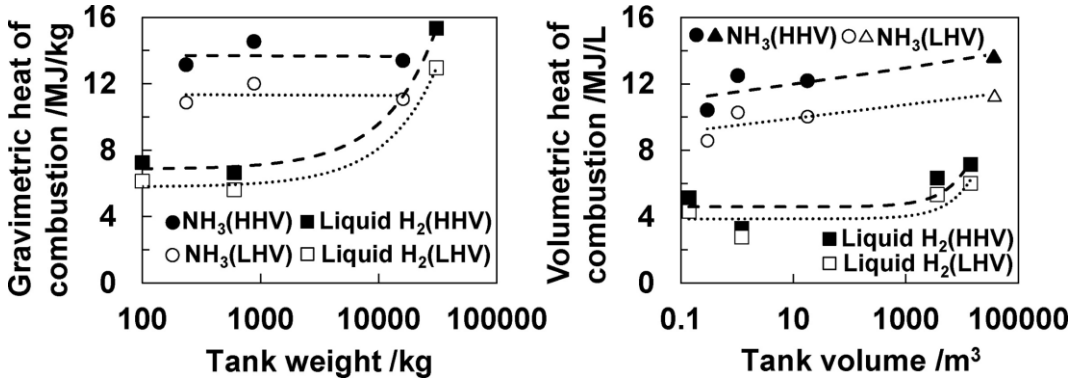

Fig. 1.4: Gravimetric and volumetric heating values of liquid NH_3 and H_2 (including storage tank). Reproduced from [24].

1.3.3. Current Utilisation and Development

Currently, 70% of ammonia produced globally is used for producing fertiliser products [20]. The remainder is used for industrial applications such as plastics, explosives and chemical production feedstock. It is also still used as a refrigerant and in exhaust gas treatment for NOx abatement. The latter can be performed with or without a catalyst – selective catalytic reduction (SCR) and selective non-catalytic reduction (SNCR), respectively. Ammonia is injected into the exhaust gas after the combustion process to reduce NOx to nitrogen and water. SNCR requires relatively high temperatures and is most efficient in a narrow temperature band of 850-1050 °C [25,26], as shown in Fig. 1.5. Use of a catalyst reduces required operating temperatures but increases cost.

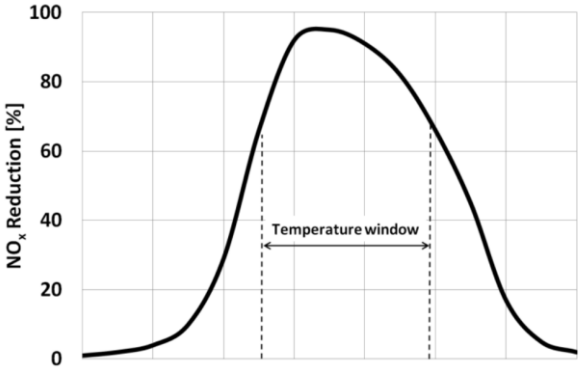

Fig. 1.5: SNCR NOx reduction as a function of temperature. Reproduced from [26].

Ammonia usage by sector is expected to undergo radical change over the coming decades. As shown in Fig. 1.6, existing utilisation – mainly as a fertiliser – is forecast to slightly increase by 2050. However, total utilisation is set to increase significantly by 2050, with demand for use as a maritime fuel expected to reach parity with current total usage, while demand for power generation is projected to reach one quarter of current total usage [20].

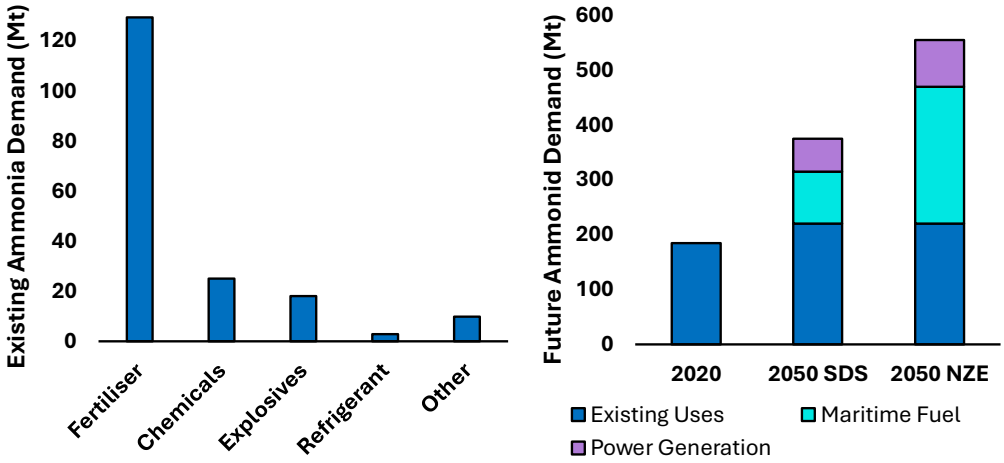

Fig. 1.6: Current (left) and predicted future (right) ammonia utilisation by sector. Reproduced from [20].

The increase in demand for ammonia as a maritime fuel is driven by the development of ammonia-fuelled internal combustion engines (ICE) by leading manufacturers such as Wärtsilä and MAN. Wärtsilä have recently announced the commercial availability of a medium size four-stroke dual-fuel marine ICE operating on diesel/ammonia blends at up to 3.4MW thermal power [27]. Although the engine does not operate on pure ammonia, Wärtsilä promise a 70% reduction in CO_2 emissions and compliance with regulatory limits of NOx emissions with the assistance of an after-treatment system. MAN is developing a two-stroke dual-fuel ammonia engine, also targeting a 70% reduction in CO_2 emissions and NOx emission compliance with the use of an SCR based after-treatment system, with the first commercial engine reaching the testbed in 2025 [28]. Both manufacturers highlight the ease of storage as a driver for development, along with reduced CO_2, SOx and particulate emissions.

A large part of the increase in demand for ammonia as a power generation fuel is driven by companies and governments in Asia. IHI Corporation is developing several industrial-scale combustion systems operating on ammonia. Working closely with JERA, a Japanese power company, IHI demonstrated a 1 GW coal boiler operating on a dual fuel blend with 20 % ammonia substitution, based on higher heating value (HHV) utilising staged air injection. Reliable combustion was achieved throughout a three-month trial in 2024 [29]. No increase in NOx emissions were found, compared to full coal combustion. IHI and JERA are targeting 50 % ammonia substitution by 2030. A single 1 GW coal boiler operating with 50 % ammonia

substitution would consume more ammonia than the entire current demand of Japan, underlining the significant increase in ammonia demand shown in Fig. 1.6. Additionally, in partnership with GE Vernova, IHI are currently testing a 2 MW gas turbine combustor burning pure ammonia, also with an air staged combustion regime to reduce NO emissions [29]. These demonstrations represent the largest ammonia combustion tests to date. In Korea, KOSPO has recently begun construction of an ammonia import terminal at one of their coal fire power stations, also targeting 20 % ammonia substitution in one of the 1 GW boilers by 2028 [30]. It is worth noting that these are all either maritime or heavy industry projects, with few projects targeting medium-sized industrial steam boilers or furnaces. This gap therefore warrants targeted research.

1.3.4. Cracking

A point of note in Section 1.3.3 is that few large-scale projects currently under development are operating on pure ammonia. This is because it can be difficult to combust compared to conventional hydrocarbon fuels with high ignition energy, low flame speed and narrow stability limits, meaning it is not suitable for all combustion processes directly [31]. However, these challenges can be mitigated with the use of hydrogen fuel blending, widening the applicability of ammonia-based flames. This is convenient due to the presence of hydrogen within the ammonia molecule. Therefore, a potentially useful process is the thermo-catalytic decomposition – or cracking – of ammonia into its constituent atoms, hydrogen and nitrogen. This is particularly beneficial if waste heat is recovered from the combustion system and used for the cracking process. The catalytic reaction for cracking ammonia shown in Equation (1-1) is endothermic and temperature dependent, as shown in Fig. 1.7. When only partial cracking or dissociation is achieved, the cracking fraction, Cr, can be defined as in Equation (1-2).

$$2NH_3 \leftrightarrow N_2 + 3H_2;\ \Delta H = 46.19\ \text{kJ/mol} \qquad (1\text{-}1)$$

$$Cr = \frac{2X_{H_2}}{3X_{NH_3} + 2X_{H_2}} \qquad (1\text{-}2)$$

Cracking performance is depended on the selected catalyst. Ruthenium-based catalysts are conventionally considered optimal, with a decomposition-temperature curve close to that shown in Fig. 1.7, but have high capital costs due to ruthenium's scarcity. Iron-based catalysts are the most affordable, but offer poor performance, requiring temperatures above 600°C for efficient cracking [32]. State-of-the-art research into lower cost catalysts has identified high-entropy

alloys of cobalt and molybdenum as both more affordable and more efficient than ruthenium-based catalysts [32].

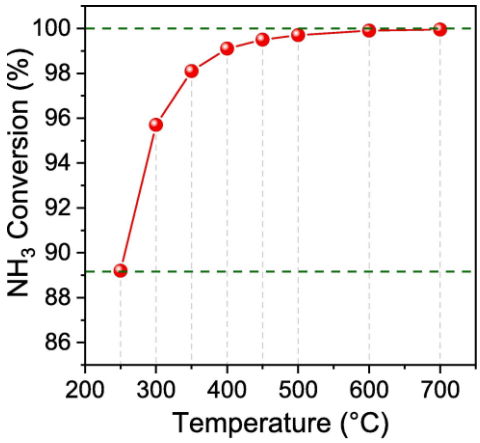

Fig. 1.7: Thermodynamic decomposition of NH_3 against temperature. Reproduced from [32].

Historically, research into ammonia cracking has targeted full conversion of ammonia into high purity hydrogen and nitrogen, with a view to reduce the transportation and storage costs associated with pure hydrogen [33,34]. Trace amounts of ammonia remaining are considered problematic and purification technologies are not yet mature, representing a significant barrier to deployment [35]. However, if only partial cracking is desired, temperatures can be lower, and purification is not required. This opens the door to combustion of partially cracked ammonia, potentially utilising waste heat from the combustion process. Furthermore, only partially cracking opens the door to using iron as a catalyst which is convenient as it is already present in the steel the cracking system would likely be manufactured from, effectively removing catalyst concerns.

1.4. Thesis Aims and Objectives

Renewably produced ammonia has the potential to aid in decarbonising electricity and heat production, particularly if partial cracking with integrated heat recovery is used. Ammonia's advantages over pure hydrogen include ease of storage and transportation via existing global infrastructure and long-established safety expertise. The remaining challenges to be solved relate to NOx emissions and flame stability.

The aim of this thesis is to support the utilisation of ammonia as a fuel by investigating methodologies to reduce NOx emissions from swirl burners while ensuring flame stability.

To meet this aim, the following objectives had to be met:

1. Determine whether the nitrogen remnant from the cracking process has an adverse effect on emissions to inform whether it should be removed.
2. Identify optimal equivalence ratios for combustion of partially cracked ammonia blends through experimental investigation.
3. Experimentally investigate methodologies to reduce emissions of NOx from partially cracked ammonia swirl flames such as fuel stratification, humidification and heat loss management. Quantify the resultant impact these methodologies have on emissions of unburned fuel.
4. Using chemical reactor networks, explore the chemical reactions responsible for the reduction of NOx from the above methodologies.
5. Experimentally investigate how variations in swirler and nozzle geometry influence flame structure and blowoff limits to determine desirable characteristics for scaling up partially cracked ammonia flames to thermal powers relevant to industry (100-1000 kW).

1.5. Thesis Structure

The structure of this thesis differs from a traditional thesis as it is a thesis with publication, where published papers accompanied by additional commentary are stylistically integrated into the thesis in place of traditional thesis chapters. The thesis first provides motivation and background for the present work in Chapter 1. Chapter 2 is a literature review which covers the fundamentals of swirl stabilised combustion, the effect of fuel blending on ammonia combustion, the basics of ammonia oxidation chemical kinetics, as well as existing research on methodologies to reduce NOx emissions from ammonia-based flames. Then, a series of paper-chapters are presented, mirroring the author's published journal papers but with additional commentary in the form of a preface to contextualise and integrate each paper into the thesis. Chapter 3 is dedicated to investigating the effect of fuel stratification on emissions and flame stability from partially cracked ammonia flames. Chapter 4 provides a study into steam injection – or humidification – of partially cracked ammonia swirl flames and outlines the reasons for the changes in emissions found. Chapter 5 examines a methodology for controlling emissions from partially cracked ammonia flames by managing heat loss to improve efficiency of NH_2 consumption of NO. Chapter 6 turns towards facilitating the scale-up of partially cracked ammonia flames by investigating the effect of swirl number and nozzle design on flame morphology as thermal power is increased. Finally, Chapter 7 is a concluding discussion which ties the thesis together and provides an evaluation of findings and recommends future works.

2. Literature Review

2.1. Swirl Combustion

2.1.1. Stabilisation Mechanism

Swirling flows for the stabilisation of combustion processes have been used commonly for decades [36]. Flame stabilisation is achieved due to the formation of highly turbulent recirculation zones which increase residence time, improve mixing, recycle heat and shorten flame length. Swirling flows vastly widen stability limits, particularly increasing blow-off resistance by enhancing turbulent flame speed which is of great use when utilising difficult to combust fuels [36].

A conceptual drawing of the flow field within a swirl burner from Strakey et al. [37] is shown in Fig. 2.1. The flame stabilises in the low velocity shear layers between a central recirculation zone (CRZ) and an external recirculation zone (ERZ), also referred to as a corner or outer recirculation zone. The CRZ is the primary stabilisation mechanism and is formed as a result of vortex breakdown. Vortex rollup from the end of the bluff body – or centre body – also contributes to strengthening the CRZ. The formation of the ERZ is a result of the area expansion from the dump plane to the larger combustion chamber and additionally stabilises the flame [38].

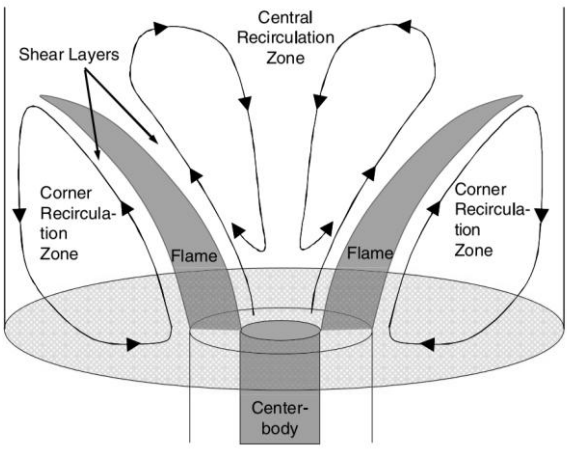

Fig. 2.1: Example of flow structures for a swirl flame. Reproduced from [37].

A swirler can be characterised by its non-dimensional swirl number, S, defined as the ratio of angular momentum flux to product of axial momentum flux and the exit radius, R, as shown in Equation (*2-1*).

$$S = \frac{angular\ momentum\ flux}{R * axial\ momentum\ flux} \tag{2-1}$$

A tangential swirler can also be characterised by a simple geometric swirl number, Sg. The geometric swirl number is based solely on the geometric dimensions of the swirler, as shown in Equation (*2-2*) for a tangential swirler, reproduced from [39].

$$Sg = \frac{\pi R R_{eff}}{A_t} \tag{2-2}$$

Where R is the exit radius, R_{eff} is the radial distance between a tangential channel axis and the injector axis and A_t is the total cross-sectional area of the tangential channels.

2.1.2. Blowoff and Flashback

In the simple case of a duct of a Bunsen burner, premixed flammability limits are dependent on gas velocity and burning velocity of the fuel. If the burning velocity is greater than the gas velocity, flashback can occur, with the flame front propagating upstream into the fresh gasses. Similarly, if the burning velocity is less than the gas velocity, blowoff can occur, with the flame front propagating downstream until the flame is lost [40]. Swirl burners enhance turbulent burning velocity, hence reducing propensity for blowoff, however their effect on flashback is more complex.

Flashback in swirl burners can be caused by a number of phenomena. It can occur in the low velocity boundary layer, by turbulent flame propagation into the core flow, by combustion instabilities or by combustion induced vortex breakdown [41]. Fuels with higher burning velocities are more susceptible to flashback, but changing swirl number can assist in managing flashback of different fuels. Fig. 2.2 demonstrates two different phenomena of flashback with different swirl numbers [42] for methane. The photo on the left shows combustion induced vortex breakdown, where the CRZ and hence flame propagate upstream into the premixing zone, here resulting in the flame stabilising within the nozzle attached to the baseplate of the swirler before flashing back radially through the swirler into the premixing chamber. This flashback mechanism only occurred at the relatively high swirl number of 1.47. At lower swirl numbers of 1.04 and 0.8, flashback occurred via the boundary layer in the outer wall, shown in the right photo.

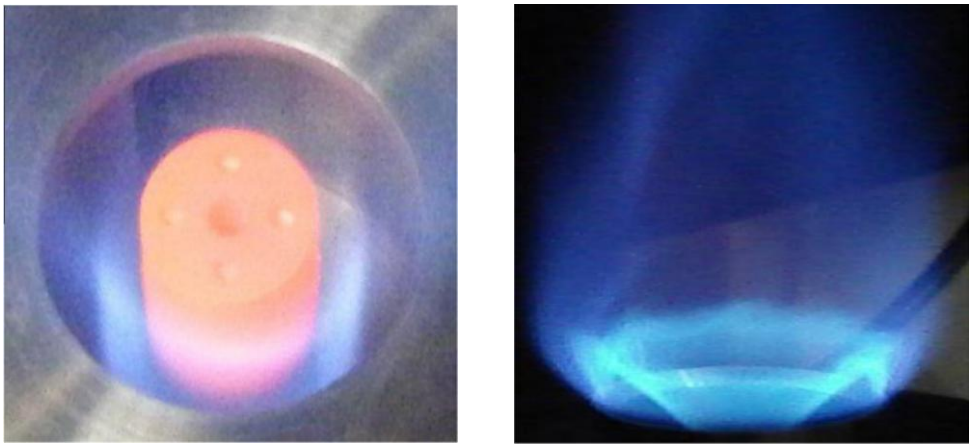

Fig. 2.2: Photo of flame (Sg = 1.47) stabilising in nozzle immediately prior to radial flashback (left). Photo of flame (Sg = 1.04) immediately prior to outer wall boundary layer flashback (right). Reproduced from [42].

2.2. Fundamentals of Ammonia Combustion and Fuel Blending

The reaction for the complete ideal combustion of ammonia in oxygen can be seen in Equation (2-3) below. As no carbon is present in the fuel, no carbon dioxide can be produced during combustion. Additionally, as discussed in Section 1.3.1, if it is produced via renewable processes, the combustion of ammonia can be considered green. However, this idealised reaction considers all intermediary NO, NO_2 or N_2O produced during combustion fully reducing to nitrogen and water. As to be discussed in the following sections, this is not necessarily true and achieving this is one of the major challenges remaining relating to ammonia combustion.

$$4\,NH_3 + 3\,O_2 \leftrightarrow 2\,N_2 + 6\,H_2O \qquad (2\text{-}3)$$

Equation (2-3) can be used to calculate the required air-fuel ratio (AFR) for complete (stoichiometric) combustion. The actual AFR can then be normalised to the stoichiometric AFR. This is referred to as the equivalence ratio (Φ), shown in Equation (2-4). When Φ is less than 1, the actual AFR is greater than the stoichiometric AFR and the flame is fuel lean with excess oxygen. Inversely, when Φ is greater than 1, the actual AFR is lower than the stoichiometric AFR and the flame is fuel rich, with less oxygen than required for complete combustion, resulting in fuel slip.

$$\phi = \frac{AFR_{stoichiometric}}{AFR_{actual}} \qquad (2\text{-}4)$$

Ammonia and hydrogen possess markedly different properties relating to combustion compared to fossil fuels such as methane and propane. Some of these properties are shown in Table 2-1. On both a mass and volumetric basis, ammonia's lower heating value (LHV) is significantly lower than those of the hydrocarbon fuels, suggesting higher flowrates into the combustor will be

required for the same heat output. On a mass basis, hydrogen has a high LHV, more than double those of the hydrocarbon fuels, but due to its low density, the volumetric LHV is even lower than ammonia's. In terms of autoignition temperature and ignition energy, ammonia is clearly difficult to ignite compared to hydrocarbon fuels, while hydrogen is easy. For ammonia, this can be considered a combustion challenge but a safety benefit, with the opposite being true for hydrogen.

In terms of adiabatic flame temperature (AFT) in air at stoichiometry, ammonia's is lower than hydrocarbon fuels while hydrogen's is higher. However, ammonia's AFT is not so low that it is not suitable for high-grade heat applications, particularly when a combustion process's operating equivalence ratio (Φ) is considered. The low laminar flame speed of ammonia – approximately 17% that of the hydrocarbon fuels – represents one of the key challenges with the combustion of pure ammonia. Care must be taken to design combustors to allow lower inlet velocities to prevent flame blowoff. It is therefore likely that existing combustors operating on hydrocarbon fuels will only be able to support pure ammonia flames with lower thermal powers where the gas inlet velocity is lower. Conversely, pure hydrogen has a laminar flame speed almost an order of magnitude larger than that of hydrocarbon fuels, presenting the opposite issue of flashback in existing combustors.

Table 2-1: Thermal and fundamental combustion properties of ammonia and hydrogen compared to hydrocarbon fuels at 298 K and 1 atm. Volumetric lower heating value and minimum ignition energy from [43], remainder from [31].

Property	Methane	Propane	Ammonia	Hydrogen
Lower Heating Value (MJ/kg)	50.0	46.3	18.6	120.0
Lower Heating Value (MJ/m^3)	35.8	91.2	14.1	10.8
Density at NTP (kg/m^3)	0.67	1.88	0.72	0.08
Minimum Autoignition Temperature (K)	903	723	923	793
Minimum Ignition Energy (mJ)	0.21-0.30	0.25-0.27	680	0.011-0.017
Maximum Adiabatic Flame Temperature (K)	2223	2273	2073	2383
Maximum Laminar Flame Speed (m/s)	0.37	0.43	0.07	2.91

Beyond flame stabilisation difficulties stemming from low flame speeds, the other major challenge with the combustion of ammonia is potentially high fuel NOx and N_2O emissions due to the presence of atomic nitrogen. The ideal final products of ammonia combustion are only molecular nitrogen and water, although more research is required to realise this in practical systems.

2.2.1. Pure Ammonia

As shown in Table 2-1, pure ammonia requires high temperatures and energy to ignite, burns slowly and at lower temperatures than fossil fuels or pure hydrogen. These factors make for a fuel which is challenging to utilise. Nonetheless, its ease of storage and transportation identified ammonia as an attractive fuel as far back as the 1960s [44]. The main findings of the early studies outlined high ignition energy and quenching distance, as well as low burning velocity causing a propensity for flame blowoff and generally narrow stability limits in terms of equivalence ratio.

Fig. 2.3 below shows an assortment of experimental measurements of laminar flame speed for ammonia/air flames at atmospheric conditions [45]. This plot also highlights the narrow stability limits, with no data available at equivalence ratios less than 0.7. The majority of studies do not provide data above an equivalence ratio of 1.3, suggesting rich stability limits are narrow or potentially dependent on experimental configuration.

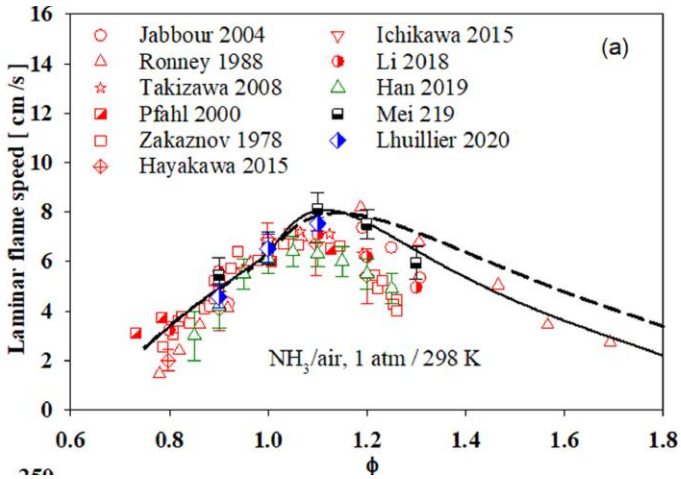

Fig. 2.3: NH_3/air laminar flame speed at atmospheric temperature and pressure. Reproduced from [45].

Beyond fundamental studies, ammonia-fired swirl burners saw renewed interest from the mid-2010s. Kurata et al. from AIST in Japan demonstrated a pure ammonia swirl flame in an unmodified kerosene micro gas turbine in 2017 [46]. The micro gas turbine featured a non-premixed axial swirl burner with swirl number of 0.88. A stable flame was demonstrated for a range of powers from 18.4 kW to 44.4 kW but with potentially poor mixing causing elevated NO and NH_3 emissions. Stability limits were widened when the inlet temperature was increased, likely because of increased flame speed. A later study using a similar combustor examined emissions from premixed ammonia/air flames more closely [47]. As shown in Fig. 2.4, NO emissions peaked at approximately 2500 ppm at slightly lean conditions of Φ = 0.9 and approached negligible values at slightly rich conditions of Φ = 1.1 – 1.2. Additionally, below Φ = 0.9, N_2O emissions began to increase with excess air. Emissions of unburned NH_3 and H_2 both rapidly increased above stoichiometry, reaching 2000 ppm and 4%, respectively at Φ = 1.2. An

equivalence ratio between Φ = 1.0 and 1.1 could be considered optimal, as it presents the lowest simultaneous total emissions.

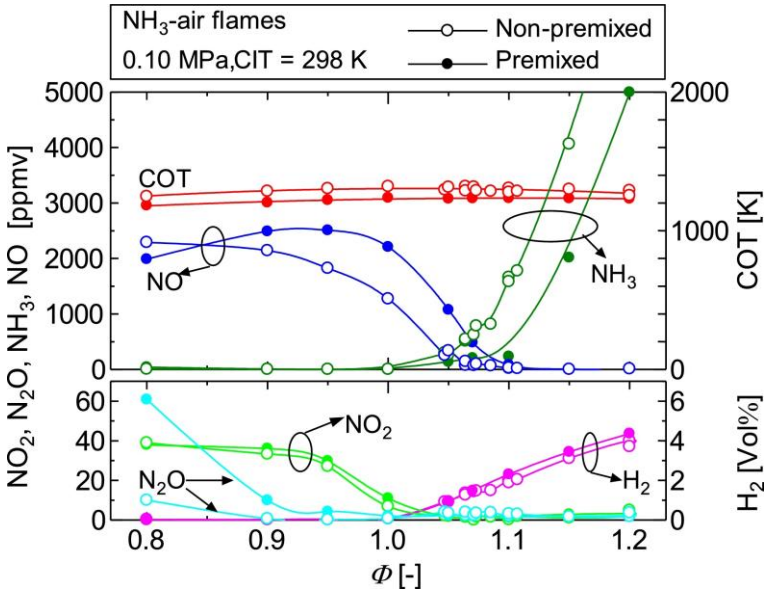

Fig. 2.4: Emissions of NO, NO_2, N_2O, NH_3 and H_2 against equivalence ratio for pure ammonia/air flames. Reproduced from [47].

A 2015 study from Tohoku University demonstrated pure ammonia premixed flames using two axial swirlers, with swirl numbers of 0.736 and 1.270 [48]. A broad range of equivalence ratios from 0.65 to 1.3 were stabilised at relatively low inlet velocities of 2-8 m/s and a potentially optimal equivalence ratio of 1.05 was identified with simultaneously low NO and unburned NH_3 of the order of several hundred ppm each. As can be seen in Fig. 2.5, the flame morphology of ammonia flames is markedly different to methane flames, with the most obvious difference being the flame colour. The yellow-orange colour of the pure ammonia flames can be attributed mainly to NH_2* chemiluminescence with some NO_2* at very lean conditions [49]. The methane flame however appears blue, with the chemiluminescence spectra in the visible wavelength range being dominated by CH* [50]. The other significant difference is that the ammonia flame is notably longer, as a result of its lower burning velocity.

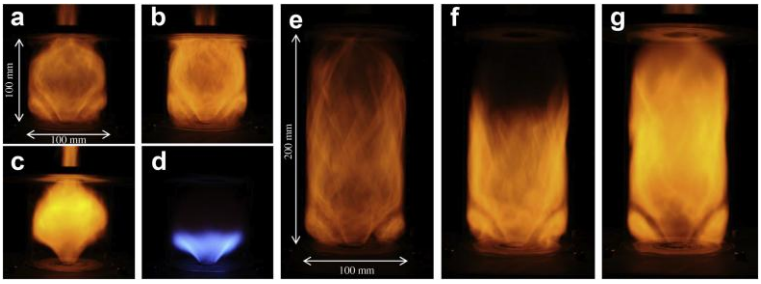

Fig. 2.5: Photographs of ammonia flames at a range of equivalence ratios and 13 kW thermal power compared to an equivalent methane flame. Reproduced from [48].

2.2.2. Ammonia/Methane

An accelerant blended into the fuel can improve the combustion characteristics of ammonia flames. One option is methane, the main constituent molecule of natural gas. More precisely, ammonia/methane fuel blends have been investigated to assess the potential of adding ammonia to existing methane combustors to gradually decarbonise such processes. As the CH_4 fraction in the fuel blend increases, laminar burning velocity increases nearly linearly [51], as shown in Fig. 2.6.

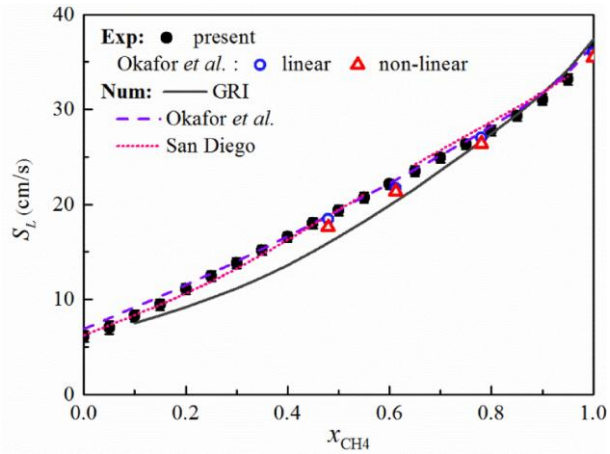

Fig. 2.6: Laminar burning velocities of stoichiometric NH_3/CH_4/air flames at atmospheric conditions. Reproduced from [51].

This increase in laminar burning velocity can have a resultant increase in stability limits [52]. Additionally, adding ammonia to methane flames can increase methane stability limits by reducing the risk of flashback [53] as shown in Fig. 2.7 from two different combustor designs. As flashback did not occur for a pure methane flame in stability map on the left, adding methane to the ammonia swirl flame always increased lean and rich blowoff limits in all blends. However, in the stability map shown on the right, flashback occurred from ammonia fuel fractions from 0 to 0.5. As a result, adding methane to the ammonia swirl flame increase lean and rich blowoff limits up to a 50/50 NH_3/CH_4 fuel blend. At higher CH_4 fractions, flashback sharply reduced the stability limits at rich conditions.

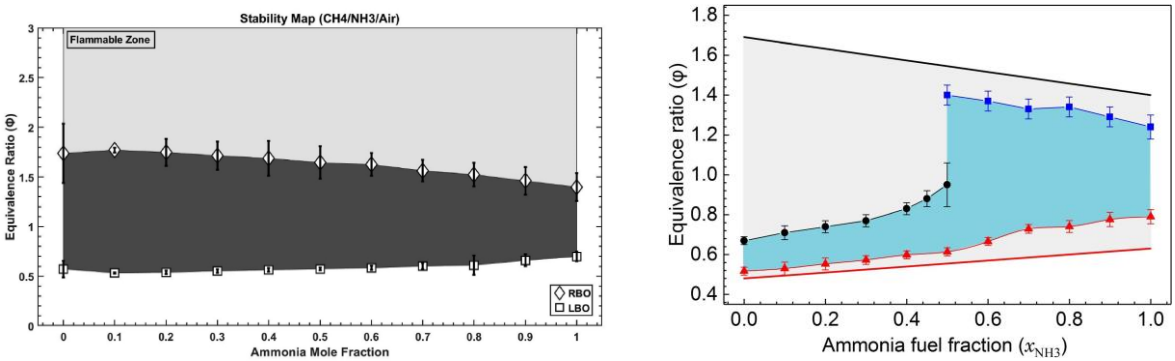

Fig. 2.7: Stability limits of ammonia/methane swirl flames. Left reproduced from [52], right reproduced from [53].

However, this expansion of stability limits with methane addition comes at a cost. At moderately lean to slightly rich equivalence ratios, adding methane to ammonia swirl flames increases NO emissions [53,54]. In Fig. 2.8, the highest NO emissions were measured at the lowest ammonia substitution rates of 0.2. This demonstrates the difficulty with adding only small amounts of ammonia to existing systems operating on methane. Interestingly, this study showed that NO emissions remained elevated compared to pure methane at Φ = 1.0 until 60% NH_3 substitution was reached.

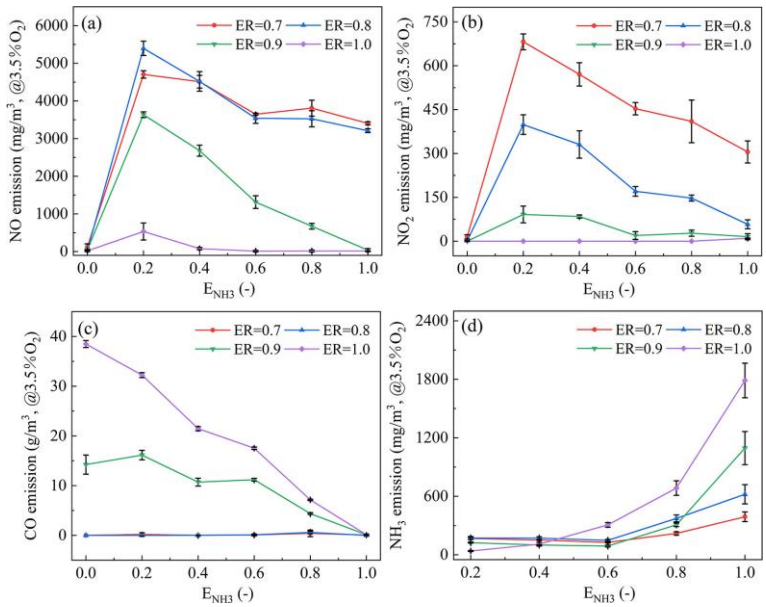

Fig. 2.8: Effect of NH_3/CH_4 fuel blend on emissions of NO, NO_2, CO and NH_3 for various equivalence ratios, reproduced from [54].

2.2.3. Ammonia/Hydrogen

Another potential accelerant to add to ammonia to improve its combustion characteristics is hydrogen – a highly reactive fuel. This high reactivity is demonstrated in Fig. 2.9, which shows laminar flame speed of ammonia/hydrogen blends rise exponentially with an increase in H_2 concentration [45]. This means that compared to an equivalent methane volume fraction, even a small amount of hydrogen in an NH_3/H_2 blend yields a more significant increase in flame speed. This increase in laminar flame speed with hydrogen addition is due to a reduction in chemical activation energy and transport effects from hydrogen's high diffusivity [55]. The hydrogen rapidly produces H atoms and other radicals which drive chain-branching reactions and disperse throughout the flame front, overcoming ammonia's high activation energies and resultant slow chemical kinetics.

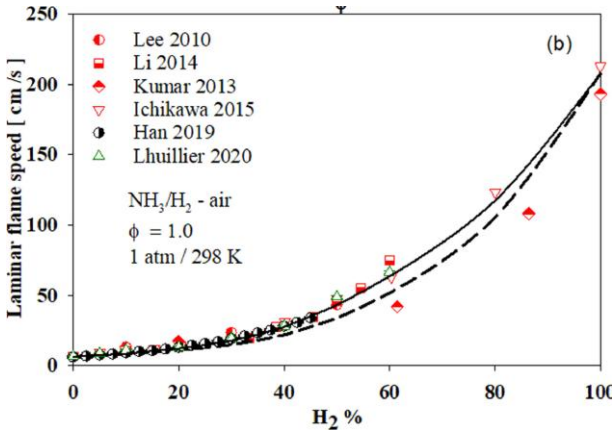

Fig. 2.9: Laminar flame speed of NH_3/H_2 blends at atmospheric temperature and pressure. Reproduced from [45].

In terms of emissions, adding hydrogen to ammonia flames assists in reducing some pollutants, but increases others. As shown in Fig. 2.10, NO emissions generally increase as X_{NH3} decreases from 0.9 to 0.55, at all equivalence ratios [56]. This was suggested to be due to higher hydrogen concentrations resulting in NO generation via the HNO route becoming dominant and suppressing the N/NH systems which consume NO at higher X_{NH3} ratios. On the other hand, N_2O emissions at lean conditions are reduced as hydrogen concentrations increase. This is due to higher flame temperatures and an increased supply of free H atoms readily available to consume N_2O. In terms of unburned NH_3 emissions, they are generally lower for higher hydrogen concentrations for a given rich equivalence ratio. However, NO emissions are also higher at the same equivalence ratio. Therefore, the main difference in total NO and NH_3 emissions at rich conditions with varying NH_3/H_2 ratios may be the equivalence ratio at which the lowest simultaneous emissions are reached, rather than the magnitude of those combined emissions.

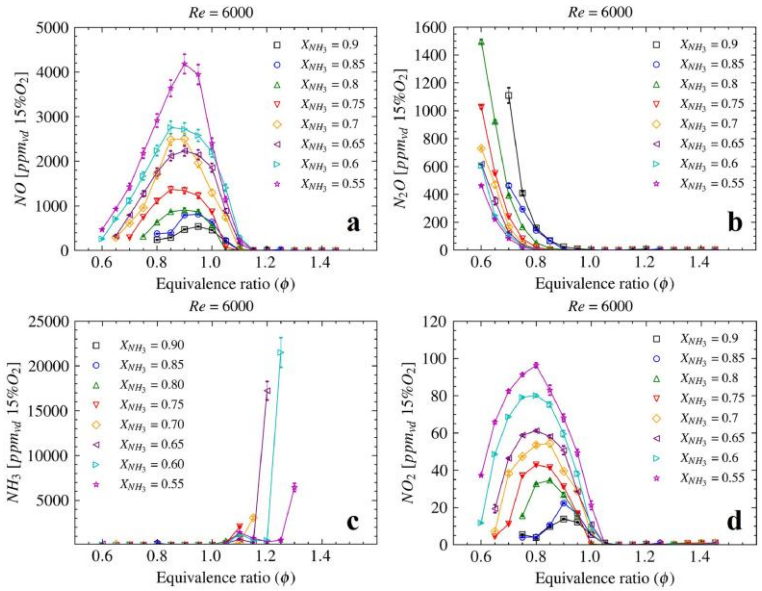

Fig. 2.10: Emissions of NO, N_2O, NH_3 and NO_2 from varying NH_3/H_2 blends and equivalence ratios. Reproduced from [56].

2.2.4. Partially Cracked Ammonia

As discussed in Section 1, the main downside of using hydrogen as a combustion enhancer in ammonia flames is storing and transporting the hydrogen. Therefore, the potential for partially cracking ammonia (discussed in Section 1.3.4) is attractive. The potential for using partially cracked ammonia was highlighted in the 1960s, where one study found that 28% cracked ammonia (0.56 NH_3 / 0.33 H_2 / 0.11 N_2 (mol.)) could be combusted in a gas turbine burner designed for hydrocarbon fuels without modification [44]. The combustion characteristics of partially cracked ammonia ($NH_3/H_2/N_2$) are similar to NH_3/H_2 blends, but the presence of molecular nitrogen in the fuel produced during the cracking process results in some flame differences. An example of this is shown in Fig. 2.11, where increasing the ammonia cracking ratio results in higher H_2 concentrations and hence laminar flame speed [57]. The inhibiting effect of the molecular nitrogen in the fuel blend is also clearly demonstrated, with the fully cracked ammonia blend (0.75 H_2 / 0.25 N_2 (mol.)) having an approximately 20 % lower stoichiometric flame speed than the pure H_2 shown in Fig. 2.9. This moderating effect is due to the N_2 absorbing some heat from the combustion process and hence reducing the adiabatic flame temperature compared to an equivalent NH_3/H_2 blend and slowing the chemical kinetics. This fuel blend can therefore be considered to have integrated dilution. A study from NTNU found that approximately 40 % cracked ammonia provided the same adiabatic flame temperature and laminar flame speed as pure methane at slightly lean conditions, suggesting this cracking fraction could be a suitable "drop-in" fuel for existing combustion systems [58].

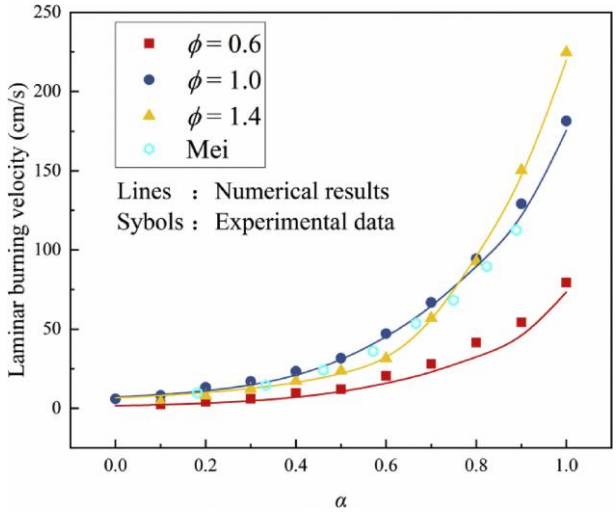

Fig. 2.11: Laminar burning velocity as a function of ammonia cracking fraction (α). Reproduced from [57].

Compared to pure NH_3 and NH_3/H_2 blends, there are fewer studies on the emissions from $NH_3/H_2/N_2$ flames available in the literature. In particular, there are none which compare the emissions from equivalent NH_3/H_2 and $NH_3/H_2/N_2$ flames to assess the impact of molecular

nitrogen addition to the fuel. An example of emissions from pure and partially cracked ammonia is shown in Fig. 2.12. As with NH_3/H_2 flames, the same trend of increasing NO and NO_2 emissions with increasing cracking fraction were found [59]. Despite H_2 and N_2 displacing NH_3 with fuel bound nitrogen as Cr increases, this increase in NO was suggested to be due to an increase in thermal NO production. As these conditions are near stoichiometric and hence high temperature, little N_2O was measured at any cracking fraction. Nonetheless, a small increase in N_2O emissions with pure ammonia was found, suggesting that partially cracking ammonia can reduce N_2O emissions. Despite the fuel lean conditions, the unstable pure ammonia flames produced significant unburned NH_3 emissions, which were quickly abated with increasing cracking fraction.

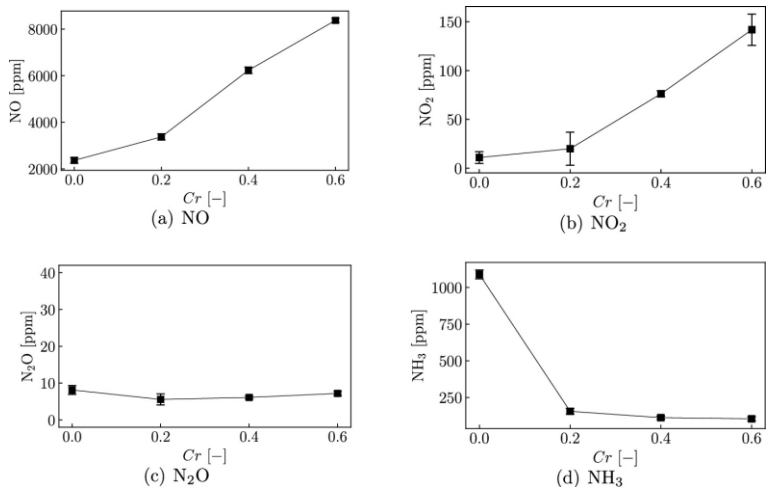

Fig. 2.12: Emissions of NO, NO_2, N_2O and NH_3 at phi = 0.9 as a function of cracking fraction. Reproduced from [59].

Recent research [60] into thermoacoustic instabilities shows that pure ammonia flames are relatively unresponsive to pressure fluctuations due to the long flame length and low flame speed, with gain cut-off frequencies as low as 100 Hz. They also found that cracking increased the gain cut-off frequency and hence tendencies for thermoacoustic instabilities significantly due to the shortening of the flame and hydrogen's high strain rate resistance. Nonethless, in comparing pure methane and partially cracked flames with similar unstretched laminar flame speed and adiabatic flame temperature, Wiseman et al. [58] found that the $NH_3/H_2/N_2$ flames had lower thermoacoustic gain. This demonstrates that even highly cracked ammonia flames could present less significant thermoacoustic issues in applications such as gas turbines, compared to pure methane or hydrogen.

2.3. Ammonia Oxidation Pathways

The combustion chemistry of ammonia is markedly different from that of hydrocarbons, and it further differs from hydrogen due to the presence of fuel bound nitrogen. The global stoichiometric reaction of ammonia/air combustion is shown in Equation (2-5), and it suggests the only products from complete ammonia combustion are water and nitrogen. This is of course an ideal reaction, and the real oxidation of ammonia is much more complex, with additional key products including NO, NO_2, N_2O as well as potentially unburned NH_3 and H_2 or unconsumed O_2.

$$4\ NH_3 + 3\ O_2 + 11.28\ N_2 \leftrightarrow 6\ H_2O + 13.28\ N_2 \qquad (2\text{-}5)$$

Chemical kinetic mechanisms can be used to better understand the chemical reactions occurring during combustion by examining thermodynamic, transportive and kinetic parameters. A fuller understanding of these parameters increases the effectiveness of combustion applications by improving flame stability and reducing pollutant emissions. However, the development of these kinetic mechanisms for generalised chemical prediction is challenging, particularly with varying equivalence ratios, operating conditions and fuel blends. The earliest kinetic mechanism for ammonia oxidation was developed in the 1980s by Miller et al. [61]. As shown in Fig. 2.13 , many other mechanisms have followed, demonstrating there is still no one mechanism which can accurately predict ammonia flames at a wide range of conditions [62].

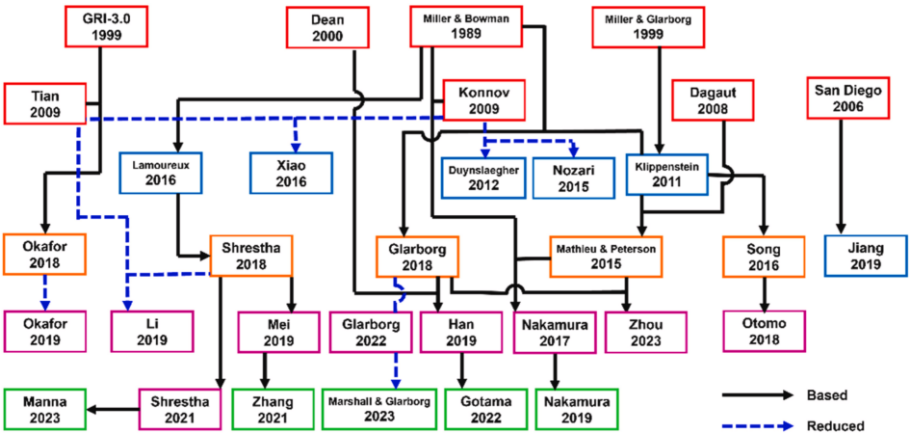

Fig. 2.13: Developmental tree of NH_3 mechanisms. Reproduced from [62].

Generally, ammonia oxidation can be considered a process where H atoms are gradually removed from the NH_3 molecule until N_2 is reached, oftentimes with some NO leftover. An example reaction pathway diagram from Stagni et. al [63] is shown in Fig. 2.14. The majority of NH_3 reacts with OH, removing an H atom to produce NH_2 and H_2O. From here, the NH_2 has four main pathways. The first is to continue with hydrogen removal to produce NH, which often forms N_2O by reacting with NO. If the temperatures are high enough, the majority of this N_2O will reduce

to N_2 with the assistance of a free H atom. The second pathway for NH_2 is to react with NH to ultimately form N_2 via N_2H_2 and NNH. The third route is to react with O atoms to form HNO, which quickly decomposes into NO, which is in fact the major route for NO production in ammonia-based flames. This is one of the major ways ammonia combustion differs from hydrocarbon combustion, where the classic thermal NOx mechanism – beginning with the reaction of molecular nitrogen and atomic oxygen – dominates. The final route for NH_2 is a major NO consumption route and is often referred to as the DeNOx reaction, where NH_2 and NO react together to directly produce molecular nitrogen.

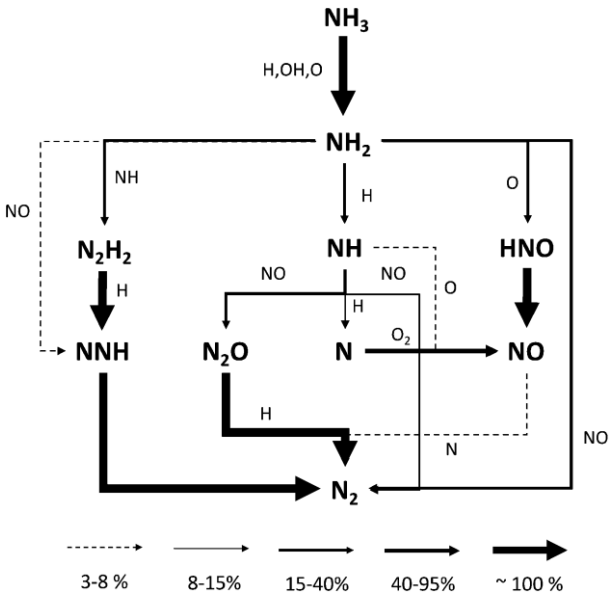

Fig. 2.14: Reaction flux analysis of NH_3 oxidation at T = 1523 K. Reproduced from [63].

Examining NO reactions more deeply, the reactions shown in Equations (2-6), (2-7) and (2-8) have been found to be key reactions in the production of NO in NH_3/H_2 flames at lean conditions [64]. These are fast reactions which are promoted by high concentrations of OH, H and O in the radical pool, usually found at lean or near stoichiometric conditions. The reaction shown in Equation (2-6) is the most dominant near stoichiometry due to its high sensitivity to temperature, and the increased availability of free H atoms from reduced oxygen availability.

$$HNO + H \leftrightarrow NO + H_2 \quad (2\text{-}6)$$

$$HNO + O \leftrightarrow NO + OH \quad (2\text{-}7)$$

$$NH + O \leftrightarrow NO + H \quad (2\text{-}8)$$

At slightly rich conditions, the reaction shown in Equation (2-6) is joined by Equations (2-9), (2-10) and (2-11) as the key reactions for the production of NO.

$$N + O_2 \leftrightarrow NO + O \quad (2\text{-}9)$$

$$NH_2 + HNO \leftrightarrow NO + NH_3 \quad (2\text{-}10)$$

$$N + OH \leftrightarrow NO + H \quad (2\text{-}11)$$

However, at slightly rich conditions there is little oxygen left in the radical pool, either as O or OH. Therefore, HNO production is markedly reduced and NO becomes the main fuel oxidiser, and NO consumption becomes dominant compared to its production. The main reactions dominating consumption of NO are shown in Equations (2-12), (2-13), (2-14), (2-15). Interestingly, N and NH reverse roles from being NO producers at lean conditions to strong NO consumers in the absence of oxygen. Of particular interest are the two 'DeNOx' reactions in Equations (2-13) and (2-14), a chain branching reaction which self-sustains the combustion process by producing fresh OH radicals to oxidise the NH_3 into NH_2, and the chain terminating reaction which produces only the ideal exhaust products from ammonia flames – N_2 and H_2O. However, if equivalence ratio is increased further, these NH_2 DeNOx reactions become less significant as NH_2 concentrations decrease.

$$NH + NO \leftrightarrow N_2O + H \quad (2\text{-}12)$$

$$NH_2 + NO \leftrightarrow NNH + OH \quad (2\text{-}13)$$

$$NH_2 + NO \leftrightarrow N_2 + H_2O \quad (2\text{-}14)$$

$$N + NO \leftrightarrow N_2 + O \quad (2\text{-}15)$$

N_2O is another key potential pollutant from ammonia-based flames which must be carefully controlled. The reaction responsible for the majority of N_2O production is shown in Equation (2-12). This is a fast reaction occurring almost solely in the flame zone and is responsible for the reduction in NO emissions seen at very lean conditions, typically $\Phi < 0.6$. Conversely, the two reactions responsible for the majority of N_2O consumption are shown in Equations (2-16) and (2-17) [65].

Generally, N_2O is produced at all conditions as part of normal ammonia combustion. N_2O consumption however is dependent on certain requirements, which if not met results in high emission of N_2O. One requirement is the availability of free H atoms to consume N_2O via the reaction shown in Equation (2-16). If there is too much oxygen available to consume free H atoms (i.e., from conditions being overly fuel lean), H atoms are consumed by N_2O at a lower rate. Therefore, as equivalence ratio increases, N_2O consumption increases. Higher temperatures can also assist in producing more free H atoms by providing the energy required to separate them from their parent molecules or radicals (NH_3, NH_2, NH, H_2 etc) more readily. The reaction in Equation (2-17) is less significant in the flame zone, but more significant in the post-flame zone,

where H atom availability is lower. This reaction is highly temperature dependent – if heat loss is too high and temperatures too low, N_2O consumption will decrease. This reaction is also dependent on residence time, with a longer post flame zone providing the residence time required to continue consumption of N_2O.

$$N_2O + H \leftrightarrow N_2 + OH \quad (2\text{-}16)$$

$$N_2O + (M) \leftrightarrow N_2 + O + (M) \quad (2\text{-}17)$$

An example of the effect of hydrogen blending on kinetics of ammonia flames is related to N_2O. As shown in Fig. 2.10, increasing H_2 concentration in an NH_3/H_2 fuel blend reduces N_2O emissions. This is because it increases availability of free H atoms to consume N_2O, thus boosting the reaction shown in Equation (2-16). It also increases temperatures, producing even more free H atoms and increasing the reactivity of the third body reaction shown in Equation (2-17).

Recent mechanisms have achieved good accuracy in prediction of NH_3/H_2 fuel blends. However, these mechanisms are often only accurate at certain conditions (equivalence ratio, fuel blend, inlet temperature and pressure etc.) or for only specific product gases. To date, no one mechanism has yet achieved high accuracy at all conditions, for all products [66]. This is further demonstrated by the continued development of new kinetic mechanisms. Therefore, careful mechanism selection is required depending on operating conditions used.

2.4. Combustion modes for Ammonia Fuelling

As discussed in Sections 2.2.3 and 2.2.4, blending ammonia with hydrogen, either as a binary blend or from partial cracking of ammonia, can overcome one of the main challenges relating to the application of ammonia as a fuel – flame stability. The other remaining challenge is emissions of NOx. Therefore, many works in the literature focus on minimising NOx formation or converting produced NOx to benign species such as N_2 within the flame. A range of strategies will be summarised in this section, including stratifying fuel injection, dilution with steam, passive measures such as varying equivalence ratio and amount of premixing, as well as pressurisation and axial staging of air.

2.4.1. Fuel Stratification

Fuel stratification seeks to achieve the best of both worlds – low NO and high combustion efficiency – by combining premixed and non-premixed flame regimes in one combustor.

A study from Jin et al. [67] have used this methodology to great effect in a 30/70 % (vol.) NH_3/H_2 fuel blend. Here, an array of premixed air/fuel swirl injectors was utilised, shown in Fig. 2.15. Many fuel flow path permutations were examined in this study and compared to a base, uniform blending (UB) case of lean premixed 30/70 % (vol.) NH_3/H_2, where this uniform mixture was supplied through all injectors simultaneously. The highest reduction in NO emissions compared to the uniform blending configuration was found with a rich 90/10 % (vol.) NH_3/H_2 blend in the inner injection stage, and lean, pure H_2 in the outer injection stage. As shown in Fig. 2.15, they found a minimum concentration of 310 ppm NO and 136 ppm H_2, with no unburned NH_3 measured, a marked improvement compared to the uniform blending case.

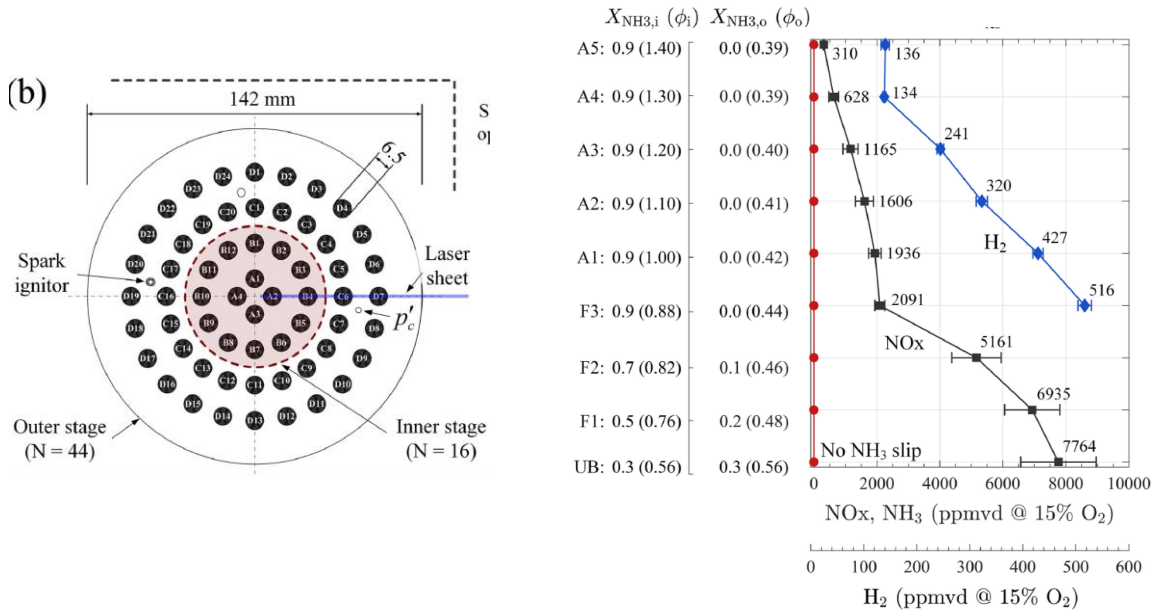

Fig. 2.15: Schematic of multi-element injector assembly and emissions with different injection regimes. Reproduced from [67].

An earlier study from Pugh et al. [68] compared a base, fully premixed 70/30 % (vol.) NH_3/H_2 case against H_2 diffusion from a central lance and premixed NH_3/air in the outer swirling flow and with the flow paths reversed. They found that the compared to the fully premixed case, injecting diffusive NH_3 resulted in a significant reduction in NO emissions due to rich pockets of non-premixed NH_3 resulting in an increase in NO consumption by NH_2. However, emissions of unburned NH_3 were also significant. On the other hand, H_2 diffusion within a premixed NH_3/air swirl flame seemed to perform better overall, with approximately half the NO of the fully premixed case and only slightly elevated emissions of NH_3.

Abdullah et al. [69] investigated the effect of partial premixing in NH_3/CH_4 flames. They fully premixed the CH_4 and air by injecting CH_4 far upstream, in Port 1 in Fig. 2.16. They varied the mixing of NH_3 by injecting it in Port 1 (to achieve "full" premixing) and Ports 2 and 3 to achieve varying amounts of partial premixing. Also shown in Fig. 2.16, They concluded that NO emissions increased as mixing decreased, regardless of NH_3 ratio in the fuel blend. This highlights the apparent difference between NH_3/CH_4 and NH_3/H_2 fuel blends, as well as the need for further investigation on partial premixing.

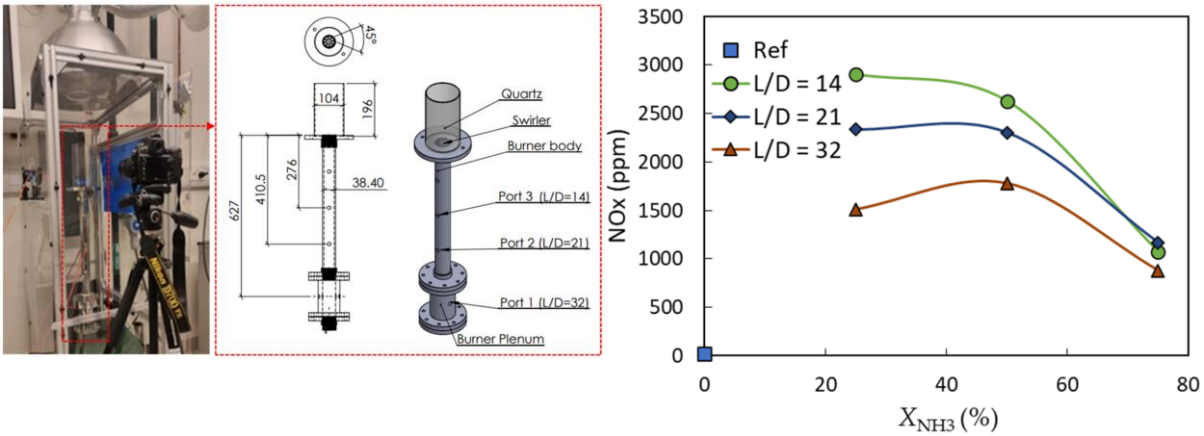

Fig. 2.16: Experimental rig for investigating partial premixing of NH_3/CH_4 flames and the resultant measured emissions of NOx. Reproduced from [69].

A series of studies from Wang et al. of Shanghai Jiao Tong University have investigated fuel stratification of NH_3/CH_4 swirl flames [70–72]. Here, a premixed CH_4/air swirl flame was stratified with a central premixed NH_3/air flame and compared with fully premixed conditions. A visual comparison is shown in the left of Fig. 2.17. The central NH_3 jet flame is clear to see at 50% NH_3 concentration in the stratified case and the swirl structure in the outer premixed CH_4 flame is slightly disrupted but not lost. This disruption stems mainly from the NH_3 jet flame cancelling out the central recirculation from the CH_4 swirl flame which ultimately results in a longer swirl flame, rather than a compact premixed flame. Intense mixing between the hot products of the central NH_3 flame and the excess oxygen from the lean premixed CH_4 swirl flame occurs in the vortex breakdown region, forming a flame structure analogous to air staging to ensure full fuel burnout.

Shown in the right side of Fig. 2.17, Wang et al. found a significant reduction in NO, NO_2 and CO using the stratified (dual flame) configuration. The stratified configuration had lower OH concentrations in the central flame, which resulted in reduced NO production via HNO [70]. Further study also highlighted that HNO production was also reduced via the NH_2 route and that thermal NO production was lower for the stratified case [72]. They found an even larger NO reduction with stratification when increasing the inlet temperatures up to 473 K, as a result of an increase in the influence of NH_2 consumption as temperature increased [71].

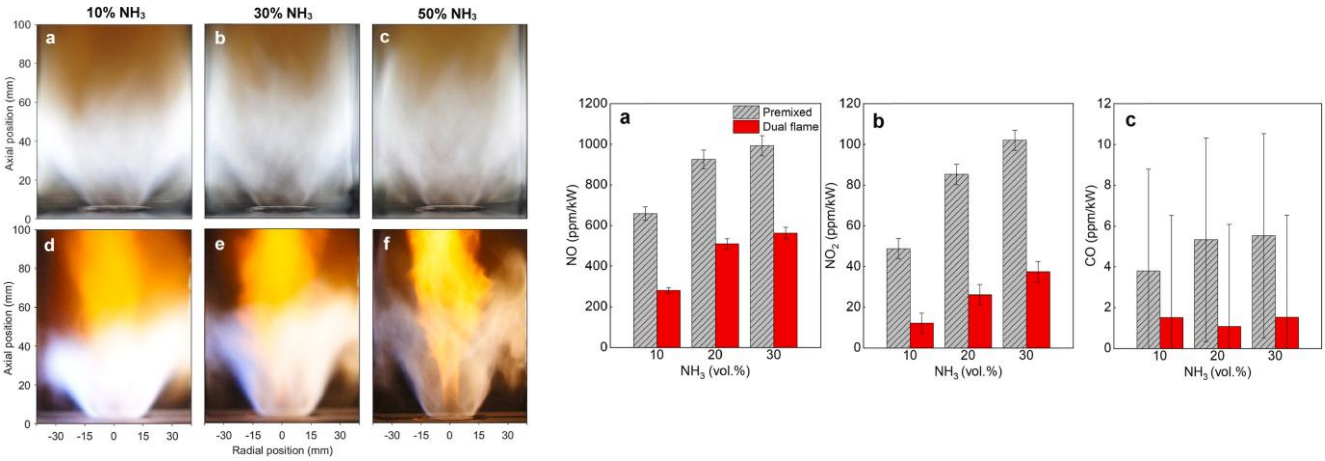

Fig. 2.17: Comparison of flame shape (left) and emissions (right) between fully premixed and stratified NH_3/CH_4. Reproduced from [70].

Mashruk et al. also investigated 70/30 % (vol.) NH_3/H_2 swirl flames with stratification [73]. Here, they maintained fully premixed NH_3/air in the outer swirling flow and also maintained the H_2 flowrate. The H_2 stratification ratio was then varied from 0 % (fully premixed) to 100 % (fully stratified). They found that increasing H_2 stratification reduced NO and NO_2 emissions, but increased N_2O emissions at lean conditions. This was suggested to be due to higher stratification rates concentrating free H atoms closer to the burner centre axis, away from the swirling NH_3 flame which was producing the N_2O for the H atoms to normally consume when premixed.

2.4.2. Humidification

A classic approach for reducing NOx emissions from hydrocarbon flames is steam injection, or humidification which reduces flame temperatures and hence the efficacy of the thermal NOx pathway. This methodology has been proven in gas turbines operating on natural gas [74–76] and methane/hydrogen blends [77]. However, there has been limited research on this methodology in ammonia-based flames until recently. Pugh et al. investigated the effect of steam injection on emissions of NO and N_2O in a 70/30 % (vol.) NH_3/H_2 swirl flame [78,79]. They found that reactant humidification reduced NOx emissions at rich conditions by limiting thermal NOx production but resulted in elevated NH_3 emissions. At ultra-lean conditions, shown in Fig. 2.18, they again found a reduction in NOx emissions as well as in increase in N_2O emissions. The explanation for this was an increase in NH consumption by NO to increase production of N_2O, and a decrease in consumption by the third body reaction shown in Equation (2-17).

Little other research on the effects of steam injection in ammonia-based swirl flames is available in the literature, but more fundamental studies have been carried out. Shi et al. [80] found that at ultra-lean conditions of Φ = 0.5, NO formation was reduced by 43 % at T = 1375 K in a jet-stirred reactor due to a reduction in HNO production. However, they found that at stoichiometric and rich, high temperature conditions, NO production increased, as the H_2O acted as an oxidiser in the normally oxygen sparse conditions. This apparent contradiction between the two studies can potentially be explained by the difference in experimental setup. Pugh et al. used a swirl burner, while Shi et al. used a jet-stirred reactor (JSR). The JSR likely has significantly longer residence times and uniform temperature which may prevent radical quenching and cooling downstream of the flame, as would occur in a swirl burner. This means NO emissions from the swirl flame can reduce to N_2, whereas NO emissions in the JSR are effectively "frozen" as NO. This highlights the need for studies with practical combustion systems, such as swirl burners.

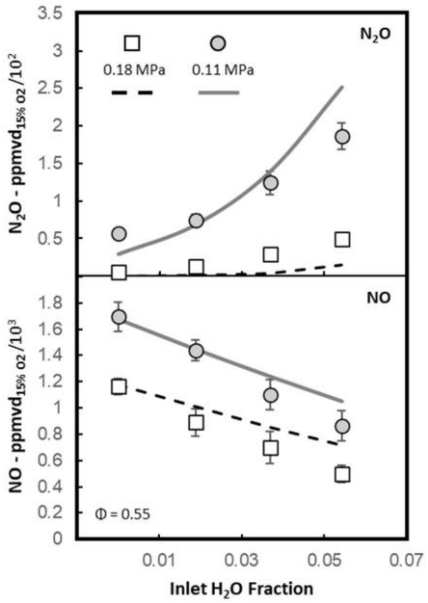

Fig. 2.18: NO and N2O emissions from an NH_3/H_2 Swirl flame with increasing water loading. Reproduced from [79].

2.4.3. Heat Management

The impact on emissions from pure ammonia swirl flames with different combustor liners was investigated by Okafor et al. [81]. They compared insulated and uninsulated stainless steel and quartz glass combustor linings to assess the impact on emissions with varying heat loss to the combustor walls. Fig. 2.19 below shows a marked reduction in measured NO emissions from the insulated wall cases (black circles) and the uninsulated cases (red diamonds, blue squares) at all equivalence ratios. The opposite trend can be seen for emissions of unburned NH_3. The authors suggested two processes influencing this; NO production cannot occur without NH_3

consumption, and NO consumption is increased in the presence of unburned NH_3. This suggests that excessive heat loss to the uninsulated walls resulted in reduced NH_3 consumption and hence lower combustion efficiency, followed by a reduction in NO emissions. They also found that the uninsulated combustor walls resulted in higher emissions of N_2O due to a reduction in H atom production and reduced temperatures for the third-body reaction to consume N_2O.

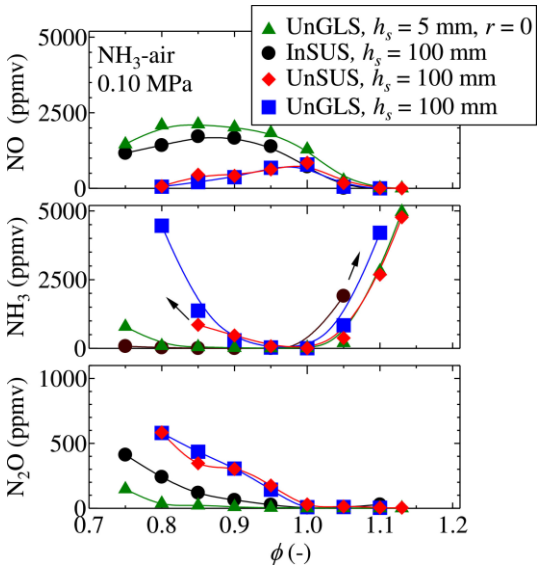

Fig. 2.19: Effect of wall heat loss on emissions from pure ammonia flames. Reproduced from [81].

Another study from Zhang et al. [82] simulated gas turbine film cooling by flowing air over the outside of the combustor walls to increase heat loss from a pure ammonia flame. They also found a decrease in NO and increase in NH_3 emissions with increased heat loss at lean conditions, with seemingly little effect at stoichiometric or rich conditions. They suggested that flame quenching on the relatively low temperature wall locally reduced OH production, which in turn limited NO production via HNO.

These studies investigate relatively passive heat loss to the wall rather than considering management of heat loss as an active NOx control methodology, representing a gap in the literature. Furthermore, no studies have been published examining the effects of heat loss on emissions from NH_3/H_2 nor from partially cracked ammonia flames.

2.4.4. Passive Flame Control

Classic hydrocarbon combustion achieves low NOx using “passive” lean premixed regimes, which reduce temperature and hence thermal NOx production [83]. However, early studies using lean premixed NH_3/H_2 flames from Valera-Medina et al. reported potential for high NOx emissions

of the order of thousands of ppm at lean conditions [84]. This was because despite lower temperatures, fuel-bound nitrogen reacted with abundant OH and O radicals to form NO. As shown in Fig. 2.20, they also noted that ultra-lean equivalence ratios of Φ = 0.43 emitted just over 100 ppm NOx, highlighting potential for relatively low NOx emissions. However, this study did not measure emissions of N_2O, which have since been found to increase rapidly at lean conditions [65,81,82,85]. Reducing emissions of CO_2 but replacing them with N_2O emissions cannot be considered a practical, sustainable solution due to N_2O's high global warming potential. Currently, commercial selective catalytic reduction systems are not sufficiently effective for removing N_2O emissions from exhaust gases as they require expensive catalysts, high temperatures and the process is inhibited by oxygen and steam [86], which constitute roughly 30% (vol.) of the exhaust gas from a lean NH_3/H_2 flame. Therefore, ultra-lean combustion of ammonia is not considered viable.

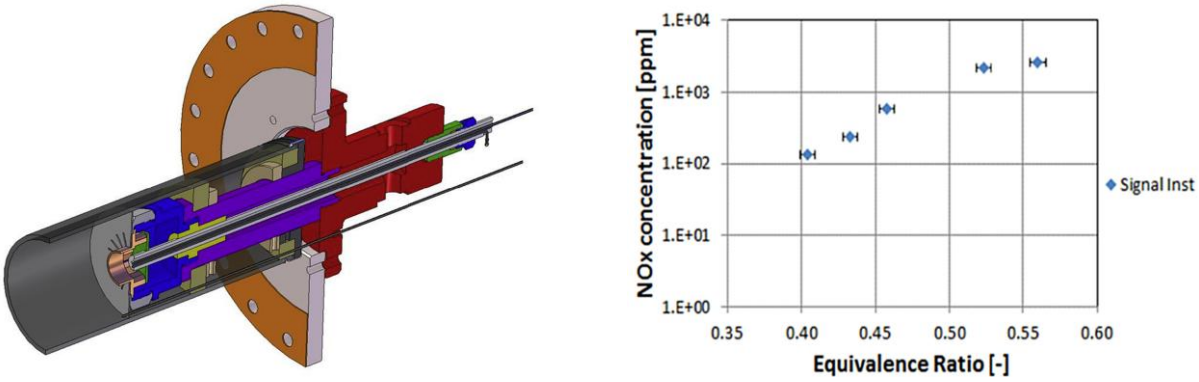

Fig. 2.20: Generic swirl burner and experimental NOx emissions from fuel lean premixed 50/50 % (vol.) NH_3/H_2 flames. Reproduced from [84].

At the other end of the equivalence ratio spectrum, fuel rich combustion has also been shown to emit low [87] or negligible amounts of NO, NO_2 and N_2O [48,88]. The downside at rich conditions is emission of unburned fuel [48]. For example, at Φ = 1.1 in Fig. 2.21 NH_3 reached ~3500 ppm and H_2 ~2.5 % (vol.). While emissions of NH_3 and H_2 are effectively unregulated in many countries, they should be nonetheless avoided due to health and safety risks – primarily toxicity for NH_3 and explosion for H_2. Additionally, unburned fuel emissions are never ideal from an economic perspective. As to be discussed in the following sections, air staging can be an effective method to combust these remnant fuel emissions, but care must be taken to avoid the production of fresh NO or N_2O emissions.

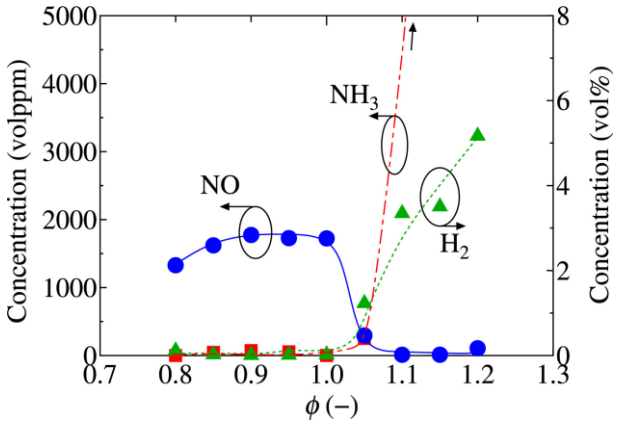

Fig. 2.21: Emissions of NO, NH3 and H_2 from a pure ammonia swirl flame. Reproduced from [48].

When examining premixed vs non-premixed ammonia combustion, Okafor et al. found that unlike with hydrocarbon flames, pure ammonia diffusion flames emitted lower NO than fully premixed flames in the primary zone. However, lower combustion efficiency was reported, with higher unburned NH_3 [47].

Both premixed and non-premixed pure ammonia swirl flames have also been investigated by Pugh et al. [89]. Shown in Fig. 2.22, they too found that non-premixed swirl flames had significantly lower NO emissions than premixed. This was suggested to be due to the imperfect mixing in the diffusion case – local fuel rich zones led to increased concentrations of NH_2 available to consume NO via the reactions shown in Equations (2-13) (2-14). The downside is that the imperfect mixing results in higher emissions of unburned NH_3.

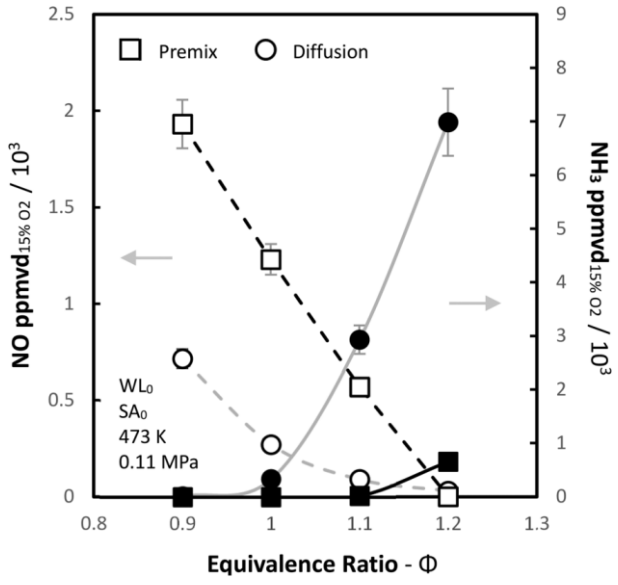

Fig. 2.22: Measured NO (dashed) and NH_3 (solid) emissions for premixed and diffusive NH_3/Air swirl flames. Reproduced from [89].

Another study from Pugh et al. [90] examined the influence of swirl number on NO emissions from a non-premixed 25/75 % (vol.) NH_3/H_2 flame. They found this fuel blend could be stabilised at geometric swirl numbers of 0.8 and 2.0 at ambient and elevated pressure. Increasing the geometric swirl number from 0.8 to 2.0 doubled NO emissions at atmospheric pressure, without any noticeable change in oxygen concentrations, which were used as an indicator of combustion efficiency. Emissions of N_2O and unburned NH_3 were not presented in this study, which could potentially explain the NO trends found. Interestingly, this difference in NO emissions was less pronounced as pressure increased, with NO emission parity between the swirlers being reached at 0.6 MPa. It was therefore suggested that high swirl could be optimal as pressure was increased further towards gas turbine conditions and further study was warranted.

2.4.5. Pressurisation

Combustion at elevated pressure – and temperature – is of particular relevance to gas turbines. A significant body of work examining the effects of pressurisation on emissions from ammonia-based swirl flames has developed over the past decade, some of which will be summarised here.

A study from Khateeb et al. examined the effect of elevated pressure on emissions from NH_3/H_2 swirl flames up to 4 bar [91]. They found that increasing pressure significantly decreased NO at all lean conditions, shown in Fig. 2.23. At Φ = 0.9, NO emissions were roughly halved from ~3000 ppm to ~1500 ppm. However, the diminishing NO reduction effect as equivalence ratio is reduced is clear to see, with negligible differences in NO emissions at Φ = 0.7 as pressure increases. With higher H_2 concentrations, lower equivalence ratios were achievable, and the plateau-like behaviour at leaner equivalence ratios remained.

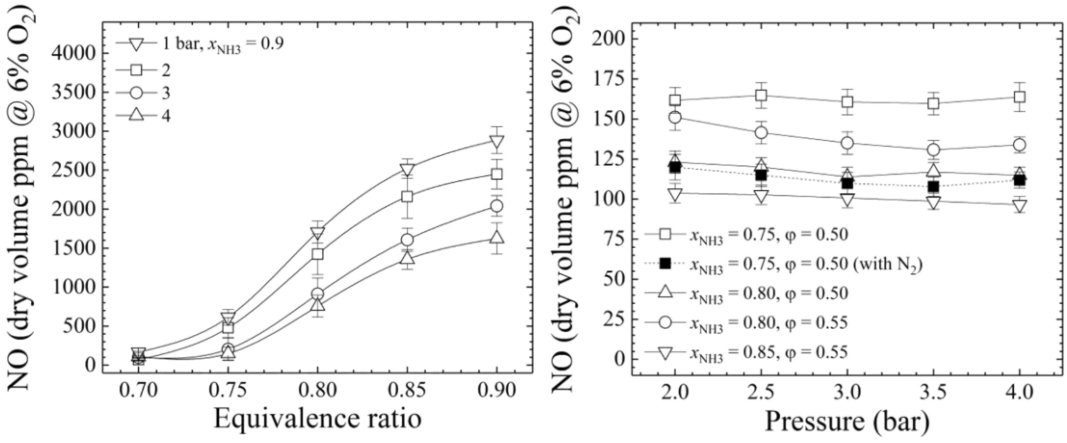

Fig. 2.23: NO emissions from lean NH_3/H_2 swirl flame with increasing pressure. Reproduced from [91].

Several studies on the effects of pressurisation have been carried out by Pugh et al. At ultra-lean conditions – shown in Fig. 2.24 – they also found that increasing pressure moderately reduces NO emissions [79]. This was attributed to a reduction in NO production via HNO paired with an increase in NO consumption by NH and NH_2. They also found a reduction in N_2O emissions, with a greater sensitivity to pressure than NO primarily due to an increase in N_2O consumption via the third body reaction. This may be related to pressure shortening the flame and increasing thermal energy density. At rich conditions, the trend of reducing NOx emissions is maintained also due to an increase in consumption of NO by NH_2 [78]. They also highlighted a plateau effect as pressure increased – NO decreased more gradually.

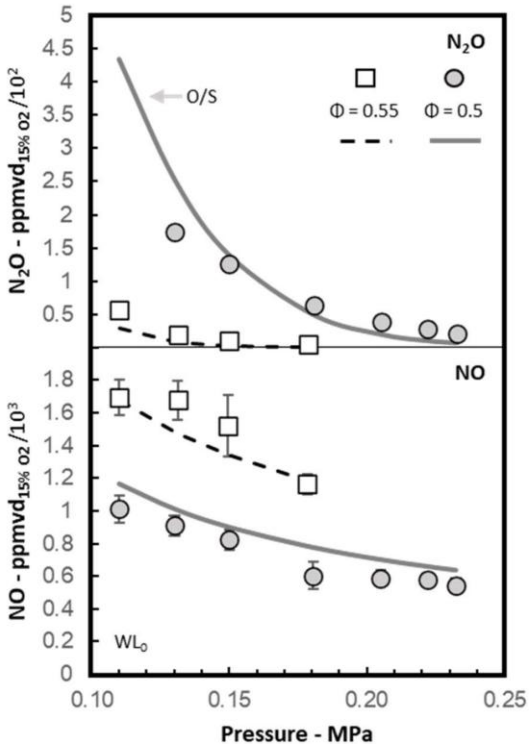

Fig. 2.24: NO and N_2O emissions from ultra-lean NH_3/H_2 swirl flames with increasing pressure. Reproduced from [79].

A recent study from Ditaranto and Saanum [92] examined a wide range of cracking fractions at high pressures up to 10 bar. They also found a reduction in NO emissions as pressure increased and discussed the plateau effect in detail. Shown in Fig. 2.25, they found that at cracking fractions of > 60 % (~20 % NH_3 volume ratio in the fuel), there was only a small reduction in NO as pressure increased from 5 bar to 10 bar. At a cracking ratio of > 80 %, very little difference in NO emissions can be seen with pressure.

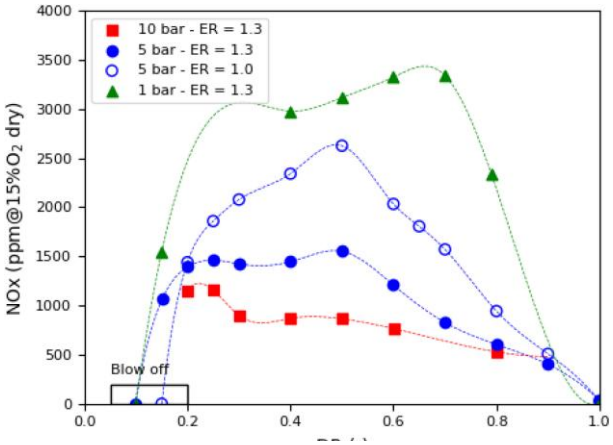

Fig. 2.25: Effect of cracking ratio and pressure on NOx emissions. Reproduced from [92].

2.4.6. Axial Staging

Of the NOx emission reduction strategies discussed so far in this section, it could be argued that rich conditions are the most attractive, due to the avoidance of N_2O production. However, the downside is it results in reduced combustion efficiency and hence emissions of H_2 and NH_3, which is not ideal. Therefore, axial air staging has been investigated, most commonly with a fuel rich primary stage and fuel lean secondary stage. The aim is to achieve low NOx emissions in the primary stage and then combust the remnant fuel with additional air supplied to the post-flame zone. The key challenge is to avoid the production of fresh NOx or N_2O emissions in this fuel lean secondary stage.

A study from Okafor et al. investigated air staged pure ammonia swirl flames in premixed and non-premixed configurations [47]. With a constant global equivalence ratio of Φ = 0.38, the lowest emissions were found when the primary equivalence ratio was 1.1. With this fixed primary equivalence ratio, they found that the global equivalence ratio should only be lean enough to fully consume the unburned NH_3 from the primary stage, and if conditions were globally ultra-lean, NOx emissions rose – shown in Fig. 2.26. This was true for both premixed and non-premixed configurations. In a premixed configuration with 99.5% NH_3 consumption, NO emissions reached a minimum of approximately 120 ppm and 40 ppm with inlet pressures of 0.1 MPa and 0.2 MPa, respectively.

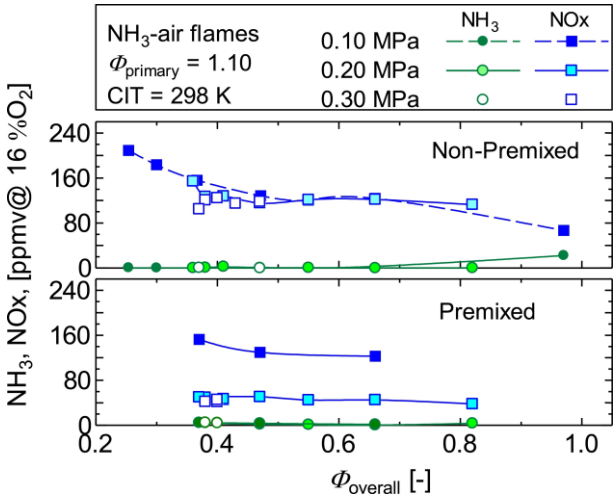

Fig. 2.26: Measured emissions of NO and NH_3 from a pure ammonia swirl burner with varying global equivalence ratio. Reproduced from [47].

The findings of only "slightly" lean global equivalence ratios producing the optimal balance of NO and unburned NH_3 emissions also come from Pugh et al. [78], shown in Fig. 2.27. Here, a 70/30 % (vol.) NH_3/H_2 flame was used with pressurisation and steam injection. The lowest emissions of ~30 ppm NO and ~50 ppm NH_3 were found at primary and global equivalence ratios of 1.25 and 0.98, respectively, with 0.18 MPa operating pressure and a moderate amount of steam injection.

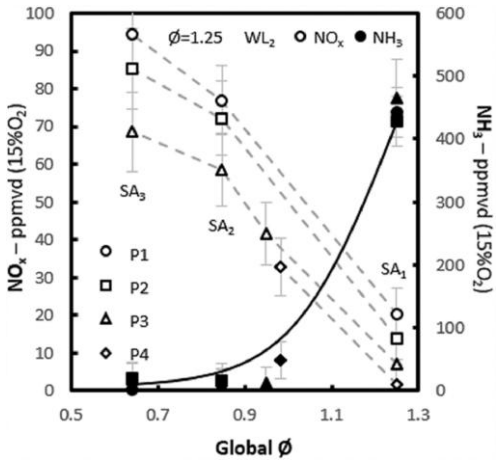

Fig. 2.27: NO and NH_3 emissions with varying secondary equivalence ratio. Reproduced from [78].

A recent study from Srinivasarao et al. [93] investigated pure ammonia combustion with up to four preheated air stages, shown on the left side of Fig. 2.28. Air flow rates were not metered for each individual stage. However, at global stoichiometry, CFD results indicated that for the four-stage system, local equivalence ratios were 2.2 in the first stage, followed by 1.7, 1.15 and 1.0 in the fourth stage. Shown in the right side of Fig. 2.28, NO emissions of less than 1 ppm/kW were achieved with four stages at 40 kW (4S-F40) and negligible emissions of NH_3 were recorded, despite the rich global equivalence ratio of Φ = 1.2. This was presumably possible due to the

relatively high thermal power and well insulated combustor thermally cracking the unburned NH_3 in the final stage into H_2.

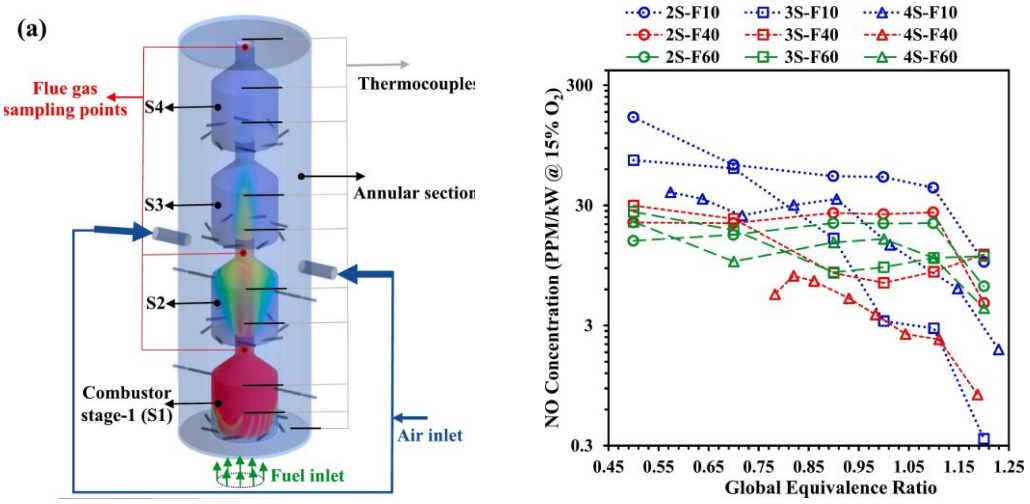

Fig. 2.28: Combustor schematic and NO emissions recorded for varying number of air stages (S) and thermal powers (F) and global equivalence ratios. Reproduced from [93].

2.5. Research Gaps

A rich literature investigating various methodologies to reduce emissions from lab-scale ammonia-based flames has emerged in recent years. Nonetheless, the problem of emissions from ammonia-based flames has not been fully solved, and several research gaps remain in this area. In this thesis, the following contributions address these gaps through the research papers produced:

- Emissions behaviour of partially cracked ammonia blends (Chapters 3, Humidification4 and 5)

  Compared to NH_3/H_2 blends, relatively few studies on equivalent partially cracked ammonia ($NH_3/H_2/N_2$) blends have been carried out. As $NH_3/H_2/N_2$ blends from partial in-situ cracking are more practical than NH_3/H_2 blends from two separate storage vessels, it is important that the effect of the added molecular nitrogen on emissions is understood. This is especially true for NOx reduction methodologies such as fuel stratification and humidification.

- Improved emissions normalisation methodologies (Chapter 4)

  The published studies on partially cracked ammonia usually report the emissions on a volumetric ppm normalised to dry conditions with a particular oxygen concentration. The diluent effect of nitrogen in the fuel is not properly accounted for with this methodology, and

alternative methodologies (such as normalising to a mass per unit power basis) would be useful.

- Novel NOx reduction strategies via thermal management (Chapter 5)

Temperature management via controlled heat loss represents an underexplored NOx reduction methodology. This research investigates how imposed heat losses influence flame temperature and emissions.

- Translation of laboratory research to industrially relevant systems (Chapters 4, 5 and 6)

Another research gap to investigate is linking lab-based academic studies to industrial applications. For example, in the humidification studies highlighted above, steam is usually raised using a separate electric heater system, whereas in practical systems any steam for humidification would likely be raised using combustion heat via a heat exchanger. This is an important difference as the additional heat loss to the heat exchanger may affect flame stability or emissions inherently or present an opportunity to actively control emissions. Another example of linking lab-based academic studies with industrial applications is the scale-up of swirl burners to higher thermal power. To avoid flame blowoff as gas inlet flowrates increase, the burner nozzle must be scaled in terms of annular cross-sectional area. However, this can quickly result in excessively large combustor injectors. An investigation of design parameters such as nozzle geometry and swirl number with ammonia-based flames is important to improve static stability limits without compromising practical considerations.

Addressing these research gaps and meeting the objectives outlined in Section 1.4 would further the development and deployment of zero-carbon, low NOx and fuel-efficient swirl burners in industrial settings.

3. Fuel Stratification

This chapter comprises the journal paper titled "Experimental and numerical investigation of $NH_3/H_2/N_2$ combustion in a premixed/stratified swirl burner" published in the Journal of Engineering for Gas Turbines and Power. Further information is presented in the Statement of Authorship of Publications.

Its novelty lies in examining the effect of fuel stratification on emissions from partially cracked ammonia flames for the first time. In particular, this study focuses on the role of the diffusive equivalence ratio of the inner H_2 flame, providing new insights into its influence on emissions characteristics.

This chapter advances the aim of the thesis by addressing the overall theme of advancing the development of industrial swirl burners utilising partially cracked ammonia. It partially addresses objectives 2, 3 and 4. It experimentally investigates a methodology for reducing emissions from partially cracked ammonia flames – fuel stratification – with a focus on investigating the effect of the diffusive equivalence ratio for the first time. It examines the resultant impact on unburned emissions of NH_3 at globally rich conditions with fuel stratification. It also uses a chemical reactor network to determine significant reactions responsible for the NOx reduction found. It is linked directly to Chapters 4 and 5 as they examine alternative NOx reduction methodologies using the same laboratory-scale atmospheric swirl burner.

Abstract

Interest in using renewably produced, partially cracked ammonia in gas turbines is gaining traction, but challenges relating to emissions of NOx and unburned ammonia remain. The present work progresses existing research on using hydrogen stratification to reduce NOx from ammonia/hydrogen flames by experimentally and numerically investigating the effects of also injecting nitrogen from the cracking process. It additionally assesses the NOx reduction capability of a recently developed novel swirl burner by adding hydrogen to the stratified flow to maintain the diffusive equivalence ratio at two high NO production conditions, slightly lean and stoichiometric.

At slightly globally rich conditions, maintaining the diffusive equivalence ratio at 0.9 resulted in an order of magnitude reduction in NO emissions with only a 33% increase in unburned NH_3, compared to a fully premixed flame with the same fuel and air flow rates. This stratified

configuration was found to increase consumption of NO by NH_2, likely due to flame morphology effects, while NO production from OH and HNO pathways was reduced. The reduced OH intensity was posited as the cause for increased NH_3 emission. A strong emissions sensitivity to diffusive equivalence ratio was found, as the case with a stoichiometric diffusive equivalence ratio did not show such marked improvements over its corresponding premixed condition. Both stratified and premixed flames were found to be stable, however stratification has potential to trigger instabilities at different frequencies to premixed.

3.1. Introduction

Renewably produced ammonia is considered a promising carbon-free energy vector due to its relative ease and low cost of storage and transportation compared to pure hydrogen [94]. Although these advantages are even greater if pure ammonia is used directly as a fuel, there are combustion challenges relating to its low reactivity and NOx emissions [31,95]. Blending ammonia with other fuels to increase reactivity has been studied extensively. Mixing ammonia with methane or hydrogen has shown favourable improvements in burning velocity [45,96] and flammability limits [52]. Combustion with methane as part of the fuel will always result in carbon dioxide emissions, so mixing with hydrogen is the better option for decarbonisation. Furthermore, as ammonia has significant hydrogen content of ~18% on a mass basis [97], an ammonia/hydrogen fuel blend can be achieved by partially cracking the ammonia immediately prior to combustion [98]. This has the added benefit of reducing cost by having to store only one fuel.

Numerous studies have also investigated NOx mitigation strategies from ammonia/hydrogen fuel blends. Mashruk et al. demonstrated the NOx emission dependence on ratio of ammonia to hydrogen [88], and the strong unimodal relationship between global equivalence ratio (Φ_G) and NO emissions, with a peak near $\Phi_G = 0.9$ [52]. These studies noted that negligible NO_x emissions could be achieved at $\Phi_G = 1.2$-1.3 due to NO consumption by NH_2 but resulted in significant unburned NH_3 emissions due to a decrease in the availability of H, O and OH radicals. They also showed significant N_2O emissions at lean conditions ($\Phi_G < 0.8$) due to a reduction in flame temperature inhibiting N_2O consumption by free H atoms and shorter flames reducing residence time for the third-body reaction to act in [65,79,85]. N_2O is an important exhaust gas to monitor as it has a global warming potential roughly 250 times larger than carbon dioxide, meaning a flame with no CO_2 emissions but around 240ppm N_2O would have a similar global warming effect to a methane-air flame, as calculated in [99]. Recently, partially premixed ammonia/hydrogen combustion has received considerable attention to further reduce NO emissions. An NH_3/H_2

partially premixed concept was initially proposed and examined by Pugh et al. [68] at rich conditions. A diffusive flow of either NH_3 or H_2 was injected through a central lance with the main aim of creating local fuel-rich regions in the middle of the reaction zone. This resulted in a reduction in NO emissions but significant unburned NH_3 emissions were recorded. This study also examined the effect of elevated inlet pressures and temperatures more relevant to gas turbine conditions and reported an increase in NO emissions, particularly at rich conditions. As this is a complex nonmonotonic relationship depending on multiple variables, any kinetic mechanism selected for predicting emissions from pressurised stratified flames would require careful testing and validation. Franco et al. [100] proposed an alternative configuration for NH_3/H_2 flames, using two co-axial tubes, injecting fuel axially through the inner tube and air tangentially through the outer tube via a bluff body. However, the results presented by Franco et al. [100] did not deliver details of unburned ammonia, thus requiring further investigations. Mashruk et al. [73] recently presented a novel stratified combustion system that can operate in both premixed and stratified modes using ammonia/hydrogen blends. They observed that an increase in hydrogen stratification resulted in a reduction of NO and NO_2 emissions, but increased N_2O because of the reduced fuel in the premixed flow. It should be noted that the above works used only blends of ammonia, hydrogen and air, neglecting the nitrogen produced alongside the hydrogen in the cracking process.

The current work builds upon previous investigations by studying the influence of stratification in $NH_3/H_2/N_2$ flames utilising the same burner described by Mashruk et al. [73] at Cardiff University. Initially the premixed flow was maintained as a $20\%_{(vol.)}$ cracked ammonia blend and extra diffusive hydrogen was added to the stratified flow to preserve two set diffusive equivalence ratios (Φ_D), whilst varying the global equivalence ratio (Φ_G). Additionally, a numerical study using the CFD-CRN approach enabled a rate of production analysis to be carried out on the emissions results.

3.2. Materials and Methods

This study assessed the NOx reduction capability of a recently commissioned burner system operating on a base blend of $20\%_{(vol.)}$ cracked ammonia ($(66.7/25/8.3\%_{(vol.)}$ $NH_3/H_2/N_2$). Extra diffusive H_2 was injected into the stratified flow with the aim of promoting NOx production, to aid in identifying mechanisms for NOx reduction. In Case 1 Stratified, the extra diffusive H_2 flow rate was set to maintain the central diffusion flame at a slightly lean equivalence ratio (Φ_D = 0.9), known to produce peak NO emissions. For Case 1 Premixed, the same extra H_2 was instead

added to the premixed flow, to offer a direct comparison. The global equivalence ratio was then varied $0.8 < \Phi_G < 1.12$. Addition of extra diffusive H_2 slightly varied the fuel blend, but this change was mirrored in the premixed configuration so comparisons could be drawn. This process was repeated in Case 2, but with the central diffusion flame maintained at stoichiometry ($\Phi_D = 1.0$) to increase flame temperature. As Case 2 had a richer diffusive flame, the global equivalence ratio could be increased further, allowing $0.8 < \Phi_G < 1.2$ to be tested. As mentioned previously, operating at conditions leaner than $\Phi_G = 0.8$ produces prohibitively high N_2O emissions and so was not investigated here. All experiments were conducted at a constant thermal power of 10kW.

3.2.1. Swirl Combustor

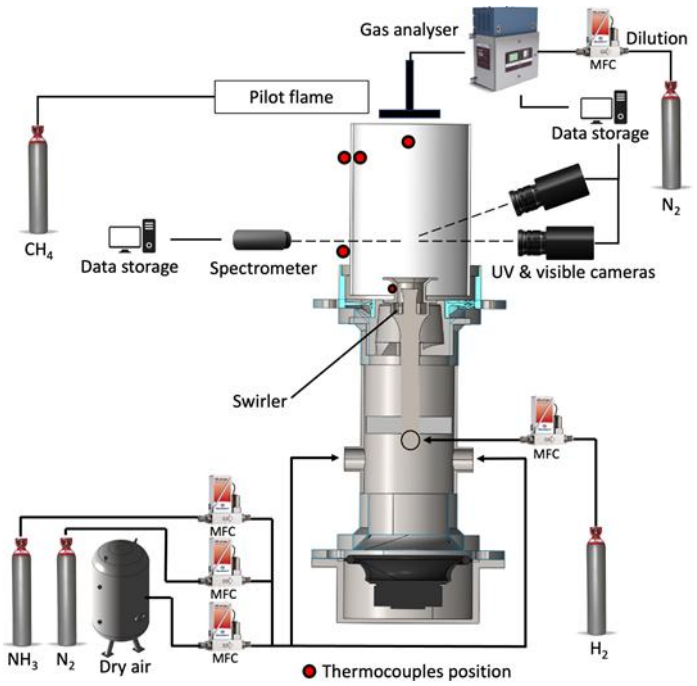

Fig. 3.1: Schematic of experimental setup (not to scale)

Experiments were conducted using an optically accessible radial-tangential swirl combustor (S_g = 1.05) shown in Fig. 3.1 at atmospheric conditions (1.1 bar, and 288K).

Fuel and air were supplied using Bronkhorst mass flow controllers (± 0.5% between 15-95% of maximum flow). Fig. 3.2 shows a diagram of the combustor architecture and flow paths. When operating in fully premixed mode, all H_2 was injected at the base of the swirler, mixing with NH_3, N_2 and air before flowing through the injector nozzle (d = 31.5 mm), using a central injection lance (d = 22.5 mm) as a bluff body. In stratified mode, the central injection lance was unblocked to allow some NH_3, N_2 and air through. Additionally, a portion of the H_2 was injected from the end of the central injection lance, ensuring the diffusion flame was maintained at either $\Phi_D = 0.9$ or 1.0 to promote NO_x production. The global equivalence ratio Φ_G was calculated relative to the stoichiometric air-fuel ratio (AFR) as (Φ_G = total $AFR_{stoichiometric}$ / total AFR_{actual}), including both

premixed and diffusive flows shown in Fig. 3.2. The diffusive equivalence ratio Φ_D was calculated in the same manner but only considering the flow through the central injector.

To facilitate optical access for flame monitoring, chemiluminescence imaging and spectrometry, the flame was confined within a quartz glass tube (d = 156 mm). The flame was monitored from a distance of 5 m using a Logitech Brio camera.

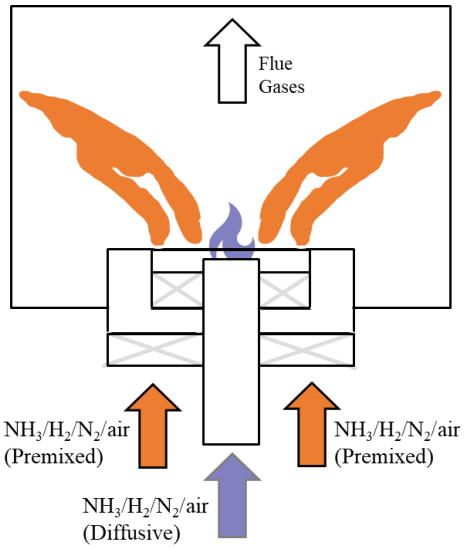

Fig. 3.2: Simplified diagram of combustor architecture

3.2.2. Exhaust Gas Measurements

NO, NO_2, N_2O, NH_3, O_2 and H_2O were measured simultaneously using an Emerson CT5100 quantum cascade laser system. The cross-shaped sample probe with equidistant holes for homogenous sample collection was situated 25 mm above the quartz tube outlet. Measured oxygen content was negligible at stoichiometric conditions, indicating no outside air was entrained into the sampling probe. The samples were carried to the gas analyser via a heated line, with measurements performed at 463 K. For each condition, 120 samples were captured with a sampling rate of 1 Hz (± 1% repeatability, 0.999 linearity), averaged, and normalised to dry 15 % O_2 following equation 14 in [101]. Ongoing discussion surrounds this emission normalisation method [102], due to elevated water content in the exhaust of hydrogen-based fuels inflating dry ppmv values. However, as this paper focuses solely on cracked ammonia as a fuel, and no direct comparisons were drawn with carbon-based fuel, this method was deemed acceptable. For conditions where raw readings were above the analysers range, N_2 dilution was used (± 10 % repeatability), as explained in detail in [85].

3.2.3. Chemiluminescence Measurements

OH* (309 nm; $A^2\Sigma$-$X^2\Pi$ system), NH* (336 nm $A^3\Pi$-$X^2\Sigma$ system) and NH_2* (630 nm; single peak of NH_2 α band) images were captured simultaneously by multiple LaVision cameras each with a Sony ICX285AL sensor and Hamamatsu HB105831 intensifier and appropriate Edmund Optics bandpass filters as in [85]. The cameras recorded at a sampling frequency of 10 Hz for a period of 20 seconds and the captured images were background corrected, 3x3 median filtered and averaged in Davis v10. The averaged chemiluminescence images then went through an Abel Deconvolution script in Matlab [103]. In this study, a positive correlation between ground state and excited radicals is assumed, as in [68,104]. An Avaspec-ULS4096CL spectrometer was used to capture broadband chemiluminescence intensity for a wide range of wavelengths, from 200-1100 nm. It featured a 100 μm slit and a 300 lines/mm grating, resulting in a full width half maximum resolution of 4.6 nm. The spectrometer specified a 4096-pixel CMOS detector measuring 7 x 200 μm, set to an exposure time of 1 second and averaged over 120 scans to improve the signal to noise ratio. Via a 600 μm fibre optic cable, it was connected to a collimating lens for UV and visible light, mounted 30 mm above the burner outlet and 240 mm away from the central axis.

3.2.4. Pressure and Temperature Measurements

A water-cooled Kistler 211B6 pressure transducer mounted in the combustion chamber near the burner exit was used to measure combustor dynamics. Pressure fluctuations were measured at a sampling rate of 25 kHz for a period of 20 seconds and then Fourier Transformed using a Matlab script for analysis.

The red dots in Fig. 3.1 denote positions of R and K type thermocouples which had sampling rates of 1 Hz and were averaged over a two-minute period for each operating condition.

3.2.5. Computation Fluid Dynamics-Chemical Reactor Network Approach

The combination of Computational Fluid Dynamics (CFD) and Chemical Reactor Networks (CRNs) allows for the precise configuration of CRNs by discretising volumes accurately. This method is commonly used in analysing complex combustion processes like those in gas turbines [105] with relatively low computational cost and short processing times. In this research, the CFD-CRN approach was applied to simulate and analyse the ammonia/hydrogen/nitrogen combustion. First, CFD was used to simulate a single test case, obtaining temperature and

velocity fields being crucial for defining different zones in the experimental setup. CRN numerical simulations of the flame were carried out using CHEMKIN-PRO. The CFD simulation was set up in ANSYS Fluent 2R2 using the Reynolds-Averaged Navier-Stokes (RANS) approach, to simulate one of the test points in the experimental campaign. A previous study [106] demonstrates that surrogate models can accurately predict NO_x emissions, temperature and velocity fields. In this work, the burner's geometry is modelled using a three-dimensional (3D) computational domain, comprising a total of 6 M polyhedral cells. The Realizable k-ϵ model with an enhanced wall function was the selected turbulence model. The Partially Premixed Combustion Model was implemented with the Flamelet Generated Manifold (FGM) approach [107]. The flamelets were carried out in Ansys Fluent, while the turbulence-chemistry interaction involved pre-integrating the look-up table with a β-PDF. The chemical kinetics from Otomo et al. [108] for the oxidation of ammonia-hydrogen flames, comprising 33 species and 213 reactions, was chosen for finite chemistry calculation. Zimont's Turbulent Flame Speed Closure (TFSC) [109] modelled the source term for the progress variable, defined as $c = Y_c/Y_{eq}$, where $Y_c = Y_{NO} + Y_{N_2} + Y_{H_2O} - Y_{H_2}$, and Y_{eq} is its equilibrium value. The laminar flame speeds included in the FGM combustion model were generated natively within Ansys Fluent after the boundary conditions were set and 1-D flamelets calculated. These laminar flame speeds were verified in CHEMKIN-PRO using the axisymmetric opposed-flow diffusion flame model by varying the equivalence ratio to account for the wide-ranging degree of premixing present in a stratified flame. Fig. 3.3 displays the axial velocity field with zone subdivisions characterising the Chemical Reactor Network CRN). Four inlets of air, NH_3, H_2 and N_2 were used to feed two Perfectly Stirred Reactors (PSRs) considering Premixed (P) and Stratified (S) sections, respectively. 100% of the exhaust from the Premixed PSR entered the Stratified PSR which had a short residence time. Then, 100% of this exhaust went to the Flame PSR. From the Flame PSR outlet, 70% went to the Post Flame Plug Flow Reactor (PRF), representing the flow zone where the velocity was completely axial. The other 30% of Flame PSR outlet was directed to the External Recirculation Zone (ERZ) and Central Recirculation Zone (CRZ) PSRs, split 5% and 25%, respectively. The ERZ PSR outlet fed back into the Flame PSR. Finally, the CRZ PSR outlet was split 70% and 30% to the Flame PSR and Mixer just upstream of the CRZ, respectively.

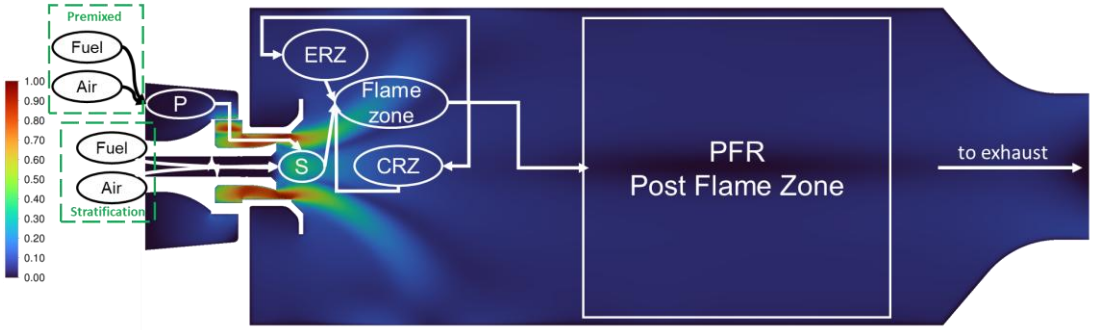

Fig. 3.3: Normalised velocity fields predicted by CFD simulation. Volume discretisation and zone division for CRN analysis.

To validate temperature trends within the PSRs and PFR reactors in the CRN, a thermal analysis was carried out; Fig. 3.4 shows the temperature field derived from CFD analysis. To determine the role of various reactions in changing NO emissions with stratification, absolute rate of production (ROP) values were calculated within the flame zone. The rate of consumption (ROC) is presented as a negative ROP, consistent with other studies [65]. Estimations of necessary heat loss were obtained from thermocouple measurements, located in appropriate positions in the burner.

Fig. 3.4: Normalised temperature distribution predicted by CFD simulation

3.3. Results and Discussion

3.3.1. Effect of Stratification on Emissions

In Case 1 Stratified, extra diffusive H_2 was injected into the stratified flow to maintain $\Phi_D = 0.9$ to promote NO production. It was compared to Case 1 Premixed, where the extra diffusive H_2 was injected into the premixed flow.

The order of magnitude reduction in NO emissions seen in Fig. 3.5 from Case 1 Stratified at $\Phi_G = 1.05$ can be explained by two main mechanisms, a reduction in NH and OH production and an increase in NO consumption by NH_2. HNO is an intermediary radical which can be formed from NH and OH radicals via the reaction shown in Equation (3-1).

$$NH + OH \leftrightarrow HNO + H \qquad (3\text{-}1)$$

$$N + OH \leftrightarrow NO + H \quad (3\text{-}2)$$

$$NH + NO \leftrightarrow N_2O + H \quad (3\text{-}3)$$

Fig. 3.6 demonstrates the reduction in NO production for Case 1 Stratified via HNO radicals, as well as from OH radicals directly via Equation (3-2). Again, assuming a positive correlation between ground state and excited radicals, these numerical results were validated by the chemiluminescence images shown in Fig. 3.7. OH* intensity was found to be similar, but over a smaller flame volume, supporting lower NO production from routes consuming OH and HNO. Although OH* intensity can be directly correlated with changes in temperature, Fig. 3.8 shows only small differences between the two configurations in the post-flame zone.

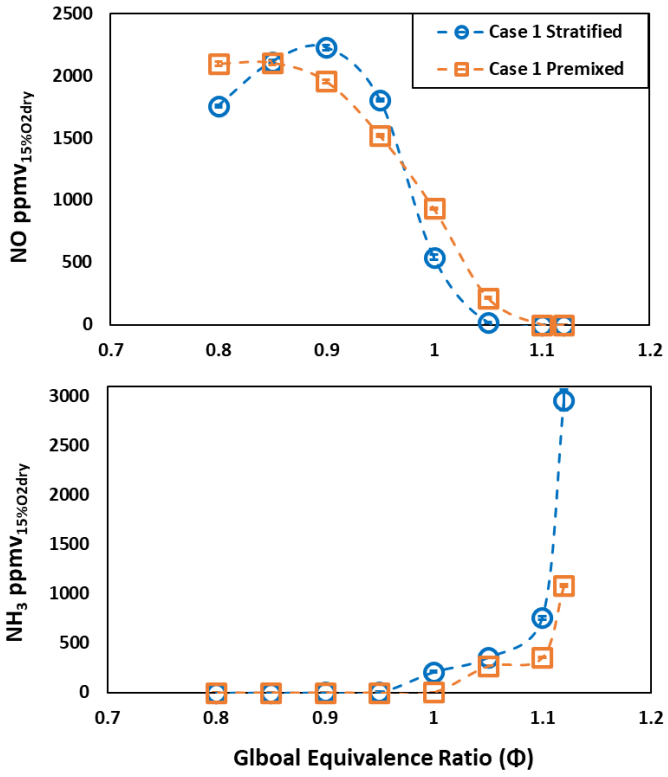

Fig. 3.5: Measured emissions from Case 1 with changing global equivalence ratio. NO (top) and NH_3 (Bottom). (Best-fit lines for clarity rather than modelled data).

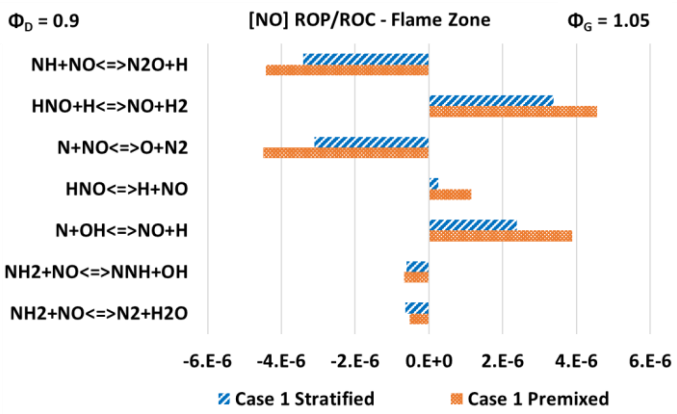

Fig. 3.6: Flame zone ROP/ROC [unit - mole/cm^3-s] for the most significant NO reactions at Φ_G = 1.05 for Case 1 stratified (blue) and premixed (orange).

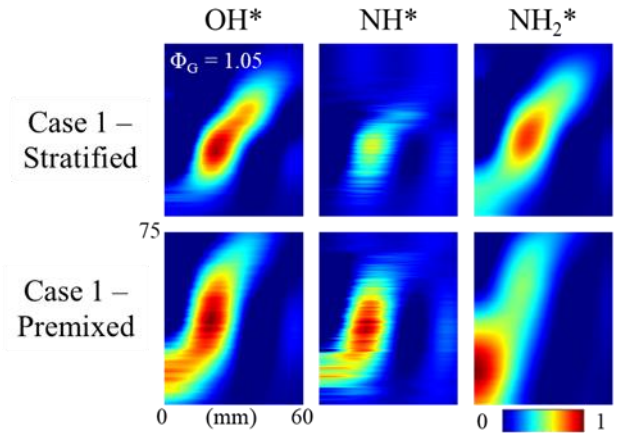

Fig. 3.7: Abel transformed chemiluminescence images (OH, NH* and NH_2*) of Case 1 Stratified (top) and premixed (bottom) at Φ_G = 1.05. Each species normalised to its Case 1 Φ_G = 1.05 maximum.*

NH* intensity was significantly lower in Case 1 Stratified, again supporting lower NO production from routes consuming HNO. Compared to Case 1 Premixed, the stratified configuration showed less NO consumption by NH via the reaction shown in Equation (3-3), which would also suggest a reduction in N_2O emissions. Consistent with previous studies [65,88] most conditions produced negligible N_2O emissions due to the relatively high equivalence ratios examined here, and so N_2O was not plotted for brevity. However, at the leanest global equivalence ratio investigated (Φ_G = 0.8), single digit ppmv (15% O_2 dry) N_2O values were measured for both Case 1 configurations, and the stratified N_2O value was lower, further indicating the accuracy of the numerical investigation. NO_2 emissions followed the same general trend as NO and so were not plotted for brevity. The peak of 70 ppmv (15% O_2 dry) NO_2 was found at the leanest conditions

measured, with Case 1 Stratified slightly lower and both configurations reaching negligible readings by $\Phi_G = 1.0$.

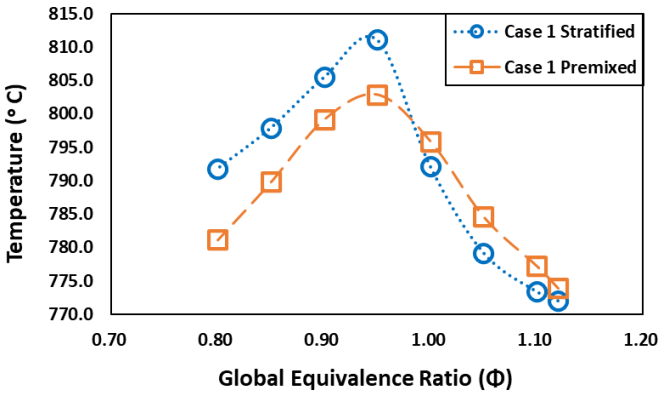

Fig. 3.8: Temperature readings from a thermocouple located in the centre of the quartz confinement 50mm upstream of the outlet for Case 1.

The other mechanism by which Case 1 Stratified had lower NO emissions than Case 1 Premixed above stoichiometry was an increase in NO consumption by NH_2, from the reactions in Equations (3-4) and (3-5).

$$NH_2 + NO \leftrightarrow NNH + OH \qquad (3\text{-}4)$$

$$NH_2 + NO \leftrightarrow N_2 + H_2O \qquad (3\text{-}5)$$

These reactions do not immediately appear significant in Fig. 3.6 until their contribution to the total NO consumption is considered. For Case 1, the contribution of these reactions was 35 % larger in the stratified flame than in the premixed flame. Fig. 3.7 shows Case 1 Stratified had slightly lower NH_2* intensity, centred farther away from the burner nozzle than Case 1 Premixed. This suggests less NH_2 was produced in the locally lean ($\Phi_D = 0.9$) area near the central injector and was instead produced further downstream where the local equivalence ratio was more rich. This more spatially dispersed NH_2 would then have a longer residence time to consume NO produced in the area near the central injector and be available to consume NO in the ERZ.

Also shown in Fig. 3.6, the thermal NO reactions of Equations (3-2) and (3-6) were slightly less significant in the stratified configuration than premixed for Case 1 at $\Phi_G = 1.05$. This small reduction in significance of thermal NO reactions is reflected in the small reduction in temperature for the stratified configuration at rich conditions shown in Fig. 3.8.

$$N + NO \leftrightarrow N_2 + O \qquad (3\text{-}6)$$

Unburned NH_3 emissions have previously been shown [110] to increase between $0.8 < \Phi_G < 1.2$ in fully premixed NH_3/H_2 flames due to reduced availability of OH radicals. This can explain the increase in NH_3 emissions shown in Fig. 3.5 for Case 1 Stratified. Fig. 3.7 does demonstrate a reduction in OH* intensity compared to Case 1 Premixed, but it is more clearly shown by the normalised chemiluminescence spectra intensity in Fig. 3.9 at $\Phi_G = 1.05$. The approximately 15 % increase in NO emissions from Case 1 Stratified shown in Fig. 3.5 at slightly lean conditions can be attributed to the change in NH and OH production, consistent with when $\Phi_G = 1.05$. However, the role of NH_2 in consuming NO was diminished, as expected from the lower NH_2* intensity at lean conditions shown in Fig. 3.9. There was a smaller difference in NO emissions between the two configurations at lean conditions, which is reflected in Fig. 3.10. However, some differences can still be seen. For example, both HNO and OH consumption to form NO were increased for Case 1 Stratified. Chemiluminescence data in Fig. 3.9 and Fig. 3.11 support these numerical results by showing higher OH* intensity at $\Phi_G = 0.9$. Fig. 3.10 also shows the reduced significance of NH_2 in the NO consuming Equations (3-4) and (3-5), as there was less NH_2 available to be consumed in these reactions at globally lean conditions, compared to the globally rich conditions.

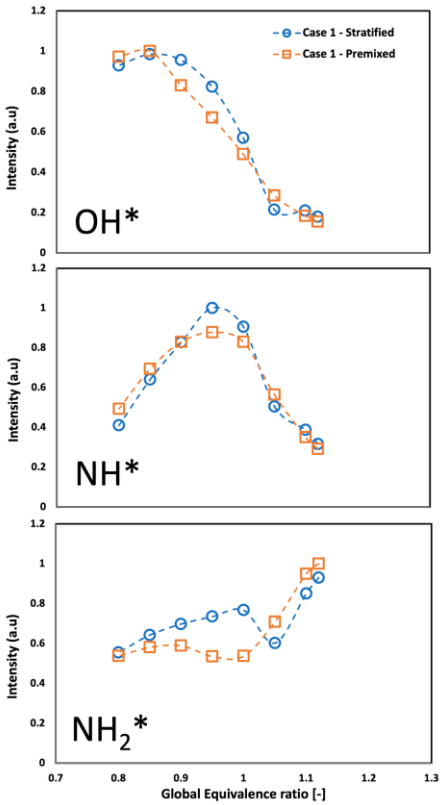

Fig. 3.9: Normalised optical chemiluminescence spectrometry results for OH, NH* and NH_2*.*

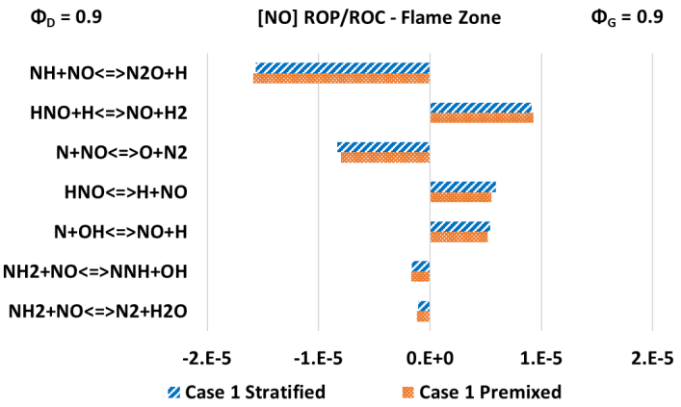

Fig. 3.10: Flame zone absolute ROP/ROC [unit - mole/cm^3-sec] for the most significant NO reactions at Φ_G = 0.9 for Case 1 stratified (blue) and premixed (orange)

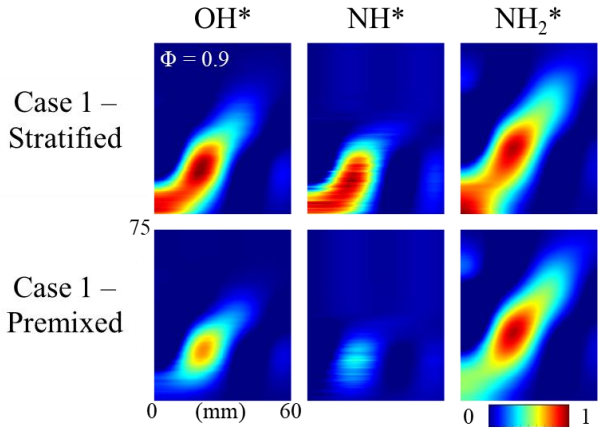

Fig. 3.11: Abel transformed chemiluminescence images (OH, NH* and NH_2*) of Case 1 stratified (top) and premixed (bottom) at Φ_G = 0.9. Each species normalised to its Case 1 Φ_G = 0.9 maximum.*

Studies have shown that heat loss from the flame to the confinement walls can have a significant influence on emissions from ammonia flames, with wall quenching reducing NO emissions, but increasing N_2O and NH_3 emissions [81]. This is not the case in this study, demonstrated by two main reasons. First, Fig. 3.7 and Fig. 3.11 show that although stratification did change the flame morphology, neither configuration caused the flame to impinge on the quartz glass confinement. The right-side edge of each chemiluminescence image is 60mm from the centreline of the flame, and the quartz tube is 18mm beyond that. The emissions data provides the second reason. Okafor et al. [81] reported N_2O and NH_3 emissions of 580 ppmv and 4457 ppmv at Φ_G = 0.8. Although this was from a pure ammonia flame and so not directly comparable to the current study, the fundamentals of ammonia combustion do apply. That is, emissions of unburned fuel at lean equivalence ratios represents a reduced combustion efficiency from excessive heat loss from the flame. That is not the case in the present study, proven by the negligible emissions of NH_3 at all conditions below stoichiometry, and the negligible or single digit ppmv emissions of N_2O at all conditions.

Both configurations in Case 1 reached negligible NOx emissions at a global equivalence ratio of 1.1, which is leaner than for NH_3/H_2 flames reported previously [88]. This is likely due to the N_2 present in the cracked ammonia fuel included in this study reducing reactivity and combustion efficiency. The combined emissions profile of Case 1 Stratified is particularly interesting at Φ_G = 1.05. Here, relatively low NO and NH_3 emissions of 20 and 358 ppmv (15% O_2 dry), respectively were found. This was an order of magnitude reduction in NO emissions with only a 33% increase in NH_3 emissions compared to the fully premixed configuration with the same total flow rates. In summary, this reduction in NO was a result of a reduction in NO production from OH and NH radicals, paired with an increase in NO consumption by NH_2. Lesser availability of OH radicals also resulted in an increase in unburned NH_3 emissions.

3.3.2. Effect of Varying Diffusive Equivalence Ratio

To investigate the effect of different central diffusion equivalence ratios, Φ_D was increased from 0.9 in Case 1, to 1.0 in Case 2. As in the previous section, the extra diffusive H_2 injected centrally in the stratified configuration was then injected into the premixed flow to provide baseline emissions for this fuel blend. As Case 1 had slightly different total flowrates to Case 2, the stratified configurations from each Case cannot be compared directly. It is however useful to compare the stratified configurations' relative difference from their respective premixed configurations.

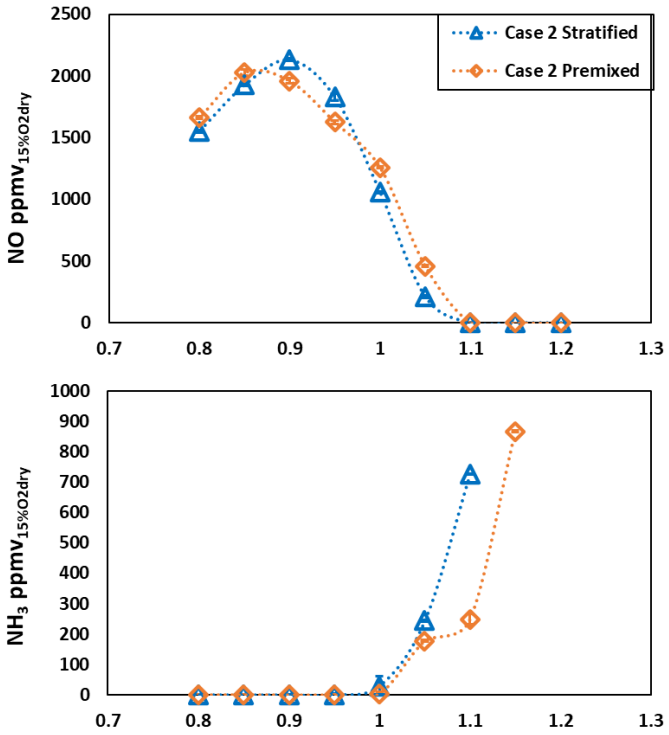

Fig. 3.12: Measured emissions from Case 2 with changing global equivalence ratio. NO (top) and NH_3 (bottom). Out of range NH_3 at rich conditions not plotted. (Best fit lines for clarity rather than modelled data.

Fig. 3.12 shows that for Case 2, stratification with the diffusive flame maintained at a more rich equivalence ratio of Φ_D = 1.0 was less effective in reducing NO emissions than the Φ_D = 0.9 in Case 1. At Φ_G = 1.05, Case 2 Stratified had NO emissions roughly half that of the Case 2 Premixed, but 37% higher unburned NH_3, a poorer trade-off than found in Case 1. This was a significant difference from a relatively small change in flow rates, so numerical simulations were performed to clarify the mechanisms responsible, which were then compared with chemiluminescent data again assuming a positive correlation between the ground state and excited radicals. Fig. 3.13 shows the differences in ROP/ROC between Case 2 Stratified and Premixed configurations was the same as for Case 1 in Fig. 3.6 but with smaller differences. This was expected as the differences between NO emissions was smaller.

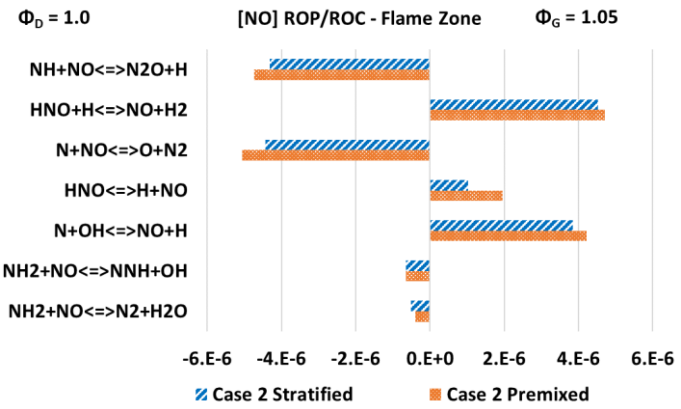

Fig. 3.13: Flame zone absolute ROP/ROC [unit - mole/cm^3-sec] for the most significant reactions at Φ_G = 1.05 for Case 2 stratified (blue) and premixed (orange)

Fig. 3.13 shows a smaller relative difference in the ROP from reactions which consume HNO to form NO for Case 2 configurations. An explanation for this difference could be due to the stoichiometric diffusive flame having a higher local flame temperature near the central injector, increasing the availability of free H atoms to react with HNO. As NH and OH combine to form HNO via the reaction in Equation (3-1), a smaller difference in OH* and NH* could be expected between the Case 2 configurations when compared to the Case 1 configurations. This is demonstrated in Fig. 3.14, where the NH* in particular has a similar intensity across the two configurations

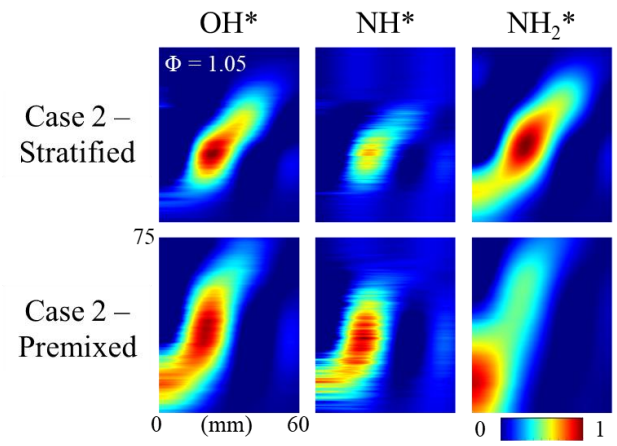

Fig. 3.14: Abel transformed chemiluminescence images of (OH, NH* and NH_2*) of Case 2 stratified (top) and premixed (bottom) at Φ_G = 1.05. Each species normalised to its Case 2 Φ_G = 1.05 maximum*

The other major difference shown in Fig. 3.13 is the smaller De-NOxing impact of the NH_2 radicals in Equations (3-4) and (3-5). In Case 1, the contribution of these reactions in the stratified configuration was 35 % larger than in the premixed configuration, but only 22 % larger in Case 2. The difference in consumption of NH and NO from Equation (3-3) was similar for both Cases. This reduction in NH_2 significance could relate to the ratio of NO produced in the diffusive flame versus total NO produced. The peak NO production was found at Φ_G = 0.9, suggesting that Case 1 Stratified (Φ_D = 0.9) would produce more NO in the diffusive flame than Case 2 Stratified (Φ_G = 1.0). Compared to their respective premixed configurations, they should produce the same total emissions due to their total fuel and air flow rates being the same. However, Case 1 producing a larger percentage of that total NO in the region near the central injector would allow that NO more residence time to be consumed by the NH_2.

Fig. 3.12 also shows a smaller increase in NO emissions at the lean conditions for Case 2 Stratified than was found for Case 1 Stratified. This was reflected in the ROP/ROC plot shown in Fig. 3.15 where the only variation of significance was again in the HNO decomposition reaction. As in Section 3.3.1, NO_2 followed the same trend as NO. In Case 2, NO_2 peaked at a slightly lower value of 64 ppmv (15% O_2 dry) at Φ_G = 0.8 and both configurations produced negligible readings at Φ_G = 1.0. N_2O emissions were negligible at all equivalence ratios tested and so neither are plotted here.

To summarise, the stoichiometric central diffusion flame in Case 2 had a smaller effect on reducing NO emissions than the slightly lean one presented in Case 1. This is likely related to the stoichiometric diffusion flame having a locally higher temperature, increasing the availability of free H atoms to react with HNO and ultimately produce NO.

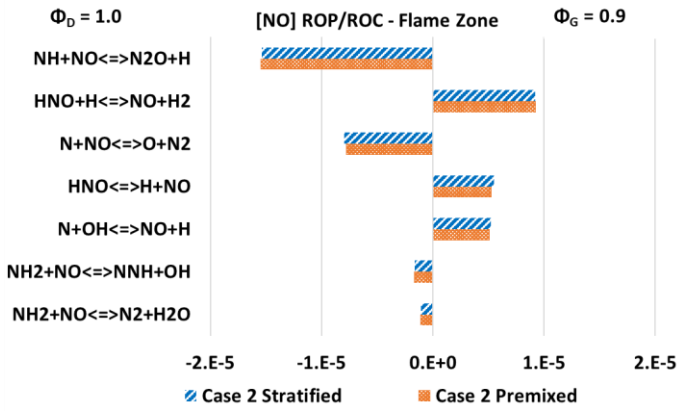

Fig. 3.15: Flame zone ROP/ROC [unit – mole/cm^3-s] for the most significant NO reactions at Φ_G = 0.9 for Case 2 stratified (blue) and premixed (orange).

3.3.3. Effect of Stratification on Flame Stability

All tested configurations and conditions provided a stable flame, with no indication of lean or rich blowoff owing to all fuel blends being near stoichiometric. The dynamic pressure fluctuations within the quartz tube flame confinement were measured for all test conditions. However, as the same trends were observed for both Cases, only Case 1, which provided the best emissions performance is presented here.

Fig. 3.16 shows the stratified configuration generally had lower RMS pressure fluctuations than the premixed configuration. The stratified case did not seem to possess the same sensitivity to equivalence ratio as the premixed and was comparatively constant at most test conditions.

It has been suggested that NH_2* can be used as a heat release marker in ammonia-based flames [104]. Fig. 3.7 and Fig. 3.14 showed that stratification had a strong effect on flame morphology, with the NH_2* production being centred further downstream than in premixed configurations. This relocated centre of heat release could have changed the time delay and hence phase difference between the heat release fluctuations and pressure fluctuations to be out of phase, reducing the thermoacoustic instability in line with the Rayleigh Criterion [111]. The introduction of equivalence ratio fluctuations from stratification could also have affected the phase difference.

Fig. 3.17 shows the Fourier transformed pressure signal for the Case 1 test point with the best emissions performance (Φ_G = 1.05) above 50 Hz. Both configurations produced relatively high amplitude broadband combustion noise below 50 Hz of a similar magnitude, likely related to the

injector geometry. There were however some significant differences at higher frequencies, so only those are presented and discussed here.

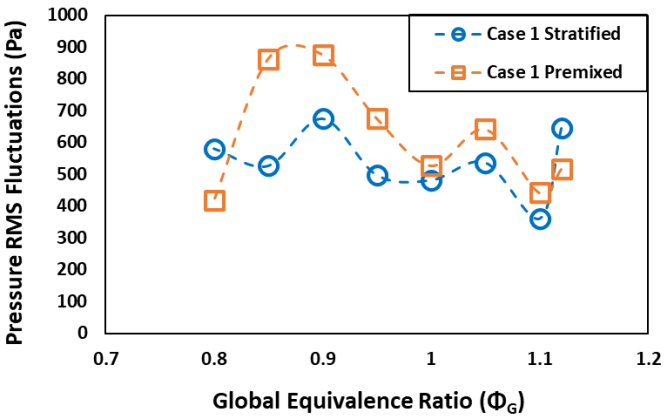

Fig. 3.16: Root mean square fluctuations in combustor pressure with changing global equivalence ratio for Case 1. (Best fit lines for clarity rather than modelled data).

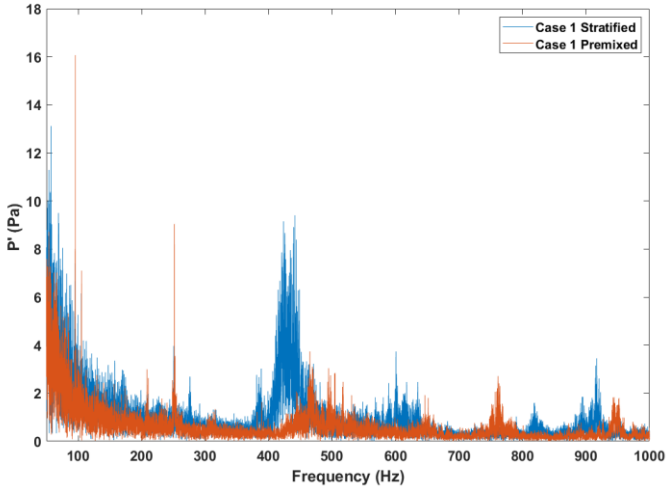

Fig. 3.17: Spectral comparison of Case 1 Stratified and Premixed at Φ_G = 1.05 above 50 Hz.

Both configurations experienced a significant pressure fluctuation at 95 Hz and 251 Hz, but stratification halved the amplitude when compared to the premixed configuration. Interestingly, the stratified configuration produced a peak at around 430 Hz which was not present in the premixed data. This newly excited instability could have been triggered by equivalence ratio fluctuations that a stratified flame experiences, as a premixed flame only experiences velocity fluctuations. These instabilities are too low frequency to be associated with the natural frequency of the combustor, which was calculated to be the broadband signature around 630 Hz present in both configurations.

3.4. Conclusions

The effect of supplying varying amounts of extra diffusive H_2 to the stratified flow of a 20 % cracked ammonia flame was investigated using a turbulent swirl burner, at a constant thermal power of 10 kW. Chemiluminescence data and numerical simulations were used to interpret changing emissions trends.

At stoichiometric and rich equivalence ratios, stratified configurations increased consumption of NO by NH_2 and reduced NO production from OH and HNO reaction pathways. The reduced OH intensity also resulted in an increase in unburned NH_3 emissions, which was offset by a significantly larger reduction in NO emissions. At slightly lean equivalence ratios, an increase in NO emissions was found, also due to changes in OH and NH production paired with diminished NH_2 intensity consuming less NO. Negligible N_2O was measured at all conditions as expected.

Emissions showed a strong sensitivity to the equivalence ratio of the stratified flow, related to diffusive flame temperature and NO – NH_2 residence times. Assuming an equal weighting for NO and unburned NH_3 emissions, the case where the diffusive flame had a slightly lean equivalence ratio showed better combined emissions performance.

Both examined configurations exhibited stable combustion. Whilst stratification generally reduced the amplitude of pressure fluctuations within the combustion chamber, it did also trigger new instabilities at different frequencies to the premixed flame which need to be properly assessed in further analyses.

4. Humidification

This chapter comprises the journal paper titled "Emissions analyses of humidified cracked ammonia swirling flames" published in Combustion and Flame. Further information is presented in the Statement of Authorship of Publications.

Its novelty lies in examining for the first time the effects of humidification on partially cracked ammonia flames and simultaneously measuring NO, NO_2, N_2O, NH_3 and H_2 while accounting for the volumetric dilution effect of steam. It also compares emissions from NH_3/H_2 flames and equivalent partially cracked ammonia flames. Furthermore, it demonstrates an industrially relevant swirl burner which raises steam using heat from the flame via an integrated heat exchanger. This is unlike previously published studies with NH_3/H_2 blends which used an external electrical heating system.

This chapter advances the aim of the thesis by addressing the overall theme of advancing the development of industrial swirl burners utilising partially cracked ammonia. It fully answers objective 1 and partially addresses objectives 2, 3 and 4. It assesses the impact including the nitrogen produced in the cracking process in the fuel blend has on emissions compared to a classic ammonia/hydrogen blend. It experimentally investigates a methodology for reducing emissions from partially cracked ammonia flames – humidification. It examines the resultant impact on unburned emissions of NH_3 and H_2 at globally rich conditions with humidification. It also uses a chemical reactor network to determine significant reactions responsible for the NOx reduction found. It is linked directly to Chapters 3 and 5 as they examine alternative NOx reduction methodologies using the same laboratory-scale atmospheric swirl burner.

Abstract

Using renewably produced ammonia as a zero-carbon fuel is gaining momentum due to its ease of transportation and storage as a hydrogen vector. This is particularly true for partially cracking ammonia immediately prior to use, injecting a blend of NH_3, H_2 and N_2. Challenges with this fuel combination relate to the emissions of NOx and unburned NH_3, as well as understanding flame stability for practical applications. In this study, a 20 $\%_{(vol.)}$ cracked ammonia blend was investigated using a fully premixed swirl burner, operating at a thermal power of 10 kW with steam injection of 30 $\%_{(vol.)}$ of the fuel and preheating inlet temperatures of up to 390 K, for a range of equivalence ratios from lean to rich. Emissions of NO, NO_2, N_2O, NH_3, H_2, O_2 and H_2O were

recorded, along with OH*, NH* and NH_2* chemiluminescence. Additionally, a numerical investigation was conducted using CHEMKIN-PRO to elucidate the main reactions responsible for reducing emissions by providing a rate of production analysis. The 20 $\%_{(vol.)}$ cracked ammonia blend was found to reduce NO, NO_2 and N_2O significantly, with an increase in NH_3 emissions at rich conditions and instabilities at both lean and rich extremes, compared to the widely investigated $70/30_{(vol\%)}$ ammonia/hydrogen blend. Humidification reduced NO and NO_2 emissions due to a reduction in HNO production via OH and NH but caused an increase in N_2O by reducing the flame temperature and unburned NH_3 emissions at rich, low power conditions due to combustion instabilities. Unburned H_2 emissions however were reduced, likely relating to a reduction in exhaust temperature thermally cracking less unburned NH_3 into H_2 and N_2.

4.1. Introduction

Green ammonia is gaining traction as a zero-carbon fuel for combustion in gas turbines, industrial burners and internal combustion engines as it is an effective and low-cost hydrogen carrier [112].

Low reactivity, emissions of NOx and unburned NH_3, and flame stability are the main challenges relating to the direct use of pure ammonia in large scale combustion systems. Research on ammonia as a fuel has increased rapidly in recent years [95,113] and has demonstrated the high ignition temperature and delay times [114], low flame speed [115] and associated narrow stability limits [52,87] can all be improved by blending ammonia with hydrogen. This is convenient because ammonia contains hydrogen, some of which can be separated out immediately prior to combustion through a partial cracking process at relatively low temperatures [116], possibly using waste heat from the combustor. A recent review on cracking [32] discussed a high-entropy alloy cobalt-molybdenum catalyst which could achieve the 20% NH_3 cracking required here at 350 °C. This catalyst was also significantly less expensive than conventional ruthenium-based catalysts. The review discussed iron-based catalysts which are even more affordable but need higher temperatures of >600 °C. Although blends of ammonia and hydrogen have been shown to have better fundamental combustion performance, NO_x emissions remain problematic unless operating at rich equivalence ratios which emit unburned ammonia [48,88]. Therefore, a significant body of research on limiting NOx emissions from ammonia/hydrogen flames has grown in recent years. Such experimental works include pressurisation, staging, stratification and humidification.

Pugh et al. [78] showed pressurisation of an NH_3/H_2 flame at an equivalence ratio of $\Phi = 1.2$ up to 0.185 MPa reduced NOx by nearly an order of magnitude to less than 100 ppmvd (15% O_2). It was

noted that increasing pressure also resulted in an increase in unburned NH_3 due to instabilities. In another study [79], they found at lean conditions pressurisation also reduced N_2O emissions from an enhancement of third body consumption, although significant NO emissions remained at this condition. Similar results were found for NO at lean conditions in [91] but it was noted that as equivalence ratio was reduced, the effect of pressure reducing NO became marginal. Although this study identified pressurised lean flames as a viable option for low NO, it did not measure N_2O emissions, which are known to increase as equivalence ratio is reduced, as presented in [79,92]. Furthermore, it must be noted that increasing pressure does not seem to have a great impact after a certain pressure value, as shown by Ditaranto et al. [92] who additionally demonstrated that NOx emissions flatten above pressures between 4 and 6 bar. On air staging in pure ammonia flames, Pugh et al. [89] demonstrated that while secondary air loading could provide favourable emissions, it could also cause an increase in NO and NO_2 emissions if not carefully controlled. Elbaz et al. [115] concluded that staging would likely require extensive retrofitting, suggesting single stage concepts would be more viable in the short term. Mashruk et al. [73] reported that stratifying the fuel streams by taking H_2 from the outer premixed flame and injecting it centrally as a diffusion flame reduced NO emissions by roughly 75% at $\Phi = 0.8$ when operating at 100% H_2 stratification.

Another, long-established method for reducing emissions from conventional fossil fuels is steam injection. Steam injection has been known to reduce NOx emissions and increase cycle efficiency in gas turbines operating on natural gas [74–76] and blends of methane and hydrogen [77]. There had been limited research on this effect in ammonia-based fuels until recently. Research by Pugh et al. on steam injection into NH_3/H_2 flames showed reduced NO and increased N_2O but noted water loading above 56% steam/fuel mass ratios caused blowoff [78,79]. Gutesa et al. [117] showed similar humidification ratios, finding out that NH_3/H_2 flames could withstand up to 72% steam/fuel mass ratio before blowoff occurred. This is an expected outcome as humidification has been shown to reduce laminar burning velocity in ammonia flames, reducing flame stability [118].

Knowledge of ammonia corrosion and degradation is important for practical application of ammonia combustion. Ammonia causes corrosion when exposed to metals such as copper, zinc, aluminium, and their alloys, so steel has been used for ammonia storage. However, ammonia contaminated by air increases the chances of stress corrosion cracking of steel, especially if it contains nickel or molybdenum [119,120]. To eliminate this condition, the addition of water in the range of 0.08% to 0.5% by weight has been shown to mitigate the effect of oxygen and act as an inhibitor of corrosion cracking of steel [121]. Recent studies [122,123] have proposed the use of

Inconel alloys for ammonia combustion and studied the impact of hydrogen embrittlement and nitration, although the detailed material science involved is still insufficient. Additionally, water vapor in the combustion exhaust gases is damaging to gas turbine blades. Research by Chen et al. [124] has shown that increased water vapor levels have a significant negative impact on the long-term durability of hot section components such as substrate blades, oxidation resistant coatings, thermal barrier coatings (TBCs), and environmental barrier coatings (EBCs). However, these issues need to be solved to facilitate combustion of any hydrogen-based fuel, which emit significantly more water vapour than an equivalent fossil fuel. The increase in water vapour in the exhaust from a small amount of steam injection to mitigate NOx emissions would be relatively small compared to the general conversion from fossil fuel to hydrogen-based fuels so would likely be compatible with new materials developed for zero-emission combustion without significant additional research requirements.

It should be noted that the partial cracking of ammonia results in the production of both hydrogen and nitrogen, which few of the above studies included. While the nitrogen can be removed using a molecular sieve, this adds cost and complexity to the combustion system. Therefore, the present work analyses the effect on emissions from keeping nitrogen in the fuel mixture. It also presents the first findings on emissions of NO, NO_2, N_2O and NH_3 from humidified ammonia/hydrogen/nitrogen flames. This is important as industrial applications of ammonia/hydrogen flames are likely to include the nitrogen fraction from the cracking process. Further novelty and relevance to industrial applications came from utilising an integrated system to raise steam using waste heat from the combustor, rather than using separate electric heaters.

4.2. Experimental and Numerical Setup

4.2.1. Swirl Burner

The optically accessible burner shown in Fig 4.1 was operated at a constant thermal power of 10kW for all conditions. An atmospheric blend of 70/30 $\%_{(vol.)}$ NH_3/H_2 was compared to 20 $\%_{(vol.)}$ cracked ammonia (66.7/25/8.3 $\%_{(vol.)}$ $NH_3/H_2/N_2$) for equivalence ratios $0.6 < \Phi < 1.4$. For industrial applications it is practical and cost effective to store only one fuel in the form of ammonia, then crack the hydrogen required to improve combustion characteristics immediately prior to combustion. However, the cracking process also produces nitrogen. Therefore, the effect on emissions from injecting this nitrogen into the flame as part of the fuel blend was investigated. As the ammonia cracking process produces three hydrogen molecules for each nitrogen molecule, 20 $\%_{(vol.)}$ cracked ammonia was selected for comparison with 70/30 $\%_{(vol.)}$ NH_3/H_2 as it gives a ratio of NH_3 to H_2 near to 70/3 $0\%_{(vol.)}$ as well as the required H_2:N_2 ratio of 3:1. The effects of preheating the air and fuel to 390 K and injecting steam at a ratio of 30 $\%_{(vol)}$ of the fuel were then examined. 390K was selected to ensure steam injected into the mixing chamber was maintained in the vapour phase.

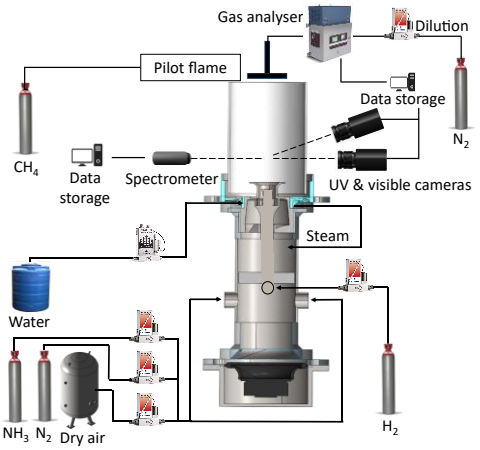

Fig 4.1: Simplified schematic of experimental setup (not to scale).

Fuel and air were supplied using Bronkhorst thermal mass flow controllers (± 0.5 % between 15-95 % of maximum flow) while liquid water was supplied using a Bronkhorst Coriolis mass flow controller. Water was boiled using waste heat from the burner and injected as steam into the plenum to mix with the preheated air and fuel. This mixture then flowed through the injector nozzle (d = 31.5 mm) via a radial-tangential swirler (S_g = 1.05), using a central injection lance (d = 22.5 mm) as a bluff body. The hydrogen was injected at the base of the swirler and mixed with the preheated air, fuel and steam as in [85]. The flame was confined within a quartz glass tube (d = 156 mm) to maintain optical access for chemiluminescence imaging and spectroscopy. The flame was monitored using a Logitech Brio camera from a distance of 5 m.

4.2.2. Exhaust Gas and Temperature Measurements

An Emerson CT5100 quantum cascade laser gas analysis system was used to measure NO, NO_2, N_2O, NH_3, O_2 and H_2O simultaneously at a temperature of 463K and sampling rate of 1 Hz (± 1% repeatability, 0.999 linearity). For all emissions, 120 samples were averaged over a two-minute period. When raw readings were above the analyser's range, N_2 was used to dilute the sample back into range (± 10 % repeatability) as explained in [85]. As the gas analysis system features independent detectors, it was possible to record and present the concentration of other pollutants which remained within range, undiluted and hence with improved uncertainty. Samples were collected from a sampling cross spanning the entire quartz confinement 25 mm above its exit and carried along a heated line to the analyser. Measured oxygen content was negligible with a stoichiometric flame, demonstrating no outside air was entrained into the sampling cross. Samples were captured wet and normalised to dry 15 % O_2 following (equation 10 in [101]. Ongoing discussion surrounds this emissions normalisation method due to the penalty against hydrogen-based fuels stemming from their increased water content in the exhaust gas, compared to carbon-based fuels. When this water content is removed to present dry emission values, the pollutants in the remaining mixture are more concentrated, increasing the apparent emissions on a dry, 15 % O_2 ppmv basis. A suggested alternative is to present emissions on a mass/power basis, e.g. mass of NO emitted per unit of thermal power [102]. Although the present study does not compare between hydrogen and carbon-based fuels, it does include both nitrogen and steam injection, which could dilute the exhaust gas sample and suggest that emissions were lower on a volumetric basis. To account for this dilution and enable a more representative comparison, emissions were also normalised on a mass/power basis, following the methodology presented by Douglas et al. [102].

4.2.3. Chemiluminescence Measurements

Time averaged images of the flame were recorded for OH* (309nm; $A^2\Sigma^+$-$X^2\Pi$ system) with a 310nm bandpass filter (10 nm FWHM), NH* (336 nm; $A^3\Pi$-$X^2\Sigma$ system) with a 337 nm bandpass filter (10 nm FWHM) and NH_2* (630 nm; single peak of NH_2 α band) with a 632 nm bandpass filter (10 nm FWHM) by two LaVision cameras each with a Sony ICX285AL sensor and Hamamatsu HB1058 intensifier). These cameras were triggered simultaneously at a sampling rate of 10 Hz for a period of 20 seconds. After subtracting the background and conducting a 3x3 pixel median filter, the images were averaged in Davis v10. Finally, the averaged images went through an Abel Deconvolution Matlab script [103] and were then normalised either to their own or the group

maximum. To aid in quantitatively assessing variations in flame morphology between operating conditions, a Matlab script for calculating the intensity weighted centroids of each flame image was written. This calculation accounted for both the distribution of pixels and their relative intensity.

The broad-band nature of the NH_2*, NO_2* [125] and H_2O* [126] which make up the visible range chemiluminescent signature in ammonia-fuelled flames has called into question the validity of using measurements of the NH_2* intensity as an indicator of ground state NH_2 concentration. The authors could not find any studies comparing NH_2 chemiluminescence and ground state NH_2 utilising PLIF. However, a recent study from Konnov [49] suggested that H_2O* was only significant in the near UV range, NO_2* intensity peaked below an equivalence ratio of 0.8 and that NO_2* intensity decreased as ammonia content increased. Another study from Weng et al. [17] agreed that at lean conditions, the visible chemiluminescence signature could be attributed to NO_2*, but only in the post-flame zone. In the flame zone, the signature was almost exclusively NH_2* at all equivalence ratios. Owing to the high ammonia content in the flames presented here, the relatively rich equivalences ratios of at least 0.8 and the chemiluminescence images being mainly of the flame zone, it was deemed appropriate to assume a positive correlation between the excited NH_2* intensity and ground state NH_2 concentration.

A collimating lens for UV/visible light was mounted 30mm above the burner outlet and 240 mm away from the central axis. Via a 600 µm fiber optic cable, it was connected to an Avaspec-ULS4096CL spectrometer with a 100 µm slit and 300 lines/mm grating, resulting in a 4.6 nm (FWHM) resolution. The spectrometer featured a 4096-pixel CMOS detector measuring 7 x 200 µm, which was set to an exposure time of 1 second and averaged over 20 scans to improve signal to noise ratio. Background scans were captured prior to flame ignition and subtracted from each datapoint. OH*, NH* and NH_2* intensities taken from the same ranges as the chemiluminescent images discussed above were captured and normalised to each species' maximum.

4.2.4. Chemical Reactor Network

To understand the most significant chemical reactions in the formation of emissions, one-dimensional numerical simulations of the flame were carried out using CHEMKIN-PRO. Five inlets for air, NH_3, H_2, N_2 and H_2O were used with four perfectly stirred reactors (PSR) modelling the pre-mixing, flame, central recirculation zone (CRZ) and external recirculation zone (ERZ). To simulate the reactions in the post-flame zone, the outlet of the flame zone PSR fed into a plug flow reactor (PFR). A diagram of the Chemical Reactor Network (CRN) is shown in Fig. 4.2 and further details including determination of recirculation strength can be found in [85,88,104]. As the same burner geometry was used with similar fuel blends, equivalence ratios and thermal powers as the previous study, the same CRN was deemed an appropriate starting point. To evaluate the contribution of different reactions in the production and consumption of NO and N_2O, absolute rate of production (ROP) values were used in the flame zone, and integrated values of production were used in the post flame zone. Initial heat loss values were estimated from thermocouple measurements and residence times from empirical flow calculations based on combustor volumes and modified to give favourable agreement with sampled concentrations at each condition. It should be emphasised that moderate uncertainty is associated with CRN modelling, and the CRN presented here was primarily used for qualitative analysis of trends found in the experimental results, rather than detailed prediction of untested conditions. Inlet temperatures always matched their equivalent experimental conditions. The reaction mechanism from Stagni et al. [63] with 31 chemical species and 203 reactions was selected as it showed good correlation with the experimental values in the present study, shown in the supplementary material Fig. 4.15, Fig. 4.16 and Fig. 4.18. It has also shown good performance in other recent studies [65,88,127].

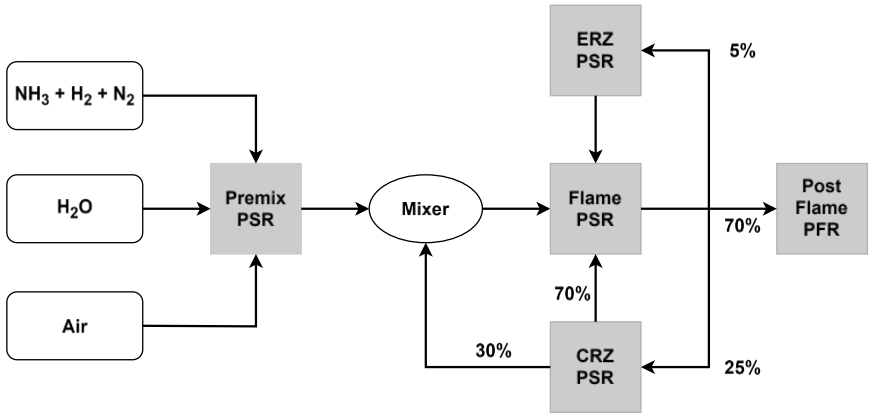

Fig. 4.2: Chemical reactor network (CRN)

4.3. Results and Discussion

4.3.1. Comparison of 20%$_{(vol.)}$ Cracked Ammonia with 70/30%$_{(vol.)}$ NH_3/H_2

As discussed previously, 20 %(vol.) cracked ammonia was chosen to compare the effects of adding the nitrogen from the cracking process into the fuel blend on emissions with a 70/30 %$_{(vol.)}$ NH_3/H_2 blend. This is because it maintains a similar blend of NH_3/H_2 while preserving the required ratio of hydrogen to nitrogen.

Fig. 4.3 shows sampled emissions of 70/30 %$_{(vol.)}$ NH_3/H_2 and 20 %$_{(vol.)}$ cracked ammonia across a wide range of equivalence ratios and compares the two normalisation methodologies outlined in Section 4.2.2 to assess the impact on emissions from nitrogen dilution in the cracked ammonia case. Emissions of NO and NO_2 followed the expected unimodal trend, peaking at Φ = 0.9 and 0.8, respectively. Both NO and NO_2 showed reduced emissions from the 20 %$_{(vol.)}$ cracked ammonia flame from both normalisation methodologies. Fig. 4.3 also shows N_2O emissions were negligible for both cases at Φ > 0.8, but below Φ = 0.8, the 20 %$_{(vol.)}$ cracked case showed a slight reduction in N_2O emissions. The emissions of unburned NH_3 showed the opposite relationship with equivalence ratio to the N_2O, instead showing negligible emissions below stoichiometry, and rapidly increasing at rich conditions. The cracked ammonia case emitted significantly more unburned ammonia than its equivalent ammonia/hydrogen blend. Fig. 4.3 also clearly demonstrates the narrower operating range for the 20 %$_{(vol.)}$ cracked ammonia. Due to flame instabilities arising from reduced reactivity in the lean zone, no emission data could be captured below Φ = 0.7, whereas the flame was still stable enough to capture emissions here for the 70/30 %$_{(vol.)}$ case. However, the beginnings of flame instability can clearly be seen, with unburned NH_3 arising at Φ = 0.7 for the 70/30 %$_{(vol.)}$ case.

One reason for the reduction in NO emissions from the 20 %$_{(vol.)}$ cracked flame shown in Fig. 4.3 relates to the flame morphology shown in Fig. 4.5. The 20 %$_{(vol.)}$ cracked flame stabilised closer to the central axis of the burner, suggesting the NH or NH_2 radicals would be more likely to consume the NO produced there, as suggested from NO PLIF measurements in [73], which used an identical burner geometry and flow rates as the 70/30 %$_{(vol.)}$ case presented here. This centralisation of flame stabilisation may be a result of the nitrogen addition, which increased the burner inlet velocity by 2 % and Reynolds number by 2.5 % at Φ = 0.8. The extra, relatively dense and inert nitrogen may have been captured in and disrupted the CRZ, preventing the flame from opening as much in the radial direction. Another reason for reduced NO emissions, particularly below stoichiometry, is related to flame temperature via NH and OH production. From the present CHEMKIN-PRO analysis, HNO is an intermediary chemical which can react with available

H radicals to form NO, as shown in Equation (*4-1*) and can be produced from the reaction in Equation (4-2). These equations continuously appeared as significant in the present CRN study and have previously been identified as important in other studies using the same burner configuration [85] and different configurations [92,126].

$$HNO + H \leftrightarrow NO + H_2 \quad (4\text{-}1)$$

$$NH + OH \leftrightarrow HNO + H \quad (4\text{-}2)$$

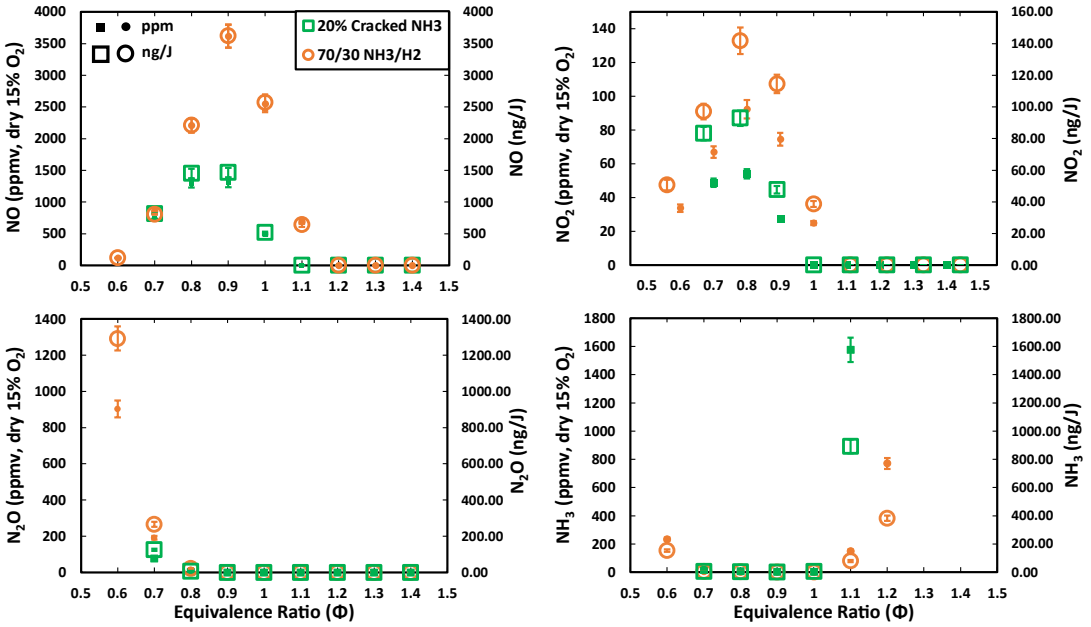

Fig. 4.3: Sampled emissions with changing equivalence ratio for 70/30%$_{(vol.)}$ NH_3/H_2 and 20%$_{(vol.)}$ cracked NH_3. NO (top left), NO_2 (top right), N_2O (bottom left) and unburned NH_3 (bottom right). Out of range NH_3 at rich conditions for both cases not plotted. Open and closed symbols refer to normalisation on a mass-power basis and a dry volumetric basis, respectively.

Fig. 4.5 shows the changes in radical formation between the two blends. Following previous studies [85] and discussed above in detail, the assumption of a positive correlation between ground state and emitting species was made for these three radicals. Although these images were normalised to their own maximum values, the images with poorer resolution and horizontal artefacts indicate lower signal intensity. The 20 %$_{(vol.)}$ cracked ammonia case had lower OH* and NH* intensity as expected from the reduced measured post flame zone temperatures in Fig. 4.4. It should be noted that these temperature measurements proved less reliable at very rich conditions, likely due to flame length effects becoming significant. For example, at very rich conditions, the humidified flame was significantly longer and therefore closer to the thermocouple than the base condition flame. Although this was a relatively modest reduction of roughly 30 K at Φ = 1.1, the added nitrogen would also consume more heat by raising the average specific heat capacity of the mixture, resulting in less heat being available for producing OH and NH for any given temperature. The reduction in reactivity from the presence of nitrogen would also

reduce ammonia oxidation. Ultimately, HNO formation and consequently NO formation was reduced. This is in agreement with the study from Zhu et al. [99], which suggested OH* intensities could be a good marker for NO emissions in NH_3/H_2 flames.

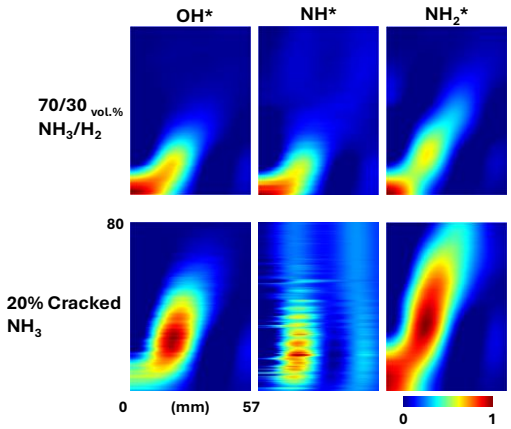

Fig. 4.5: Abel transformed chemiluminescence (OH, NH* and NH_2*) for 70/30%$_{(vol.)}$ NH_3/H_2 (top row) and 20%$_{(vol.)}$ cracked NH_3 (bottom row) at Φ = 0.8. Colourmap of chemiluminescence images normalised to each image's maximum intensity.*

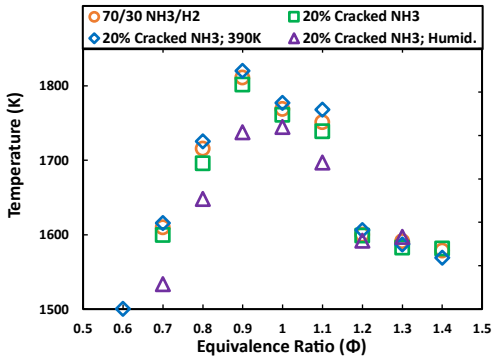

Fig. 4.4: Temperature captured by a thermocouple in the post-flame zone against equivalence ratio for each of the four cases considered. (Corrected for radiative and convective heat losses from the thermocouple).

Fig. 4.6 shows the NO rate of production (ROP) in the flame zone for the two cases, calculated in CHEMKIN-PRO using the CRN shown in Fig. 4.2. The NO dependence on NH and OH via HNO was validated in Fig. 4.6, which shows that when the NO consuming reaction of Equation (*4-3*) was approximately equal for both cases, Equation (*4-1*) was less than half for the 20 %$_{(vol.)}$ cracked NH_3 case.

$$NH + NO \leftrightarrow N_2O + H \qquad (4\text{-}3)$$

It should be noted that in Fig. 4.6 and Fig. 4.7, the 70/30 %$_{(vol.)}$ NH_3/H_2 and 20 %$_{(vol.)}$ cracked ammonia cases were each normalised by their own maximum ROPs to aid in visual comparison of the relative differences between reactions across both cases. The aim here was not to compare

absolute values of ROP for each reaction, but to assess the differences in relative importance of each reaction between the two cases.

Fig. 4.5 also shows an increase in distribution of NH_2* intensity for the 20 % $_{(vol.)}$ cracked NH_3 case, which would ordinarily reduce NO emissions from the consumption reactions of Equations (*4-4*) and (*4-5*). However, the rate of production analysis showed that for these two specific cases, at a lean equivalence ratio of Φ = 0.9 where NH_2* intensity was relatively low, these reactions were not significant, unlike at rich conditions. Instead, at slightly lean conditions, NH and atomic nitrogen were mainly responsible for NO consumption.

$$NH_2 + NO \leftrightarrow N_2 + H_2O \quad (4\text{-}4)$$

$$NH_2 + NO \leftrightarrow NNH + OH \quad (4\text{-}5)$$

It is also important to note that the equivalence ratio at which negligible measured NO was reached reduced from Φ = 1.2 to Φ = 1.1. Also shown in Fig. 4.3, the peak of 142 ng/J of NO_2 was found at Φ = 0.8 for the 70/30 %$_{(vol.)}$ NH_3/H_2 case and was roughly 50 % larger than the peak value in the 20 %$_{(vol.)}$ cracked NH_3 case. This demonstrates a similar relationship between the cases for NO_2 and NO, but with a smaller difference.

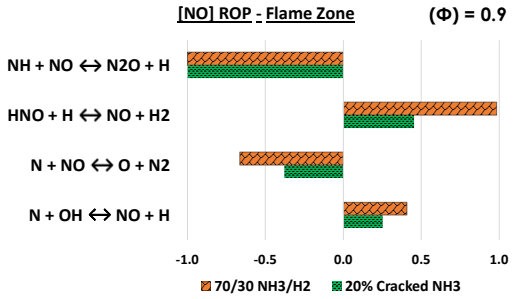

Fig. 4.6: Flame zone rate of production (ROP) for the most significant NO reactions for 70/30%$_{(vol)}$ NH_3/H_2 (orange) and 20%$_{(vol.)}$ cracked NH_3 (green).

The N_2O reduction shown for the 20%$_{(vol.)}$ cracked case in Fig. 4.3 is also related to flame morphology. On a temperature basis, the addition of N_2 into the fuel slightly reduces the reactivity and hence flame speed, elongating the flame as shown in Fig. 4.5. Fig. 4.7 shows the N_2O ROP in both the flame zone and post-flame zone for the two cases, calculated using the CRN shown in Fig. 4.2. It shows that in the flame zone, consumption of N_2O by Equation (4-7) was 11 % higher for the 20 %$_{(vol.)}$ cracked ammonia case, over the 70/30 %$_{(vol.)}$ NH_3/H_2 case. This compounds with the longer 20 %$_{(vol.)}$ cracked flame providing the increase in residence time that Equation (4-7) requires [85], as well as a larger flame volume to act in. There was a 3 % reduction in consumption of N_2O via Equation (*4-6*) for the 20 %$_{(vol.)}$ cracked ammonia case, which was expected as the required free H atom availability for that reaction is temperature dependent, and the cracked

ammonia case had a cooler temperature, shown in Fig. 4.4. Fig. 4.7 also showed that although consumption of N_2O was slightly lower in the post flame zone for the 20%$_{(vol.)}$ cracked NH_3 case, it was not enough to offset the increase in consumption found in the flame zone.

$$N_2O + H \leftrightarrow N_2 + OH \quad (4\text{-}6)$$

$$N_2O + (M) \leftrightarrow N_2 + O + (M) \quad (4\text{-}7)$$

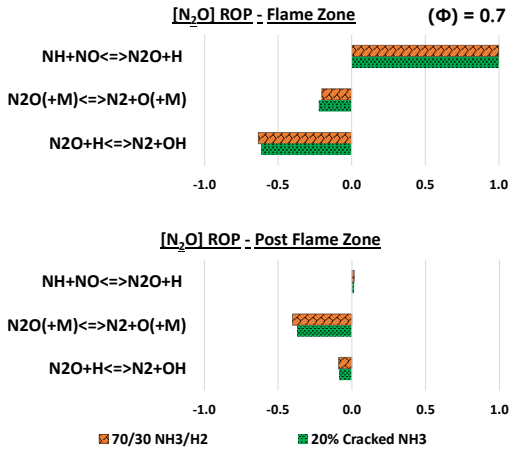

Fig. 4.7: Absolute and integrated ROPs of flame zone (top) and post flame zone (bottom) for the most significant N_2O reactions for 70/30%$_{(vol.)}$ NH_3/H_2 (orange) and 20%$_{(vol.)}$ cracked NH_3 (green).

The same mechanism affected emissions of unburned NH_3, with the 20 %$_{(vol.)}$ cracked case producing a roughly 600 % increase in NH_3 slip over the 70/30 %$_{(vol.)}$ NH_3/H_2 blend at Φ = 1.1. This alone demonstrates the reduction in measured NOx emissions is not solely the result of diluting the exhaust gas sample with the added nitrogen, as that would have also reduced NH_3 emissions. The right-hand axis in Fig. 4.3 confirms this, showing on a mass/power basis, nitrogen dilution had a relatively small effect on emissions and all trends were maintained across both methodologies. This was to be expected considering the small amount of nitrogen injected – just 2.3 % of the total inlet mass flow at stoichiometry. When further increasing the equivalence ratio above Φ = 1.1, the unburned NH_3 values for both blends were higher than the gas analyser limit and are therefore not present on this plot.

These findings of reduced NO and NO_2 but increased NH_3 emissions indicate that using 20%$_{(vol.)}$ cracked ammonia as a fuel in a single stage burner would have to be at an equivalence ratio of less than 1.1, at which point NO emissions become an issue again. Therefore, a potential NO mitigation strategy of humidification was investigated in more detail.

4.3.2. Effect of Varying Inlet Temperature and Humidification on 20%$_{(vol.)}$ cracked NH_3

In this section, only the 20 %$_{(vol.)}$ cracked NH_3 case was examined. First, inlet temperatures were increased from 295 K to 390 K. Then, steam injection was investigated, with a volumetric H_2O fraction in the fuel of 30 % whilst maintaining the higher inlet temperature of 390 K. The inlet temperature was maintained at 390 K for the humidification case so that the steam generated within the burner head would not condense back into liquid water upon injection into the premixing chamber. As a result, the quenching effect of water vaporisation within the flame would be minimal due to effective experimental design – only steam is injected into the flame, with no water droplet transport. Furthermore, wall cooling of the face plate due to waste heat being used to vaporise water into steam was accounted for in the CRN with changes in simulated heat loss.

Fig. 4.8 shows the emissions results from these three cases. As in Section 4.3.1, the NO and NO_2 emissions from each case followed the same unimodal shape, peaking around Φ = 0.9 and Φ = 0.8, respectively. NO and NO_2 also have the same trend, with the emissions increasing with increased inlet temperature, and then reducing with the injection of steam, compared to the base case of 20 %$_{(vol.)}$ cracked NH_3 at 295 K inlet temperature. All three cases reached negligible NO emissions at Φ = 1.1. N_2O emissions were all negligible at and above Φ = 0.8, apart from for the humidified case, which additionally proved significantly higher than the other two cases at Φ = 0.7. Here, the case with increased inlet temperature emitted half of the N_2O. For all cases, both unburned fuels were undetectable at and below stoichiometry, but began to rapidly increase above Φ = 1. The NH_3 emissions for the humidified case were notably high, and all three cases were above the gas analyser's dilution range already at Φ = 1.2 and are therefore not present in Fig. 4.8. This was likely due to decreased reactivity as discussed in Section 4.3.1.

Interestingly, trends inverted between unburned NH_3 and H_2. For NH_3, humidification resulted in higher emissions than the base case and increased inlet temperatures resulted in lower emissions. The opposite was true for emissions of unburned H_2, but these results are likely related. The approximately 50 K lower temperature post-flame zone measured in Fig. 4.4 for the humidified case at Φ = 1.1 could result in less of the unburned NH_3 being thermally cracked into H_2 and N_2 in the absence of oxygen in the exhaust. This would result in higher unburned NH_3 and lower unburned H_2 than the base case, as shown in Fig. 4.8. Above Φ = 1.3, unburned H_2 emissions began to reduce, which could also be related to generally lower post flame zone temperatures cracking less NH_3 into H_2 and N_2, regardless of injection temperature or humidification. Fig. 4.8 also demonstrates an increase in flame stability when the inlet temperature was increased to 390K, with emissions stable enough to measure at Φ = 0.6. At this

same equivalence ratio in Fig. 4.3, unburned NH_3 emissions were significant, demonstrating the flame instability. However, the 20 $\%_{(vol.)}$ cracked NH_3 case at an inlet temperature of 390 K had comparatively far lower NH_3 emissions, suggesting that the reduction in stable operating range from the nitrogen present in cracked ammonia flames was compensated by an increase in inlet temperature of just 100 K.

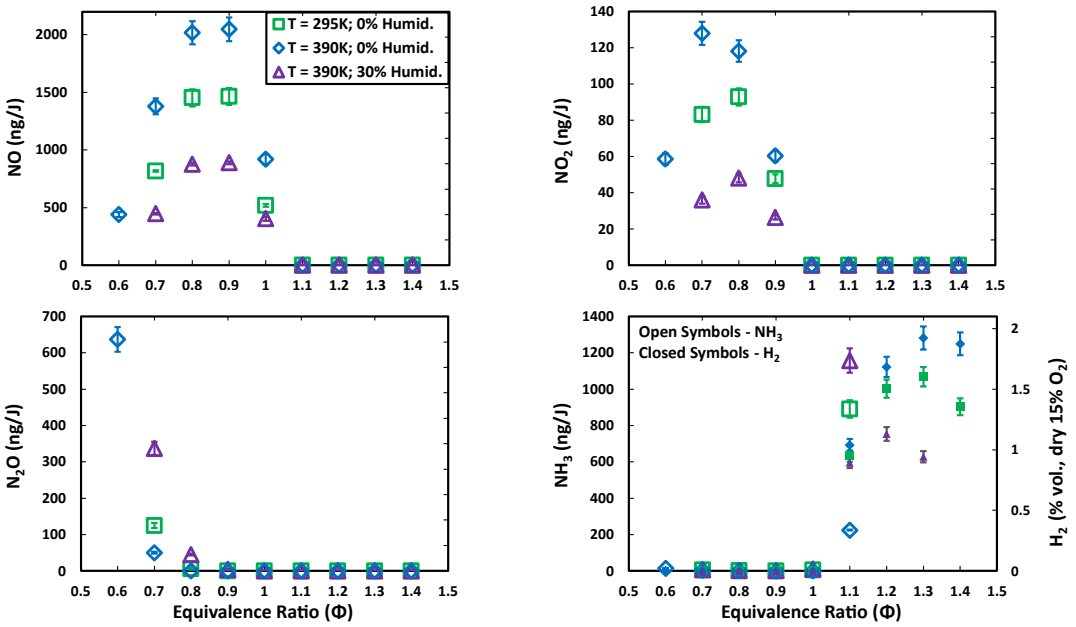

Fig. 4.8: Sampled emissions with changing equivalence ratio for 20%$_{(vol.)}$ cracked NH_3 at ambient and increased inlet temperature and with humidification. NO (top left), NO_2 (top right), N_2O (bottom left) and unburned NH_3 and H_2 (bottom right). Out of range NH_3 at rich conditions not plotted for all three cases.

To reduce graph complexity, emissions are presented only on a mass/power basis in Fig. 4.8 as it provides a more representative comparison than a dry volumetric basis by accounting for both nitrogen and steam dilution in the exhaust gases for all emissions apart from H_2. In order to calculate non-zero emissions on a mass/power basis, the concentration of all exhaust gases must be known. As unburned NH_3 was not measurable above $\Phi = 1.1$, H_2 emissions could not be calculated in ng/J, so are presented here as dry, 15 % O_2 volumetric percentage.

However, at $\Phi = 1.1$, both unburned NH_3 and H_2 were measurable at the same time. To check whether steam dilution influenced emissions results here, the H_2 emissions were calculated on a mass/power basis. Fig. 4.9 below shows NH_3 and H_2 emissions at $\Phi = 1.1$, as well as calculated combustion efficiency for each of the three cases from Equation (4-8). It shows the same inversion of trends as shown for 15 % O_2, dry, proving that dilution from H_2O (discussed in detail in Section 4.2.2) did not change the trends shown in Fig. 4.8. These H_2 values also emphasise that although ~1 % emission of H_2 appears exceptionally high, they can be explained by hydrogen's

low density, and on a mass/power basis, emissions of H_2 are similar to those of unburned NH_3. Fig. 4.9 also shows that despite the inversion of trends of emissions of NH_3 and H_2, the combustion efficiency follows the expected trend of elevated inlet temperature having higher efficiency, and humidification having lower efficiency than the base 20 $\%_{(vol.)}$ cracked case. None of the cases emitted detectable amounts of unburned fuel at $\Phi < 1.1$, resulting in combustion efficiencies of 100%. All cases produced too high emissions of unburned NH_3 to measure at $\Phi > 1.1$, so combustion efficiency could not be calculated.

$$\eta = 1 - \frac{\dot{m}(NH_3 + H_2)_{out}}{\dot{m}(NH_3 + H_2)_{in}} \tag{4-8}$$

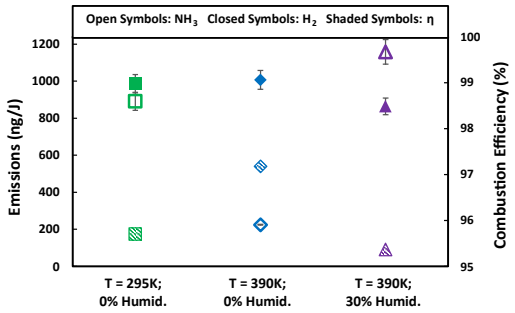

Fig. 4.9: Sample emissions of unburned NH_3 and H_2 and resulting combustion efficiency at $\Phi = 1.1$ for each case.

Fig. 4.10 shows the intensity and spatial variations of OH*, NH* and NH_2* from the three cases at $\Phi = 0.9$. Each set of OH*, NH* and NH_2* images was normalised to the maximum intensity found for each species across all three cases. Here, that was found in the T = 390 K; 0% Humid. case. This methodology is useful as it allows the variations in intensity to be compared qualitatively, while simultaneously maintaining enough information within each image to identify any spatial differences. If the images were not normalised to each species' maximum intensity, no correlations with the ROP calculations could be drawn. Fig. 4.11 shows the variations in rate of production and consumption of NO in the flame zone for the three cases, also at $\Phi = 0.9$. Here, the reason for the increase in NO when inlet temperature was increased to 390 K and the significant reduction for the humidified case can be explained, as OH* and NH* followed the same trend as NO for these cases in Fig. 4.8. Again, from Equation (*4-2*), an increase in NH and OH promotes HNO formation which ultimately forms NO, as demonstrated for the 390K case in Fig. 4.11. This is further validated by Equation (*4-9*), which consumes OH and rose for the 390K case and decreased for the humidified case in Fig. 4.11.

$$N + OH \leftrightarrow NO + H \tag{4-9}$$

The significant reduction in NO this caused for the humidification case should be highlighted, as the peak NO was measured as below 900 ng/J. As in Section 4.3.1, the "de-NOxing" [128] effect of NO reduction from NH_2 in the reactions in Equations (*4-4*) and (*4-5*) were found to be not particularly significant at the lean condition (Φ = 0.9) considered here, with an increase in inlet temperature, nor with humidification and are therefore not shown in Fig. 4.11. This was expected due to the relative lack of NH_2 intensity at lean conditions, compared to rich.

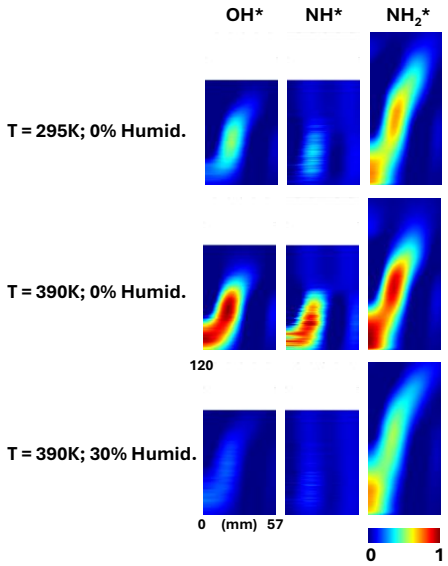

Fig. 4.10: Abel Transformed chemiluminescence (OH, NH* and NH_2*) for 20%$_{(vol.)}$ cracked NH_3 at ambient (top row), increased inlet temperature (middle row) and with humidification (bottom row) at Φ = 0.9. Colourmap of chemiluminescence images normalised to the species dataset maximum.*

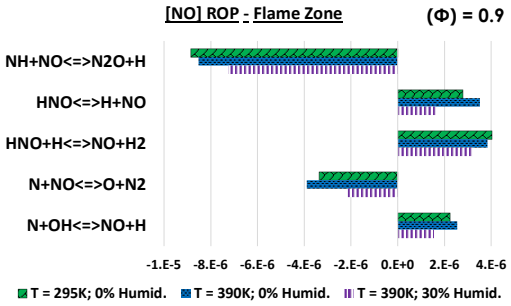

Fig. 4.11: Flame zone rate of production (ROP) [Unit – mole/cm^3-sec] for the most significant NO reactions for 20%$_{(vol.)}$ cracked NH_3 at ambient and increased inlet temperatures, and with humidification.

Interestingly, humidification was even more effective at reducing NO_2 emissions than NO emissions. While the NO emissions were reduced by 40 %, the NO_2 emissions were halved. An in-depth ROP analysis to determine the reasoning behind this enhanced reduction in NO_2 emission was not possible due to the employed kinetic reaction mechanism not accurately capturing NO_2 concentrations, shown in Supplementary Material Fig. 4.17. However, it is hypothesised that the reaction in Equation (*4-10*) could have played a role as increased

concentration of H_2O from steam injection might have provided more free O atoms to consume NO_2.

$$NO_2 + O \leftrightarrow NO + O_2 \quad (4\text{-}10)$$

The sub-optimal mechanism performance in predicting NO_2 concentrations has been noted in the literature previously [88], with it being suggested that the mechanisms may not accurately account for ammonia's high third body efficiency enhancing the conversion of NO into NO_2, through the reaction shown in Equation (*4-11*).

$$NO + O + (M) \leftrightarrow NO_2 + (M) \quad (4\text{-}11)$$

In Fig. 4.8, N_2O halved for the T = 390 K case and more than doubled for the humidified case – relative to the base 20 $\%_{(vol.)}$ cracked ammonia case – and can be explained by considering the flame length and free H radical availability. Fig. 4.12 shows the differences in intensity weighted centroid of captured OH* at two different equivalence ratios for each of the cases. Together with Fig. 4.9, they qualitatively and quantitively demonstrate that for both equivalence ratios, the flame shortened with an increase in inlet temperature and lengthened with humidification, in line with the temperatures shown in Fig. 4.4. Fig. 4.12 also shows the humidified flames were narrower radially, stabilising closer to the central axis of the burner. Furthermore, it shows the significant difference in flame length between Φ = 0.7 and Φ = 0.9 for all three cases, suggesting equivalence ratio played a larger role in varying the flame morphology than humidification did. The significant difference in flame length between the two equivalence ratios could also explains the larger differences between cases at Φ = 0.9 compared to Φ = 0.7. OH* chemiluminescence was selected for comparing the intensity weighted centroid locations instead of NH_2* due to Φ = 0.7 being presented. As discussed in Section 4.2.3, at very lean conditions, the influence of NO_2* in the visible spectrum may become significant when compared to NH_2*. However, the same trends in centroid variations across conditions shown in Fig. 4.12 for OH* were also found for NH* and NH_2* centroids.

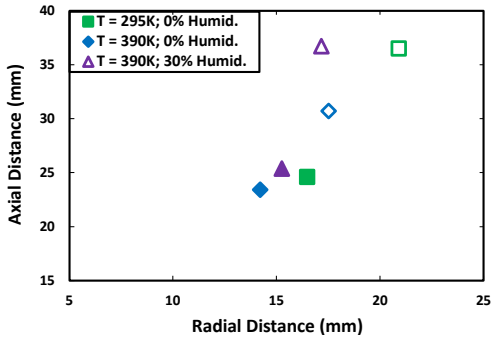

Fig. 4.12: Intensity weighted centroid locations of Abel transformed OH chemiluminescence images at Φ = 0.9 (empty symbols) and Φ = 0.7 (filled symbols).*

Fig. 4.13 shows the rate of production and consumption of N_2O in both the flame zone and post-flame zone, calculated using the CRN in Fig. 4.2 for all three cases. N_2O was mostly produced in the flame zone, shown by Equation (*4-3*) in Fig. 4.13. In the post flame zone, the effect of the third body reaction (Equation (*4-7*)), requiring a longer residence time [85] is evident. As the humidified flame was longer, the required residence time was met and so more N_2O could be consumed. Conversely, the higher temperature, shortened flame of the 20 $\%_{(vol.)}$ cracked NH_3 at 390K inlet temperature showed less consumption from the third body reaction equation. In the flame zone it appears that the reverse trend is followed, but the units of the ROP (mole/cm^3-sec) must again be considered. As the humidified flame is longer, it must also have a larger flame volume and residence time. Therefore, this apparently lower ROP is likely to result in more N_2O being consumed as the ROP has a larger volume and longer time to act in. Ultimately, the largest consuming reaction was found to be in the flame zone, with Equation (*4-6*). The free hydrogen atom requirement for this reaction has a high temperature requirement, demonstrated with the lowest temperature humidified case having the lowest negative ROP.

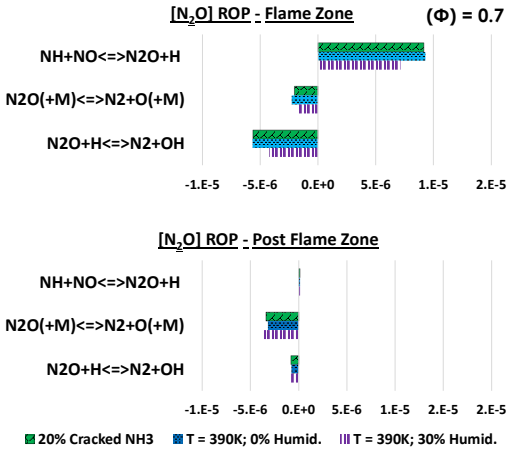

Fig. 4.13: Absolute and integrated ROPs of flame zone (top [Unit – mole/cm^3-sec]) and post flame zone (bottom [Unit – mole/cm^2-sec]) for the most significant N_2O reactions for 20$\%_{(vol.)}$ cracked NH_3 at ambient and increased inlet temperatures, and with humidification.

To validate the chemiluminescence images and to concisely show how spectral signatures vary with equivalence ratio, the chemiluminescence emission from the flame was recorded using an optical spectrometer, shown in Fig. 4.14. Fig. 4.14 follows the same trend as the chemiluminescence images in Fig. 4.10, in that the 390 K inlet temperature case had the highest intensity, followed by the 295K case and with the humidified case having the lowest. The OH* and NH* intensities follow the same unimodal curve with the peak between Φ = 0.8-1.0 as the NO emission curve in Fig. 4.8, suggesting they could be used as a rough analogue for NO emissions if a relatively low-cost spectrometer is the only diagnostic tool available. It also again evidences the role OH and NH have in NO production via the HNO reactions. From a practical perspective, the slight variation in peaks of OH* and NH* between the three cases is worth highlighting. For

the base 20%$_{(vol.)}$ cracked ammonia case, OH* and NH* peaked at Φ = 0.9 and 1.0, respectively. However, for the two other cases of elevated temperature and 30% humidification, both chemiluminescence peaks were shifted leaner, to Φ = 0.8 and 0.9. NH_2* rose sharply above Φ = 1.0 for all three cases, at which point the NH_2 reactions' (Equations (*4-4*) and (*4-5*)) role in NO consumption more than doubled. The previously mentioned shift in peak chemiluminescent intensity found for OH* and NH* was not found for NH_2*, as all three cases peaked at Φ = 1.2.

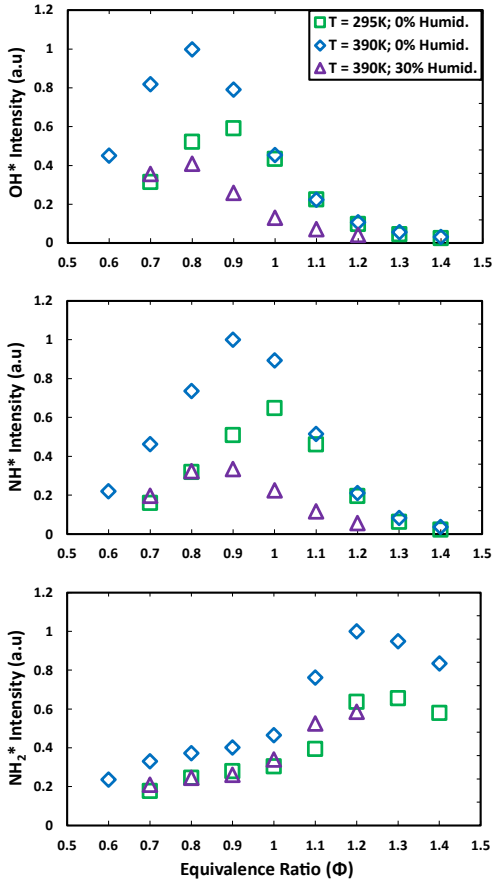

Fig. 4.14: Normalised optical spectrometry results for OH, NH* and NH_2* chemiluminescence against equivalence ratio for 20%$_{(vol.)}$ cracked NH_3 at ambient and increased inlet temperatures, and with humidification.*

Fig. 4.8 shows a decrease in NO emissions in very lean conditions, seemingly suggesting viability for low emission cracked NH_3 flames. However, there is also an increase in N_2O emissions. Insulating refractory material found in gas turbines, boilers and furnaces would likely reduce heat loss in higher power flames, leading to higher temperatures in both the flame and post flame zones. From Equation (*4-6*), N_2O emissions might be reduced further with reduced heat loss [81]. Unfortunately, higher temperatures reducing N_2O would be offset by producing more NO from the HNO reactions discussed previously across Sections 4.3.1 and 4.3.2. This highlights the necessity of operating ammonia flames at more rich conditions to reduce emissions of NO, NO_2 and N_2O to negligible quantities simultaneously, as the present work has demonstrated, with

possible operation at a leaner equivalence ratio (Φ = 1.1) than previously found. Although humidification was also shown to reduce H_2 emissions, to reduce unburned NH_3 emissions concurrently, the mechanisms which cause instabilities at the slightly rich condition need to be understood and controlled in a future study. Humidification appears to complement other methodologies for reducing NO emissions such as axial staging and needs to be investigated concurrently.

4.4. Conclusions

In this study, the emissions performance from a 70/30 $\%_{(vol.)}$ NH_3/H_2 blend was experimentally and numerically compared with a 20 $\%_{(vol.)}$ cracked NH_3 blend. The 20 $\%_{(vol.)}$ cracked NH_3 had 50 % lower peak NOx emissions mainly due to changes in flame morphology and temperature, but increased unburned NH_3 slip, as well as narrower stability regions due to a reduction in reactivity.

The 20 $\%_{(vol.)}$ cracked NH_3 blend was then investigated more thoroughly by examining the effects of increased inlet temperature and 30 $\%_{(vol.)}$ fuel humidification. With an increase in inlet temperature, NO and NO_2 increased due to thermal NOx production and an increase in OH and NH forming HNO. However, stability limits were widened and N_2O emissions decreased due to the enhancement of H radical production breaking down N_2O to N_2.

With humidification, peak NO and NO_2 emissions decreased by 40% and 48%, respectively, mainly due to a reduced production of OH and NH. Little difference between cases was found in NO consumption by NH_2 here at Φ = 0.9 as NH_2* intensity was relatively low.

Humidification also caused N_2O emission to more than double at the very lean condition due to a reduction in the availability of free H radicals from lower flame temperatures, despite a longer flame enabling the third body reaction to consume more N_2O. Unburned NH_3 emission was higher at rich humidified conditions due to reduced reactivity which resulted in flame instabilities. Unburned H_2 emission was reduced, likely resulting from reduced temperatures in the exhaust thermally cracking less of the unburned NH_3 into H_2 and N_2.

4.5. Supplementary Material

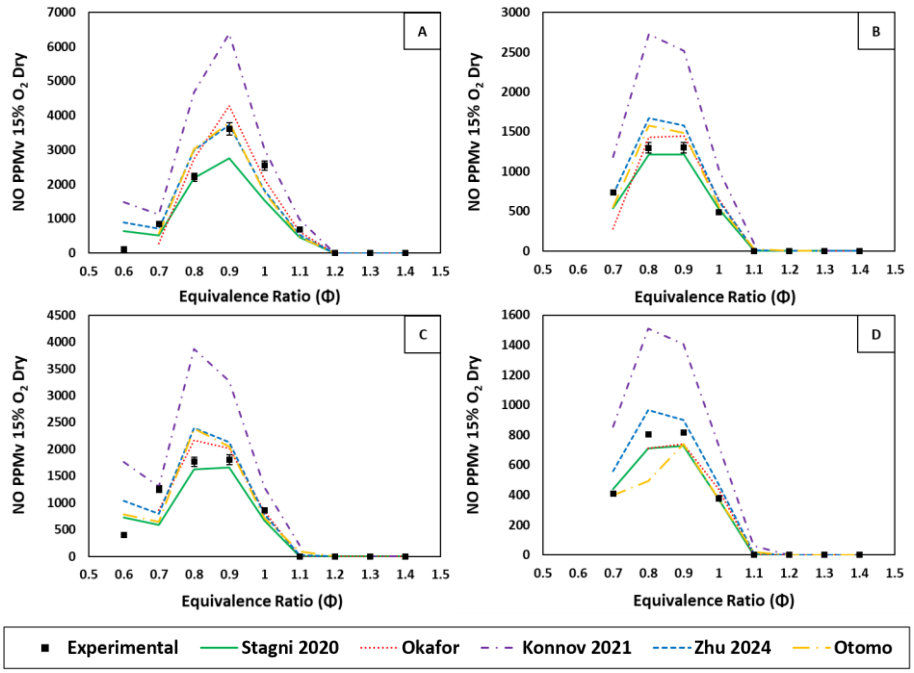

Fig. 4.15: Comparison between experimental results and mechanism predictions of NO for 70/30 NH_3/H_2; T = 295K (A), 20% Cracked NH_3 at T = 295K; 0% Humid (B), 20% Cracked NH_3 at T = 390K; 0% Humid (C) and 20% Cracked NH_3 at T = 390K; 30% Humid (D)

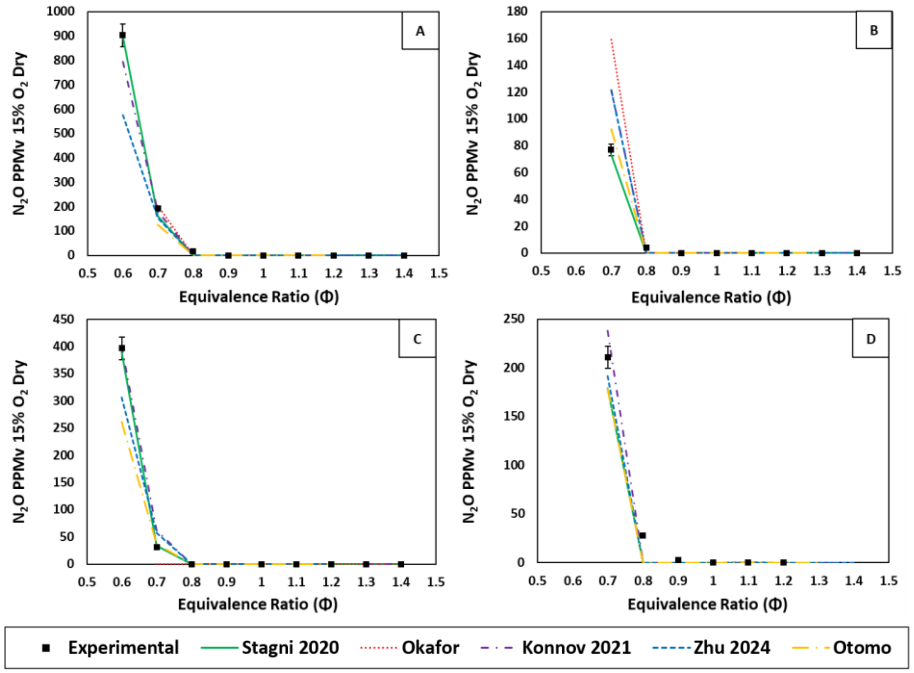

Fig. 4.16: Comparison between experimental results and mechanism predictions of N_2O for70/30 NH_3/H_2; T = 295K (A), 20% Cracked NH_3 at T = 295K; 0% Humid (B), 20% Cracked NH_3 at T = 390K; 0% Humid. (C) and 20% Cracked NH_3 at T = 390K; 30% Humid. (D)

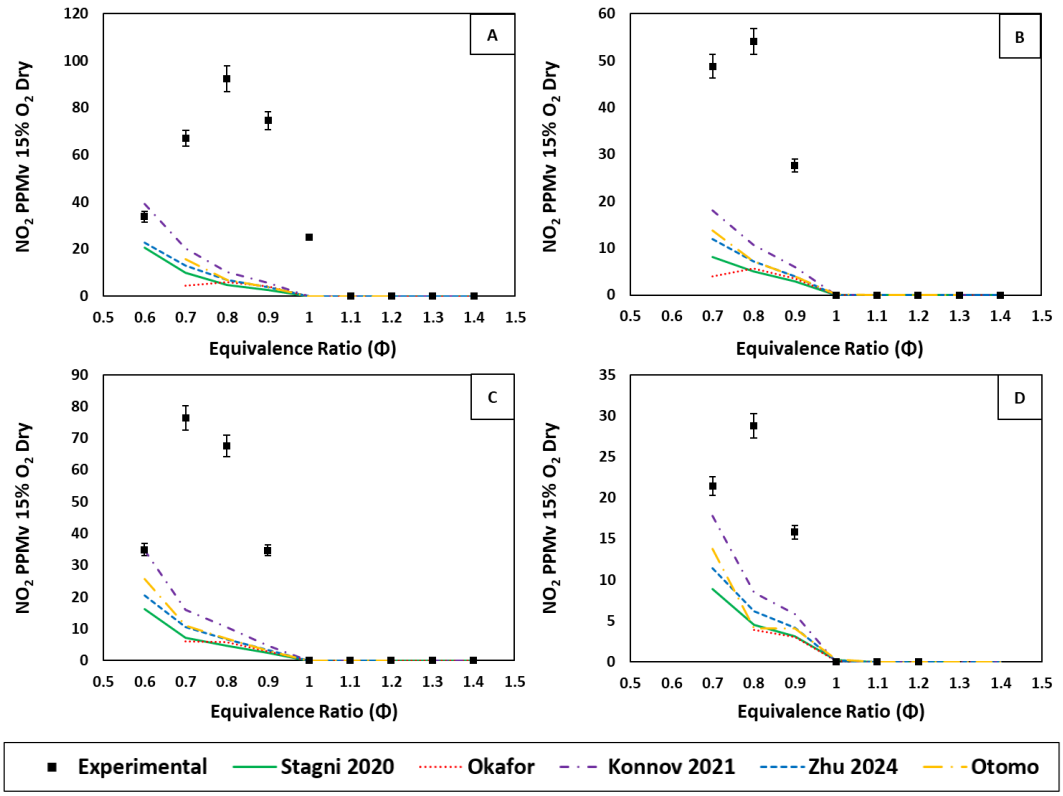

Fig. 4.17: Comparison between experimental results and mechanism predictions of NO_2 for70/30 NH_3/H_2; T = 295K (A), 20% Cracked NH_3 at T = 295K; 0% Humid (B), 20% Cracked NH_3 at T = 390K; 0% Humid. (C) and 20% Cracked NH_3 at T = 390K; 30% Humid. (D)

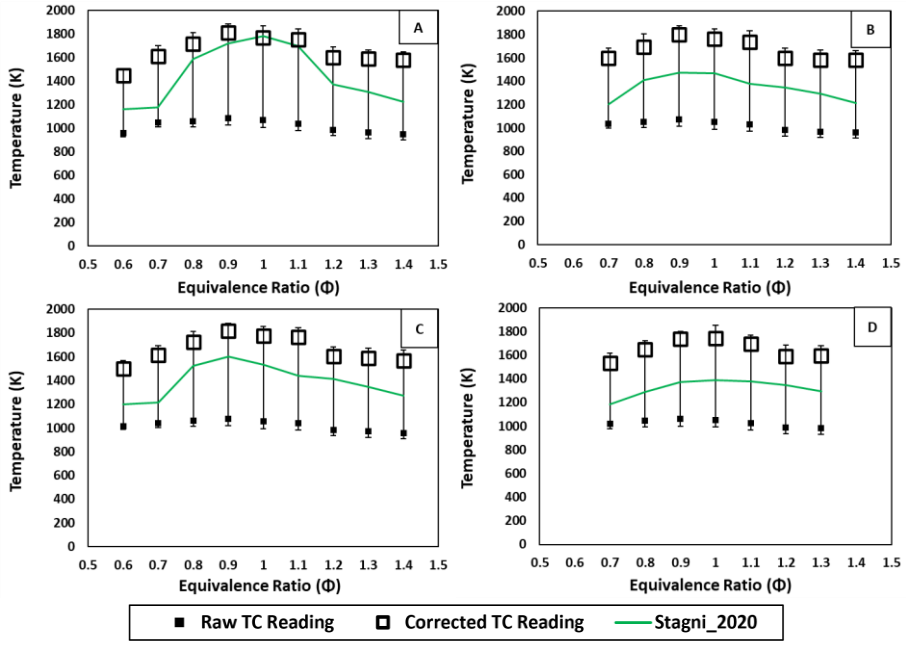

Fig. 4.18: Comparison between experimental results and mechanism predictions of post flame zone temperature for 70/30 NH_3/H_2; T = 295K (A), 20% Cracked NH_3 at T = 295K; 0% Humid (B), 20% Cracked NH_3 at T = 390K; 0% Humid. (C) and 20% Cracked NH_3 at T = 390K; 30% Humid. (D)

5. Heat Loss Management

This chapter comprises the journal paper titled “Control of emissions from cracked ammonia swirling flames by heat loss management” under review in International Journal of Hydrogen Energy. Further information is presented in the Statement of Authorship of Publications.

Its novelty lies in investigating the effect of heat loss on emissions from partially cracked ammonia flames or ammonia/hydrogen blends for the first time. Furthermore, it is the first time heat loss has been used as a NOx control methodology, rather than a passive effect. It does this by targeting the optimal temperature range for NH_2 to consume NO (DeNOx reactions) in the external recirculation zone. It also links lab-based research to practical combustion systems with significant heat loss (e.g. future systems with integrated ammonia vaporisers or crackers, as well as conventional steam boilers),

This chapter advances the aim of the thesis by addressing the overall theme of advancing the development of industrial swirl burners utilising partially cracked ammonia. It partially addresses objectives 2, 3 and 4. It assesses the impact of a novel NOx reduction methodology – heat loss management. It examines the resultant impact on unburned emissions of NH_3 and H_2 at globally fuel rich conditions with additional heat loss. It also uses a chemical reactor network to determine significant reactions responsible for the NOx reduction found. It is linked directly to Chapters 3 and 4 as they examine alternative NOx reduction methodologies using the same laboratory-scale atmospheric swirl burner.

Abstract

Implementation of renewably produced ammonia as a zero-carbon fuel faces challenges relating to emissions of NOx and unburned NH_3. This study employs a premixed atmospheric swirl burner with integrated cooling channels to examine the effects on emissions of NO, NO_2, N_2O, NH_3 and H_2 by managing heat loss from the flame. A blend of 0.67/0.25/0.08 $_{(mol.)}$ $NH_3/H_2/N_2$, representing 20 % $_{(vol.)}$ cracked ammonia was used with a constant net thermal power of 10 kW. For the range of equivalence ratios $0.7 < \Phi < 1.3$, two heat loss cases were assessed. A comparison was made between a conventional baseline configuration, and a secondary case with additional heat loss added by flowing 16 g/s of water through the burner face. A previously developed chemical reactor network (CRN) was utilised to investigate the main reactions responsible for emissions differences. Due to a reduction in availability of free H atoms caused by lower temperatures from

additional heat loss, N_2O emissions at lean conditions were increased. Therefore, focus was shifted to slightly rich conditions instead. NO emissions at Φ = 1.1 were found to be 67 % lower with additional heat loss when compared to the base case. One reason for this was a reduction in NO production via the HNO pathway, also stemming from lower temperatures. More interestingly, the increased heat loss moved flame temperatures nearer to the optimal temperature window for consumption of NO by NH_2, further reducing NO emissions with a reduced penalty in unburned NH_3, as found when targeting solely a reduction in HNO production. This resulted in unburned NH_3 emissions increasing by only 12 % at Φ = 1.1 – a reasonable trade-off for the NO reduction found. It is also suggested that lower post-flame zone temperatures from the additional heat loss case decomposed less unburned NH_3 into H_2, resulting in similar mass-based combustion efficiencies calculated for both cases.

5.1. Introduction

Hydrogen has been identified as a potential decarbonised replacement for fossil fuels in energy conversion technologies such as internal combustion engines, industrial burners, steam boilers, and gas turbines. However, storing hydrogen has proven problematic and costly, requiring pressurisation to 70 MPa or cryogenic cooling to 20 K [13]. Ammonia is gaining increased interest for this role as a low-cost hydrogen carrier which is significantly easier to store, liquefying at just 0.8-1.0 MPa pressure. It also has a long history of worldwide use as fertiliser, with existing storage and transportation infrastructure [31], unlike pure hydrogen.

However, effective combustion of pure ammonia presents some challenges, largely stemming from its low reactivity and narrow flame stability limits. These issues can be mitigated by blending ammonia with hydrogen or with methane [87,114,115,129–131]. However, as utilising methane in this role does not fully decarbonise the fuel blend, using hydrogen as the accelerant may be preferable. Additionally, three hydrogen atoms are contained within each ammonia molecule, which can be separated immediately prior to combustion via catalytic thermolysis at relatively low temperatures [116], potentially utilising waste heat from the combustion process. Therefore, the combustion improvement provided by hydrogen can be achieved without the disadvantage of having to store pure hydrogen on site.

The remaining challenge with the combustion of NH_3/H_2 or cracked NH_3 blends relates to emissions of NOx, N_2O and unburned NH_3 [130]. A resultant body of research on reducing these emissions has grown extensively in recent years. The emissions have been demonstrated to be highly dependent on equivalence ratio (Φ). Low NO and NO_2 emissions can be achieved at both

fuel lean and rich conditions, but lean conditions give rise to N_2O emissions [85], a greenhouse gas 273 times more potent than CO_2 over a 100-year period [132]. Negligible NOx emissions from NH_3/H_2 flames have been demonstrated at slightly rich conditions, but this results in emission of unburned NH_3 [81,130,133] which is also undesirable. Beyond varying equivalence ratio, other NOx reduction strategies such as pressurisation [91,92,133], fuel stratification [100,134] and humidification [135] have been investigated. Air staging, such as might be found in a rich-quench lean (RQL) systems, with a fuel rich primary stage and a fuel lean secondary stage, is therefore emerging as an attractive option for achieving low emissions from ammonia-based flames [136,137]. However, it is critically important for the primary fuel rich stage to be carefully controlled to minimise concentrations of unburned NH_3 entering the lean section, as this may lead to downstream NO production. Therefore, methodologies to achieve lower NO emissions at only slightly rich equivalence ratios in the primary stage are of value.

Few studies on effects of heat loss on ammonia-based flames have been conducted. Somarathne et al. [138] conducted 3D LES of non-premixed ammonia/air flames with NO PLIF for experimental validation. They found cooling by heat loss through the combustor walls reduced OH concentration in the region near the wall which ultimately reduced NO at the expense of increased emission of unburned NH_3. Okafor et al. [81] carried out further experimental studies on a similar staged combustor with premixed ammonia/air flames with different combustor linings which resulted in varying heat losses. They also found that higher heat loss resulted in lower NO emissions due to flame wall quenching, which caused increased unburned fuel, even at lean conditions. The authors also highlighted the elevated N_2O emissions stemming from lower temperatures inhibiting N_2O consumption. Contrary to other studies, this study also presented an increase in NO emissions with pressurisation if heat loss was elevated. They suggested that heat loss effects may be more influential than pressure effects, resulting in an increase in NO emissions. Zhang et al. [82] also investigated the effect of heat loss on emissions for premixed ammonia/air flames but simulated gas turbine film cooling by flowing air over the outside of the combustor walls. They also found a decrease in NO emission with increased heat loss stemming from a reduction of OH concentrations near the wall producing less NO via HNO and NH routes.

The present study seeks to further the emerging body of research into the effect of heat loss by experimentally assessing the impact on emissions from partially cracked ammonia, or NH_3/H_2 flames for the first time. Additionally, it uses a novel combustor with the ability to optimise temperatures to enhance the thermal de-NOxing reactions to increase consumption of NO, rather than solely to reduce its production. The first reaction driving this process is the chain branching reaction $NH_2 + NO \leftrightarrow NNH + OH$ which self sustains the process by producing OH to

oxidise NH_3 into NH_2 ready for fresh NO consumption and potentially limiting unburned NH_3 emissions. The other is the chain terminating reaction of NH_2 + NO ↔ N_2 + H_2O [61]. These reactions have been found to be most active in a 200 K range centred at 1220 K [25,26], which will be the target in the present study. This methodology/novel combustor design is also useful beyond reducing NOx. It additionally links lab-based research to practical combustion systems with significant heat loss operating on ammonia-based fuels by providing information on influences on emissions industrial systems may inherently cause. This could include changes in emissions when using ammonia as a fuel in steam boilers, in gas turbines with air film cooling of combustion chamber liners, or when integrating ammonia crackers or vaporisers into any combustion system.

5.2. Experimental and Numerical Methodologies

5.2.1. Swirl Burner

This study utilised an optically accessible premixed tangential swirl burner, with a geometric swirl number of 1.45, shown in Fig. 5.1. The fuel thermal power was maintained at 10 kW, and inlet temperature and pressure were atmospheric for all conditions. Shown in Table 5-1, a constant fuel blend of 20 $\%_{(vol.)}$ cracked ammonia was used, which comprises 0.667 NH_3 / 0.25 H_2 / 0.083 N_2 (mol.) as can be seen from Equations (5-1) and (5-2). This cracking ratio (α) was used as it maintains the required 3:$1_{(vol.)}$ ratio of H_2/N_2 from cracking while balancing emissions and flame stability. Equivalence ratios of 0.7 < Φ < 1.3 were assessed. Dry air and fuel were supplied using Bronkhorst thermal mass flow controllers (± 0.5 % between 15-95 % of maximum flow) and then premixed in a mixing plenum. This mixture then flowed via the swirler through an injection nozzle (d = 31.5 mm) using a central injection lance (d = 22.5 mm) as a bluff body. No central injection of fuel or air for stratification was used in the present study. The combustion chamber consisted of a quartz glass tube (d = 156 mm, L = 300 mm) to maintain optical access for chemiluminescence imaging and flame monitoring.

$$2NH_3 \rightarrow 3H_2 + N_2 \quad (5\text{-}1)$$

$$(1-\alpha)\, NH_3 + \alpha\,(1.5H_2 + 0.5N_2) \quad (5\text{-}2)$$

The temperature within the combustor was controlled by managing heat loss through the burner face. This was achieved by varying the flowrate of water through the burner face, designed with internal circulation channels for water flow and ridges on the face to increase surface area and hence heat transfer, shown on the right side of Fig. 5.1. A baseline condition of normal conditions

without any water flow was compared to an increased heat loss condition with a water flowrate of 16 g/s. The liquid water was supplied via a Bronkhorst Coriolis mass flow controller. Additional heat lost from the flame due to water flow through the burner face was calculated by Equation (5-3) below.

$$AQ = \dot{m}c\Delta T \quad (5\text{-}3)$$

Where AQ is the additional heat lost from the flame due to water flow, ṁ is the mass flowrate of water through the burner face, c is the specific heat capacity of water and ΔT is the temperature difference between water inlet and outlet temperatures.

Table 5-1: Operating conditions. Experiments conducted at 293 K and 0.1 MPa. 10 kW thermal power.

Cooling Water (g/s)	Fuel Blend ($_{vol.\%}$) $NH_3/H_2/N_2$	NH_3 (SLPM)	H_2 (SLPM)	N_2 (SLPM)	Air (SLPM)	Equivalence Ratio, Φ (-)
0, 16	66.7/25.0/8.3	34.8	13.0	4.33	222.8	0.70
					194.9	0.80
					173.3	0.90
					156.0	1.00
					141.8	1.10
					135.6	1.15
					130.0	1.20

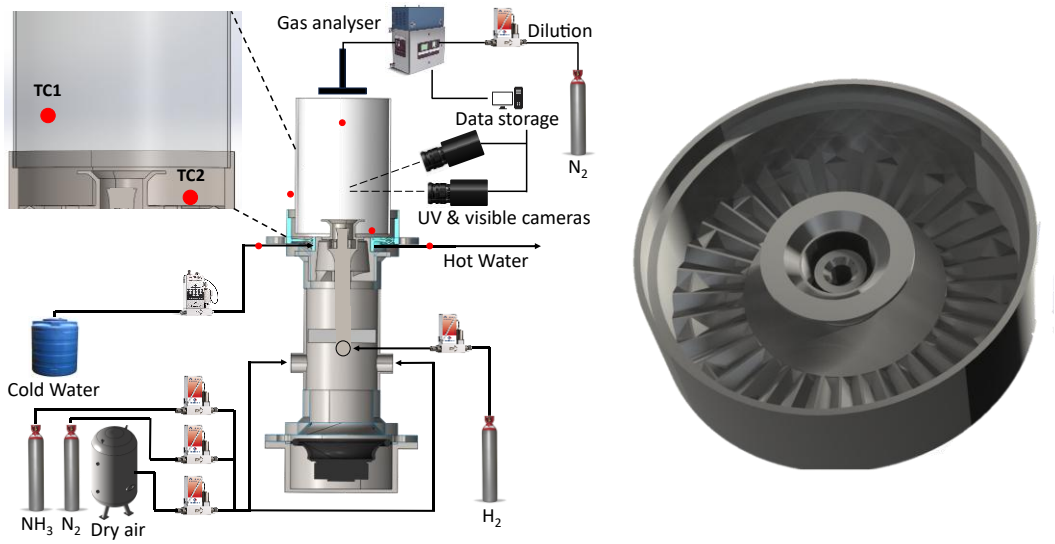

Fig. 5.1: Simplified drawing of experimental setup where red dots indicate position of thermocouples. TC1 and TC2 in the cut-away show positions of external recirculation zone (ERZ) and burner face thermocouples, respectively (left). Rendering of burner face (right).

5.2.2. Measurement of Exhaust Gas Emissions and Temperature

Exhaust gas samples were captured by a cross-shaped sample probe spanning the entire quartz confinement diameter 25 mm above its outlet and carried along heated lines to the gas analysers. Measured oxygen content was negligible at stoichiometric conditions, indicating no outside air was entrained into the probe. Two different emission measurement devices were used in parallel to target different gases. To simultaneously measure NO, NO_2, N_2O, NH_3, O_2 and H_2O, an Emerson CT5100 quantum cascade laser system was used at a sampling temperature of 463K and rate of 1 Hz (± 1% repeatability, 0.999 linearity). At each test point, 120 samples were averaged over a two-minute period after inlet flowrates, temperatures and emissions had stabilised. As H_2 is not detectable by infrared laser absorption, an Agilent 990 micro gas chromatographer was used for this gas instead. The maximum linearity error at any concentration along the full detectable range for each gas was as follows: NO = 0.208 %, NO_2 = 0.435 %, N_2O = 0.357 %, NH_3 = 1.257 %, O_2 = 0.382 %, H_2O = 0.011 % and H_2 = 0.120 %. Error bars in emissions plots were calculated using the uncertainty propagation method based on a combination of these linearity errors and measured standard deviation over the 120 samples. All samples were captured wet and normalised to dry, 15 % O_2 following equation 10 in [101]. As this study focuses solely on cracked ammonia as a fuel with relatively constant concentrations of H_2O in the exhaust, there was no need to use other emissions normalisation methodologies which account for high levels of water dilution arising from hydrogen-based fuels.

Fig. 5.1 shows the location of the K and R-type sheathed thermocouples used to determine temperatures within and outside the combustion chamber, as well as to estimate additional heat loss. These temperature readings were captured at 1 Hz, averaged over 120 seconds and corrected for radiative and convective heat losses. The correction methodology was based on the numerical heat transfer correction method from [139]. The empirical calculation based on Reynolds and Prandtl numbers proposed in [140] was used to calculate the convective heat transfer coefficient.

5.2.3. Chemiluminescence Measurements

Chemiluminescence images of the flame were captured simultaneously by LaVision cameras comprising Sony ICX285AL sensors and Hamamatsu HB105831 intensifiers. Edmund Optics bandpass filters all with 10nm FWHM centred at 310nm, 337nm and 632nm were used to capture OH* (309nm; A2Σ + -X2Π system), NH* (336nm; A3Π-X2Σ system) and NH_2* (630nm; single peak of NH_2 α band), respectively. The cameras had a sampling rate of 10 Hz and captured over a period of 20 seconds. After subtracting the background image and conducting a 3x3 pixel median filter, the images were averaged in Davis v10 and then went through an Abel Deconvolution script [141]. The resultant images were normalised to each species' group maximum to facilitate comparison of both spatial distribution and intensity variations between test points. Direct proportionality between ground state and excited radicals captured in chemiluminescence measurements was not assumed in this study. Instead, an assumption of only positive correlation was made. As suggested in [142] this is a reasonable assumption.

5.2.4. Chemical Reactor Network

A previously utilised [85] chemical reactor network (CRN) in CHEMKIN-PRO was used to analyse the most significant reactions influencing the formation of emissions. As shown in Fig. 5.2, four inlets for NH_3, H_2, N_2 and air fed into a series of perfectly stirred reactors (PSRs), simulating the premixing chamber, flame zone (FZ), external recirculation zone (ERZ) and central recirculation zone (CRZ). Finally, a 1D plug flow reactor (PFR) simulated the post flame zone. As the same swirl burner geometry was used in this study with similar fuel blends, equivalence ratios and thermal powers as in [85], the previously developed CRN was deemed an appropriate starting point. Due to the swirl burner similarities, the reactor recirculation splits previously determined via CFD (explained in [85]) were also regarded as an acceptable foundation. Absolute rate of production (ROP) values were used to evaluate the contribution of different reactions to production and

consumption of NO and N_2O in the flame zone. However, integrated ROP values were used for the post flame zone to account for it being one dimensional. ROP values were then normalised by each condition's total rate of production or consumption across the flame zone for NO, and across both flame zone and post-flame zone for N_2O. The aim here was not to compare absolute ROPs for each reaction, but instead to assess the differences in relative importance of each reaction across cases. Initial heat loss values were estimated from thermocouple measurements and residence times from empirical flow calculations based on combustor volumes and modified to give favourable agreement with sampled concentrations at each condition, as shown in the Supplementary Material (Fig. 5.14 and Fig. 5.15). It should be emphasised that moderate uncertainty is associated with CRN modelling, and the CRN presented here was primarily used for qualitative analysis of trends found in the experimental results, rather than detailed prediction of untested conditions. The chemical reaction mechanism from Stagni et al. [63] was utilised.

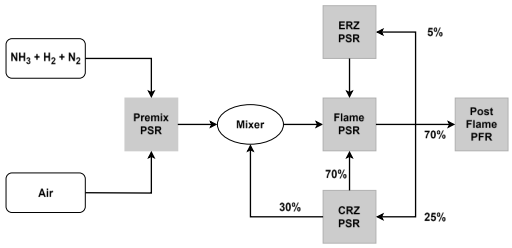

Fig. 5.2: Schematic of the chemical reactor network (CRN).

5.3. Results and Discussion

5.3.1. Temperatures

Fig. 5.3 compares the additional heat loss (AQ) from flowing 16 g/s of water through the burner face plate with the baseline case with no additional heat loss. This was calculated for each test point by considering the specific heat capacity of water, the mass flowrate of water through the face plate and the temperature difference measured by two thermocouples positioned immediately before and after the inlet and outlet of the burner face plate. The calculated AQ was relatively independent of equivalence ratio and was always roughly 600 W. Therefore, this condition will be referred to as "AQ = 600 W" throughout the remainder of the text and the baseline condition will be referred to as "AQ = 0 W". It is unsurprising that the additional heat loss was relatively constant owing to the face plate's proximity to the flame zone and external recirculation zone at all conditions. Heat loss may have been greater if the water flow was further downstream

on the combustor walls, but this would also have resulted in differences in flame length having a larger influence and hence increasing heat loss variations with equivalence ratio.

Fig. 5.4 shows temperature measured in the external recirculation zone (ERZ) and at the surface of the burner face plate. The largest temperature difference was found at the burner face, which was roughly 100 K cooler for the additional heat loss case, at all equivalence ratios. Smaller temperature differences were found in the ERZ of roughly 55 K at Φ = 0.7 and 30 K at Φ = 1.1.

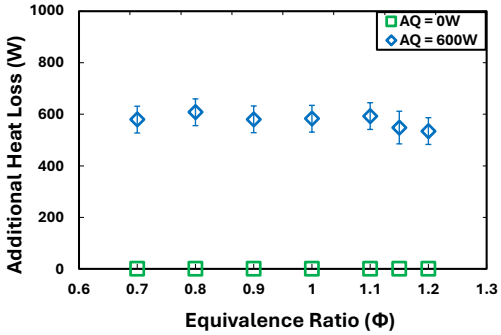

Fig. 5.3: Calculated additional heat loss from the flame with water flow through burner face plate.

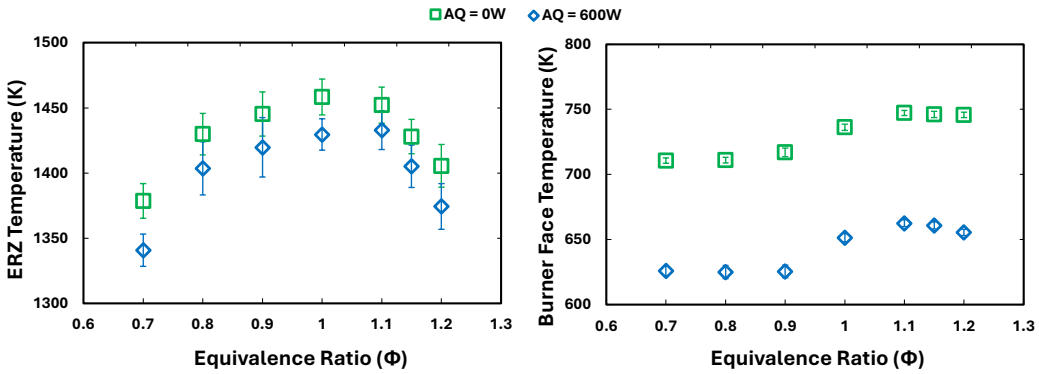

Fig. 5.4: Temperature in the ERZ (left) and at the burner face plate surface (right). ERZ readings corrected for radiative and convective heat losses from the thermocouple.

5.3.2. NOx and Unburned Fuel Emissions

Fig. 5.5 shows NOx and unburned fuel emissions for the baseline case and the reduced temperature case with 600 W of additional heat loss. NO and NO_2 emissions followed the expected non-monotonic trend with a single peak at Φ = 0.9 and Φ = 0.8, respectively for both cases. The AQ=600 W case showed a general 10-20 % reduction in NO compared to the baseline AQ=0 W case and both cases reached negligible NO and NO_2 emissions at slightly rich conditions. The penalty for low NO emissions at rich conditions is an increase in emissions of unburned fuel from a lack of oxygen. Fig. 5.5 shows both unburned NH_3 and H_2 were negligible at lean conditions but rapidly increased at slightly rich equivalence ratios. Additionally, the lower

temperatures associated with the AQ=600 W case increased emissions of unburned NH_3, most visible at Φ = 1.15. However, the AQ=600 W case had lower emissions of unburned H_2 than the baseline case, theorised to be due to the lower temperature in post flame zone thermally decomposing less of the unburned NH_3 into H_2 and N_2.

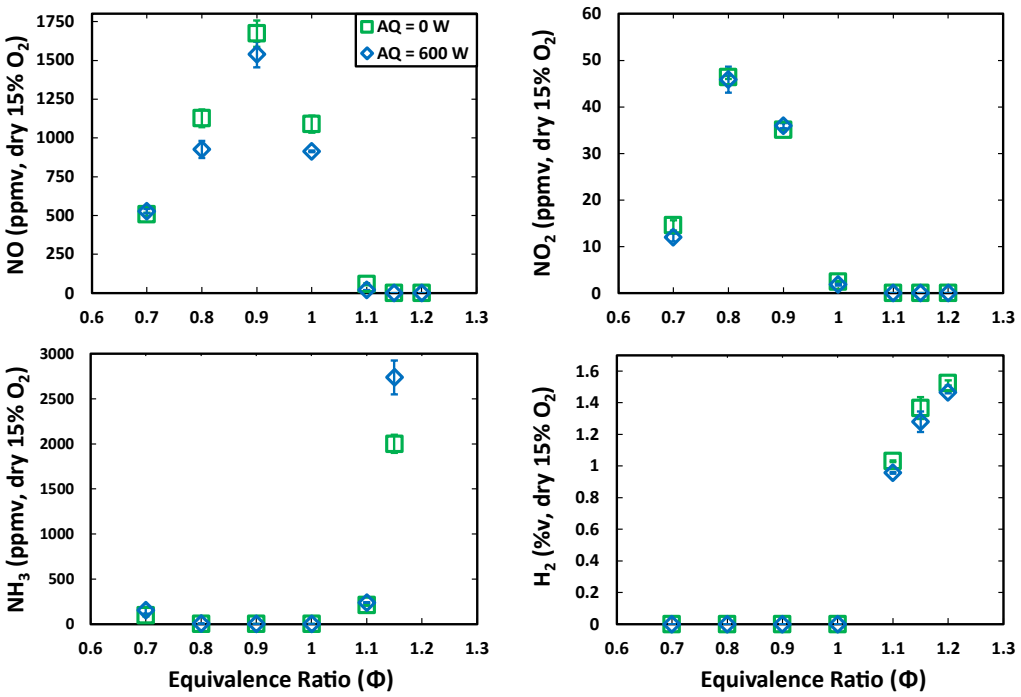

Fig. 5.5: Sampled emissions with changing equivalence ratio for the baseline case (green squares) and with additional heat loss (blue diamonds). NO (top left), NO_2 (top right), unburned NH_3 (bottom left) and unburned H_2 (bottom right).

Fig. 5.6 shows the normalised ROP at Φ = 0.8 for both conditions. It reveals that the ~18 % lower NO found for the AQ = 600 W case compared to the AQ = 0 W case is a result of both lower NO production and higher NO consumption. For both cases, NO production is dominated by the HNO route, an example reaction of which is shown in Equation (*5-4*). This reaction has previously been shown to be dependent on the reaction shown in Equation (*5-5*) [85]. Fig. 5.6 clearly shows a reduced significance of production via the HNO routes for the AQ = 600 W case of 6.4 %, which is likely related to lower temperatures from additional heat loss. Consumption of NO by NH_2 was of 9.3 % higher significance for the AQ = 600 W case, in agreement with the methodology of reducing temperatures – shown in Fig. 5.4 – nearer to the peak reactivity of the NH_2 de-NOx reactions discussed in Section 5.1. Furthermore, consumption of NO by NH to form N_2O is also higher for the AQ = 600 W case, which would suggest higher N_2O emissions.

$$HNO \leftrightarrow NO + H \quad (5\text{-}4)$$

$$NH + OH \leftrightarrow HNO + H \quad (5\text{-}5)$$

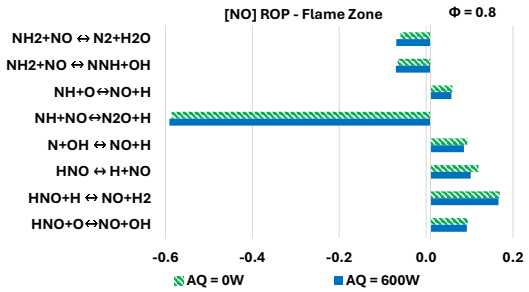

Fig. 5.6: Calculated NO ROP at Φ = 0.8 in the flame zone, normalised to the total rate of production and consumption. Baseline case (green, dashed) and with additional heat loss (blue, solid).

The remainder of this section will focus on slightly rich conditions, where the largest percentage NO emission reduction was found. Fig. 5.7 shows the emissions of NO, NH_3, H_2, and the total fuel mass consumption rate (columns) for both cases at slightly rich conditions. The total fuel mass consumption rate was calculated following Equation (5-6), after converting the sampled volumetric emissions to a mass basis.

$$\eta = 1 - \frac{\dot{m}(NH_3 + H_2)_{out}}{\dot{m}(NH_3 + H_2)_{in}} \tag{5-6}$$

Fig. 5.7 shows a 67 % reduction in NO emissions for the AQ=600 W case compared to the base case of AQ=0 W. NH_3 emissions were increased by only 12 %, which represents a favourable trade-off. Despite a 7 % reduction in emissions of unburned H_2 for the AQ=600 W case, the total fuel mass consumption rate was similar for both cases as H_2's high volumetric emission was offset by its low density. At Φ = 1.15, both cases reached negligible NO emissions. However, the significant increase in unburned NH_3 emissions from the AQ=600 W case at Φ = 1.15 did have a noticeable impact on total mass fuel consumption rate, reducing from 95.5 % for the AQ = 0 W case to 94.8 % for the AQ = 600 W case. This shows that the reduction in H_2 emissions cannot offset the increase in NH_3 emissions if the equivalence ratio is above a certain threshold and focus should remain on only slightly rich conditions with relatively low NO and manageable unburned fuel emissions. Therefore, to understand the chemical reactions responsible for NO reduction at Φ = 1.1, the CRN explained in Section 5.2.4 was deployed.

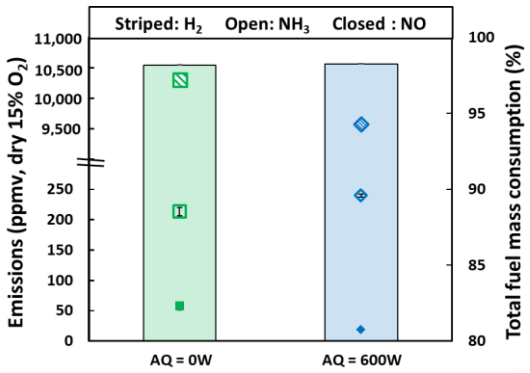

Fig. 5.7: Sampled emissions of H_2 (striped symbols), NH_3 (open symbols), NO (closed symbols), and total fuel mass consumption rate (columns) at Φ = 1.1 for both cases. Left-hand Y axis split, with the lower section showing NH_3 and NO values and the top section

Fig. 5.8 shows that at Φ = 1.1, the main difference in NO production between the two cases was from the reaction shown in Equation (*5-4*). These HNO pathways were 2.3 % less significant for the AQ = 600 W case. Furthermore, for the AQ = 600 W case, Fig. 5.9 shows a reduction in OH* and NH* intensity, as well as volume – with the narrowing of the high intensity region evident for both species. This was to be expected due to chemiluminescence intensity's dependence on temperature. Lower OH concentrations available for oxidation of NH_3 also results in increased unburned emissions of NH_3. Consequently, NO reduction strategies focusing solely on reducing HNO production are unlikely to be practical as they will always increase emissions of NH_3, which is likely to convert into NO if combusted with excess air in a rich-quench-lean (RQL) type combustor.

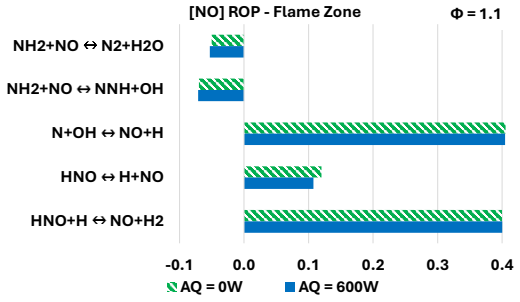

Fig. 5.8: Calculated NO ROP at Φ = 1.1 in the flame zone, normalised to the total rate of production and consumption. Baseline case (green, dashed) and with additional heat loss (blue, solid).

Therefore, the more interesting point is related to NO consumption. Fig. 5.8 shows that consumption of NO by NH_2 was 3.4 % more significant for the additional heat loss case of AQ = 600 W. This increase in NO consumption by NH_2 is posited to be due the additional heat loss shifting flame temperatures lower and nearer to the region of high NH_2 + NO reactivity discussed in Section 5.1. Despite an expected reduction in NH_2* chemiluminescence intensity from these lower temperatures, not much difference in intensity can be seen across the two cases in Fig. 5.9. This is clearer to see in Fig. 5.10, which compares the maximum intensity captured by the

chemiluminescence camera with an NH_2* filter for both cases against equivalence ratio. It shows that for rich conditions – and particularly for Φ = 1.1 – little difference in NH_2* intensity was found, despite lower temperatures reducing NH_2* intensity for the AQ = 600 W case. This suggests the AQ = 600 W case had higher ground state concentrations of NH_2 at Φ = 1.1 which were able to increase NH_2* intensity, compensating for the effect of temperature on this diagnostic technique. The results from the CRN support this as the ERZ outlet for the AQ = 600 W case had a higher mass flowrate of NH_2 at 4.08E-07 g/s, compared to the base case which had 3.48E-07 g/s. As the ERZ outlet goes to the flame zone, this increase in ground state NH_2 concentration would then have resulted in an increase in NO consumption, ultimately reducing measured NO emissions. Focusing on increases to the reactivity of NH_2 consumption of NO is especially worthwhile due to the chain branching reaction of NH_2 + NO ↔ NNH + OH, which produces fresh OH ready to consume NH_3, potentially inhibiting the increase in unburned NH_3 emissions.

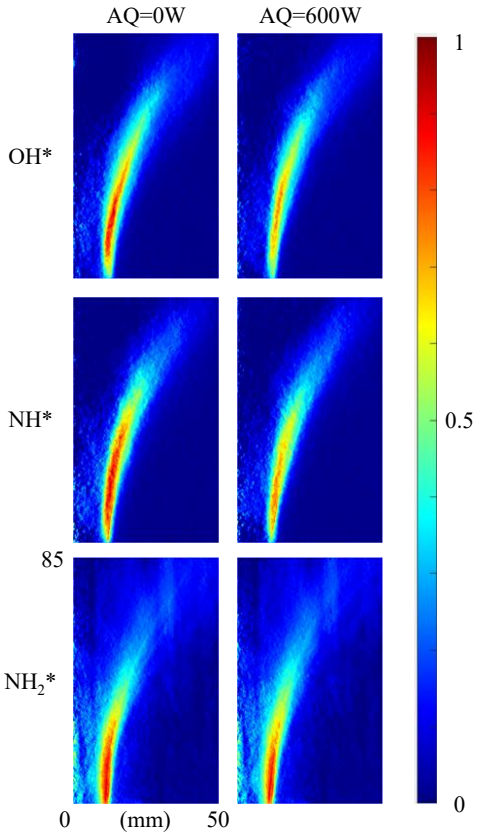

Fig. 5.9: Abel transformed chemiluminescence (OH, NH* and NH_2*) for the baseline case of AQ = 0 W (left column) and the additional heat loss case of AQ = 600 W (right column) at Φ = 1.1. Colourmap of images normalised to each species' maximum intensity across both cases at Φ = 1.1.*

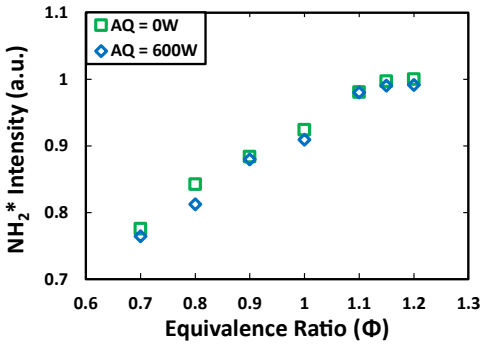

Fig. 5.10: Relative intensity of NH_2 from the averaged chemiluminescence images for both cases. Normalised to maximum NH_2* captured across both cases for all equivalence ratios.*

5.3.3. N_2O Emissions

As discussed in Section 5.1, care must be taken to avoid emissions of N_2O during ammonia combustion. Therefore, this section investigates the effect of additional heat loss on N_2O emissions. Fig. 5.11 shows N_2O emissions captured for the baseline case and the reduced temperature case with 600 W of additional heat loss. Negligible N_2O emissions were recorded for both cases at $\Phi > 0.9$ and rapidly increasing emissions were recorded as equivalence ratio was reduced. As reported in [81], additional heat loss was found here to increase N_2O emissions, with an 18% increase at $\Phi = 0.7$.

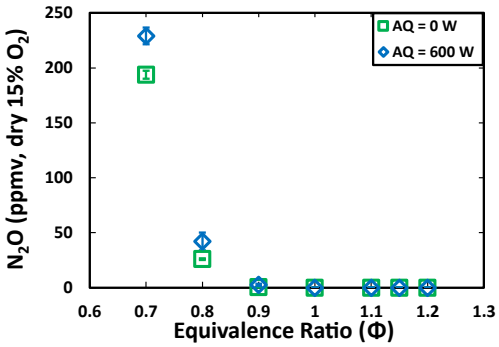

Fig. 5.11: Sampled N_2O emissions with changing equivalence ratio for the baseline case (green squares) and with additional heat loss (blue diamonds).

To aid in the understanding of the chemical reactions responsible for the increase in N_2O emissions for the additional heat loss case at lean conditions, the rate of production and consumption of different reactions was examined by utilising the CRN described in Section 5.2.4. Fig. 5.12 shows the ROP analysis at $\Phi = 0.7$ for both cases, normalised as described in Section 5.2.4. It shows that nearly all N_2O production was in the flame zone and the majority of N_2O consumption was also in the flame zone, although with a significant amount in the post-flame zone. The relatively small differences in rate of production/consumption of N_2O was expected as

the difference in experimental N_2O measured at Φ = 0.7 was only ~35 ppm between the two cases. The reactions shown in Equations (*5-7*) and (*5-8*) were the most significant for the consumption of N_2O for both cases.

$$N_2O + (M) \leftrightarrow N_2 + O + (M) \quad (5\text{-}7)$$

$$N_2O + H \leftrightarrow N_2 + OH \quad (5\text{-}8)$$

Fig. 5.12 shows little difference between the two cases in the rate of flame zone N_2O consumption by the third-body reaction shown in Equation (*5-4*). However, the base case of AQ = 0 W had 1.7 % higher significance of flame zone consumption of N_2O by free H atoms from the reaction shown in Equation (5-8). This can be explained by the temperature dependence of the free H atom previously reported in [85]. Lower temperatures found with additional heat loss (shown in Fig. 5.4) would decrease H atom availability to consume N_2O, resulting in an increase in N_2O emissions. The increase in post-flame zone consumption of N_2O by the third-body reaction shown in Equation (*5-7*) was not enough to offset the reduced consumption in the flame zone. This increase in N_2O consumption by Equation (*5-7*) can be explained by the residence time dependence of the reaction. The lower temperature flame in the AQ = 600 W case would have slightly reduced burning velocity, potentially increasing flame length.

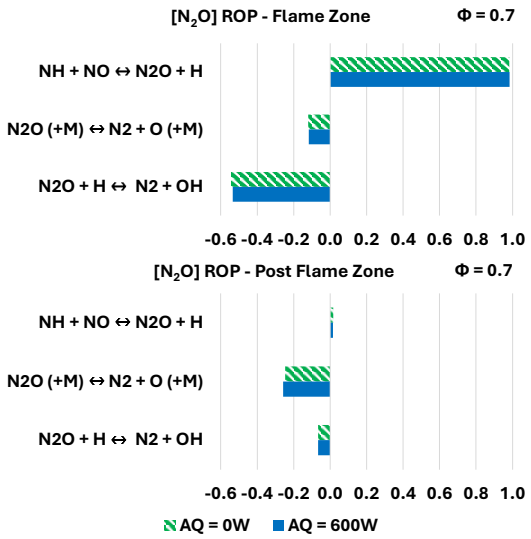

Fig. 5.12: Calculated N_2O ROP at Φ = 0.7 in the flame zone (top) and post-flame zone (bottom) normalised to total rate of production and consumption across both. Baseline case (green, dashed) and with additional heat loss (blue, solid).

This marginal difference can be confirmed by examination of the high-intensity regions of the NH_2* images shown in Fig. 5.13 below, with some high-intensity NH_2* present above the black dotted line for the AQ = 600 W case. This longer flame may have resulted in a longer residence time, increasing N_2O consumption by the third-body reaction. The generally lower temperatures

in the post-flame zone compared to the flame zone for both cases reduced the significance of the reaction shown in Equation (5-8) here.

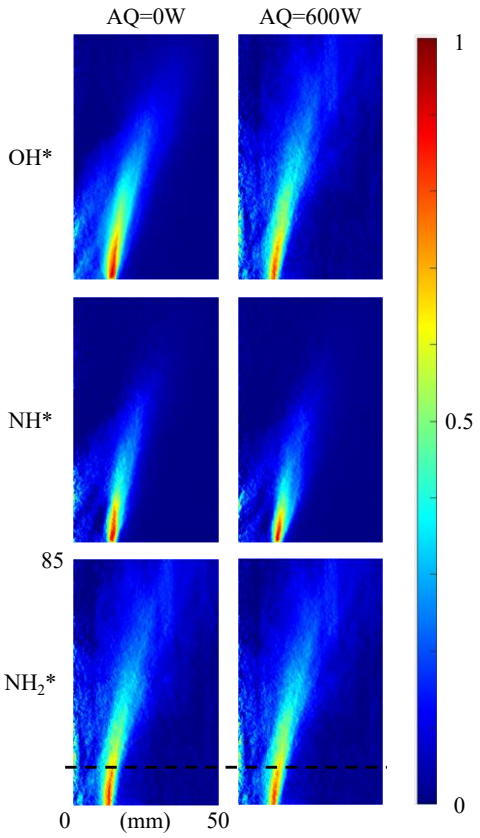

Fig. 5.13: Abel transformed chemiluminescence (OH, NH* NH_2*) for the baseline case of AQ = 0 W (left column) and the additional heat loss case of AQ = 600 W (right column) at Φ = 0.7. Colourmap of images normalised to each species' maximum intensity across both cases at Φ = 0.7.*

5.4. Conclusions

The control of emissions from a 20 $\%_{(vol.)}$ cracked ammonia flame was experimentally and numerically investigated by managing heat loss from the flame utilising a novel swirl burner design. Emissions of NO, NO_2, N_2O and unburned NH_3 and H_2 were found to be sensitive to the temperature differences associated with increased heat loss.

N_2O emissions at lean equivalence ratios were slightly increased due to lower flame temperatures from increased heat loss limiting the availability of free H atoms to consume N_2O. This highlights the challenges with combustion of ammonia-based fuels with excess air and steers focus towards achieving low NO emissions with slightly rich conditions instead.

NO emissions at Φ = 1.1 were 67 % lower for the case with additional heat loss. This was partly due to a 2.3 % reduction in significance of the HNO production and partly due to a 3.4 % increase

in significance of NO consumption by NH_2 by using additional heat loss to shift flame temperature nearer to the peak of NH_2 consumption reactivity around 1200K.

NH_3 emissions at Φ = 1.1 were 12 % higher for the case with additional heat loss, representing a favourable trade-off with the reduction in NO emissions. It is suggested that unburned NH_3 emissions would have been higher if not for the mitigation from the chain branching reaction of $NH_2 + NO \leftrightarrow NNH + OH$ providing OH to consume NH_3. Despite the increase in unburned NH_3 emissions, total fuel mass consumption rate at Φ = 1.1 was similar across both cases as the lower post-flame zone temperatures likely resulted in less unburned NH_3 being thermally cracked into H_2.

5.5. Supplementary Material

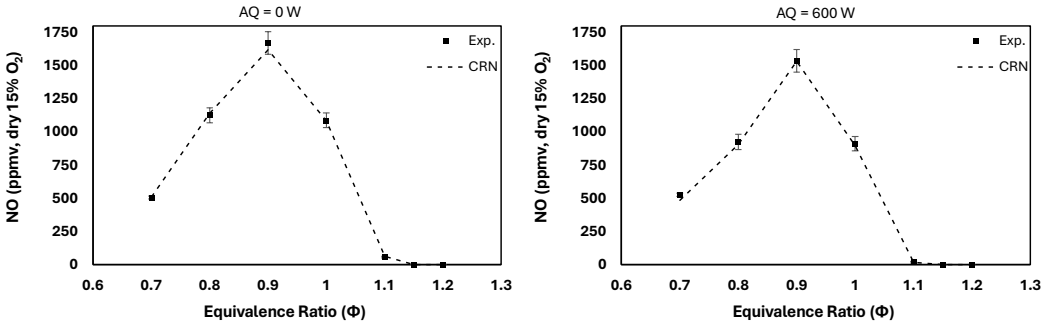

Fig. 5.14: Comparison between experimental results (symbols) and CRN predictions (lines) of NO for the AQ = 0 W case (left) and AQ = 600 W case (right)

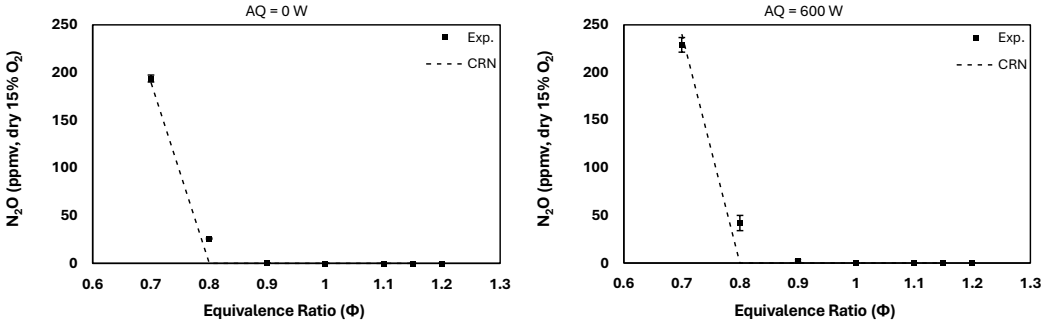

Fig. 5.15: Comparison between experimental results (symbols) and CRN predictions (lines) of N_2O for the AQ = 0 W case (left) and AQ = 600 W case (right).

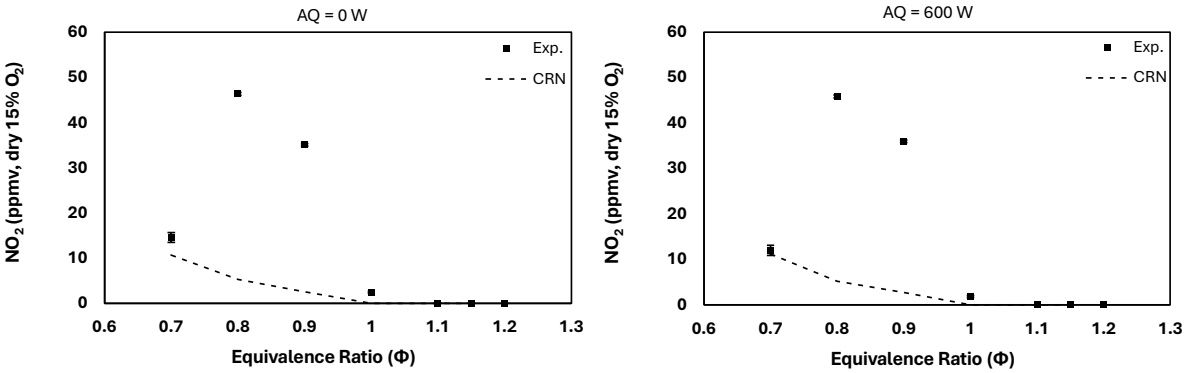

Fig. 5.16: Comparison between experimental results (symbols) and CRN predictions (lines) of NO_2 for the AQ = 0 W case (left) and AQ = 600 W case (right).

6. Swirl Number and Nozzle Design for Scale-up

This chapter comprises the journal paper titled “Experimental analysis of swirl number and nozzle design for scale-up of partially cracked ammonia flames.” published in Applications in Energy and Combustion Science. Further information is presented in the Statement of Authorship of Publications.

Its novelty lies in being the first study to focus on the investigation of optimal swirl number and nozzle design for scaling up NH_3 based flames. It remains that few published studies explore the impact of varying swirl number on flame stability and emissions. Of particular importance is that this work is the first to examine how nozzle design affects flame stability with increasing thermal power and outlines desirable characteristics for avoiding blowoff as gas inlet velocity increases.

This chapter advances the aim of this thesis by addressing the overall theme of advancing the development of industrial swirl burners utilising partially cracked ammonia. Specifically, it partially addresses objectives 2 and fully addresses objective 5. It is linked directly to Chapters 3, 4 and 5 as it includes the same swirler and nozzle design presented in those chapters as a baseline for comparison with new ones. It also examines emissions from partially cracked ammonia flames as they do.

Abstract

Due to its ease of storage and existing global distribution network, interest in the use of renewably produced ammonia for decarbonising energy systems is growing. Partially cracking ammonia can overcome the flame stability challenges of this fuel, but demonstrations of high-power ammonia-based swirl flames with acceptable emissions have yet to be realised. Therefore, the present study examines the effects of varying swirl number and nozzle design on the static stability and emissions from 20 % (vol.) cracked ammonia swirl flames for a wide range of equivalence ratios ($0.3 < \Phi < 2.2$) and thermal powers of 5, 10 and 15 kW. Additionally, a reference case of 100 kW thermal power at stoichiometric conditions was tested. Stable flames were shown across a broad range of equivalence ratios, swirl numbers and nozzle geometries although flame morphologies varied greatly. Of note was a geometric swirl number of 1.75 paired with a long nozzle, which enabled the transition to a flat, Coanda jet flow flame at equivalence ratios of 0.6 and 0.7. For a geometric swirl number of 1.45, shortening the nozzle resulted in significantly shorter, wider V-shape flames with greatly improved rich blowoff limits. This was found to be a

desirable characteristic for reaching high thermal power with a constant nozzle throat diameter – i.e. dump plane velocity – as a widened flame brush prevents jet-like flames, which are susceptible to pinching off. This can also be achieved by increasing the swirl number, although to a lesser extent. However, with a widened flame brush, careful consideration must be given to confinement diameter to avoid flame impingement which has potential to increase local heat loss and hence reduce combustion efficiency, resulting in an increase in unburned NH_3 emissions. With the same geometric swirl number of 1.45, the shorter nozzle configuration resulted in higher NO emissions, potentially due to the shorter nozzle forming shorter, wider flames, meaning there was less residence time for NH_2 to consume NO in the flame zone. This difference was less noticeable at rich conditions, with all configurations reaching negligible NO emissions by $\Phi = 1.15$.

6.1. Introduction

Interest in the use of partially cracked ammonia for the decarbonisation of energy is growing. This is due to ammonia's ease of transportation and existing global infrastructure [31,112,115]. The main challenges relating to combustion of pure ammonia – low flame stability and emissions of NOx – can be addressed by mixing ammonia with a relatively small amount of hydrogen [52,143]. This can be achieved by partially cracking the ammonia with integrated thermo-catalytic systems [144], resulting in a final fuel blend of ammonia, hydrogen and nitrogen.

The earliest studies on ammonia combustion in gas turbine swirl burners were published in the 1960s [44], with main findings including narrow stability limits and the requirement of air velocity being half of what they were for hydrocarbon fuels. Few publications can be found between then and the mid-2010s.

However, swirl stabilised combustion of ammonia/hydrogen-based blends has seen renewed research in the last decade, mainly examining emissions or flame stability with fixed swirl numbers. Many research groups have presented effective flame stabilisation with this method at relatively low thermal power, in the order of tens of kW. In 2015, Cardiff University tested blends of NH_3/CH_4 as high as 80/20 (vol.%) and NH_3/H_2 of 50/50 (vol.%) in a generic tangential swirl burner designed for natural gas with a swirl number of 1.05 [145]. For the NH_3/H_2 case of 33kW thermal power, narrow stability limits between equivalence ratios (Φ) of just 0.425 and 0.577 were possible, with flashback preventing any further increases in Φ. This suggested that generic swirlers from natural gas combustors may not necessarily be suited to NH_3/H_2 blends.

In 2017, Kurata et al. demonstrated power generation from a converted kerosene MGT operating on pure NH_3 [46]. The MGT featured a non-premixed axial swirl burner with swirl number of 0.88. Good flame stability was found, but it was noted that elevated inlet temperatures would widen stability limits. Later, using a similar combustor, Okafor et al. found that compared to atmospheric conditions, increasing the pressure to 0.2 MPa reduced NO emissions without any apparent penalty in flame stability nor unburned NH_3 emissions [47].

An early study from Tohoku University compared two different axial swirlers with swirl numbers of 0.736 and 1.270 in the combustion of pure NH_3 at a thermal power of 13.2kW [48]. Although narrower than those of CH_4, the stability limits of NH_3 were found to be broad, roughly $0.65 < \Phi < 1.3$ for an inlet velocity between 2 and 8 m/s for the high swirl case, and slightly wider for the low swirl case. The authors suggested the lower swirl number presented wider stability limits due to a higher characteristic length of recirculation aiding the slow combustion rate. This study also presented slightly rich conditions of $\Phi = 1.05$ as optimal, with relatively low emissions of both NO and NH_3.

In 2019, a marked increase in research of NH_3 combustion in swirl burners can be seen. Continued studies from Cardiff University found a 70/30 NH_3/H_2 blend (vol.%) provided stable flame at slightly rich conditions using a tangential swirl number of 0.8 at a thermal power of 39.3 kW [146]. The same swirl burner and fuel blend was also found to provide stable combustion at elevated conditions of up to 0.184 MPa and with humidification and secondary air injection [78]. It was noted that the limiting factor in increasing pressure further was fuel supply of gaseous ammonia, not flame stability.

Initial studies at KAUST on NH_3/H_2 blends using a swirl burner with swirl number of 1.0 and thermal power of <10kW [87] found narrow stability limits bounded by lean blowoff and flashback when the ammonia fuel fraction was less than 60 % (vol.). Above this, stability limits widened significantly and the 70/30 (vol.%) NH_3/H_2 was bounded by lean blowoff at $\Phi = 0.3$, but instead of the upper boundary being flashback, it was found to be rich blowoff, at $\Phi = 1.4$. Increasing NH_3 fraction further resulted in a slight narrowing of stability limits – although still significantly wider than below 60% NH_3, with upper limits still bounded by rich blowoff rather than flashback. Following research with the same swirl burner increased thermal power to 32.5 kW and pressure to 5 bar [91]. Here, it was found that pressurisation increases stability limits of pure NH_3 flames. For NH_3/H_2 blends, both lean blowout and flashback limits were slightly reduced with pressure. Additionally, the NH_3 fuel fraction threshold at which the upper limit of stability transitioned from flashback to rich blowoff was increased. Another study from Wang et al. of KAUST utilising an

adjustable axial swirl burner examined the effects of varying swirl number between 0.6 and 1.0 on emissions from NH_3/CH_4 flames [147]. Stable flames were found for both swirlers in the range $0.55 < \Phi < 0.95$. Additionally, this study showed a significant difference in both flame structure and NO emissions, with the higher swirl flame presenting lower NO emissions above $\Phi = 0.75$. This was suggested to be due to the higher swirl flame having higher heat loss to the nozzle, inhibiting the formation of OH radicals in this region.

A recent study from Chen et al. of USTC [148] examined OH* chemiluminescence from a range of ammonia blended flames with a swirl number of 0.778. They found that partially cracked ammonia flames were narrower and longer than equivalent NH_3/H_2 flames and had a higher peak value of OH*, indicating the stretching effect was stronger. This has potential to affect blowoff limits in partially cracked ammonia flames, warranting further study compared to classical NH_3/H_2 blends.

It is clear to see that most research groups have been operating NH_3 based flames with relatively low swirl numbers between 0.6 and 1.05. Despite this rich literature of ammonia swirl flames, it remains that few studies have drawn comparisons between swirl number and flame performance, either in terms of emissions or stability limits, particularly for NH_3/H_2 flames. Therefore, the present study seeks to further the deployment of swirl burners operating on partially cracked ammonia blends in an industrial setting by investigating how swirl number and nozzle design affects flame stability and emissions. A particular focus is given to how these swirlers perform with an increase in thermal power towards industrially applicable levels.

6.2. Experimental Methodology

6.2.1. Swirl Burner

In this study, the optically accessible premixed atmospheric swirl burner shown in Fig. 6.1 was used. Air and fuel entered a premixing chamber via Bronkhorst thermal mass flow controllers with accuracy of ± 0.5 % of reading between 15 % and 95 % of full scale. A constant fuel blend representing 20 % cracked ammonia (66.7/25/8.3 (vol. %) $NH_3/H_2/N_2$) for equivalence ratios $0.3 < \Phi < 2.2$ and three net thermal powers; 5, 10 and 15 kW was used. Additionally, a reference case was preliminarily examined where the same swirl burner was placed inside a significantly larger confinement representative of a 1 MW steam boiler. Here, the net thermal power was increased to 100 kW and stoichiometric conditions were examined for the same 20 % cracked NH_3 fuel blend. 20 % cracked ammonia includes the nitrogen produced during the cracking process in the

required 3:1 hydrogen/nitrogen ratio while maintaining the NH_3/H_2 ratio near to 70/30 (vol. %). This fuel blend was used due to it having previously been identified as an optimal NH_3/H_2 ratio [78], balancing improved flame stability from hydrogen addition [52] with penalties in exhaust gas emission [56]. While this fuel blend generally has a lower laminar burning velocity than pure methane flames, the differences are smaller at lean and rich conditions [110]. Additionally, 20% cracked ammonia flames have been found to have the highest ratio of turbulent flame speed to laminar flame speed of partially cracked blends [149], indicating they may have higher blowoff resistance than suggested solely by their laminar flame speed. Furthermore, an 18% cracked ammonia flame (very similar to the fuel blend in this study) has been shown to have higher lean blowoff resistance than pure methane flames due to higher positive flame curvatures and lower strain rates resulting from a Lewis number below unity [150,151].

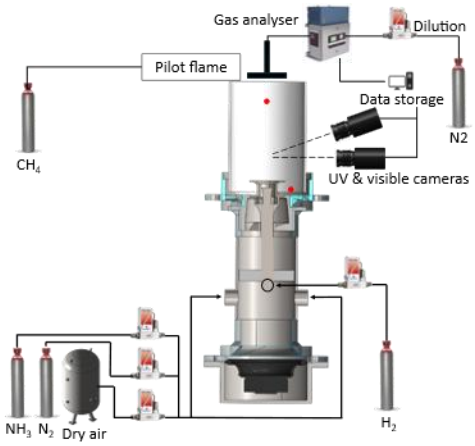

Fig. 6.1: Simplified schematic of experimental setup.

A range of tangential swirlers and nozzles were investigated, described in Table 6-1. The geometric swirl number was defined as shown in Equation (6-1), reproduced from [39].

$$Sg = \frac{\pi R R_{eff}}{A_t} \qquad (6\text{-}1)$$

Where R was the exit radius, R_{eff} was the radial distance between each tangential channel axis and the injector axis, and A_t was the cross-sectional area of the tangential channels. The different geometric swirl numbers were achieved by varying A_t.

As shown in Fig. 6.2, the nozzle inner diameter (D) and bluff body outer diameter (0.7 D) were constant for all cases. The confinement consisted of a quartz tube of inner diameter 5 D and length 9.5 D, resulting in an expansion ratio from the dump plane area to confinement area of 50.1. The nozzle geometry was varied by changing the axial length of the nozzle. In Fig. 6.2, the dashed red line shows the approximate position of the original dump plane with a long nozzle, and the black solid line shows the modified dump plane position with a shorter nozzle. The long

nozzle had a greater distance from the dump plane to nozzle expansion section than the short nozzle, but the dump plane cross-sectional area was kept constant for all conditions and cases.

Table 6-1: Description of swirl number and nozzle geometries

S_g	*Nozzle*	*Thermal Power (kW)*	*Φ Tested*
1.0	Short	5, 10, 15	0.3 < Φ < 2.2
1.45	Short	5, 10, 15, 100	0.3 < Φ < 2.2
1.45	Long	5, 10, 15, 100	0.3 < Φ < 2.2
1.75	Long	5, 10, 15	0.3 < Φ < 2.2

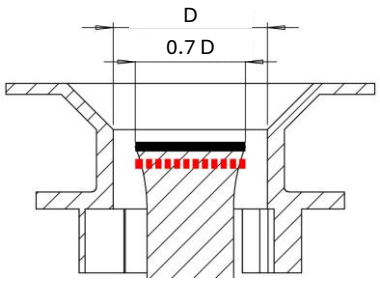

Fig. 6.2: Diagram of swirler and nozzle (black and red dashed lines show position of dump plane relative to nozzle walls with a short and long nozzle, respectively).

6.2.2. Flame Imaging

A Nikon Z7ii mirrorless digital camera was used to capture direct line of sight images of the flame from a distance of approximately 500mm. Unless otherwise stated, the camera's aperture was maintained at F/4 with an exposure time of 1/3s and an ISO of 64 for all photographs to enable comparisons of flame morphology and intensity.

Chemiluminescence images were captured by LaVision cameras comprising Sony ICX285AL sensors and Hamamatsu HB1058 intensifiers. Edmund optics bandpass filters all with 10nm FWHM centred at 310nm, 337nm and 632nm were used to capture OH* (309nm; A2Σ + -X2Π system), NH* (336nm; A3Π-X2Σ system) and NH_2* (630nm; single peak of NH_2 α band), respectively. These cameras were triggered simultaneously for a period of 20s at a sampling rate of 10Hz. Following the subtraction of the background images and a 3x3 median pixel filter, the images were averaged and processed with an Abel Deconvolution script [141]. Abel transformed images were either normalised to their own maximum to compare flame morphology or to group maximums to compare radical intensities across different swirlers and nozzle setups.

6.2.3. Exhaust Gas Measurements

Exhaust gas samples were captured via a cross-shaped sampling probe spanning the full diameter of the quartz tube confinement outlet. To prevent condensation, the sample gas was carried along a heated line to an Emerson CT5100 quantum cascade laser gas analyser. Measurements of NO, NO_2, N_2O, NH_3, O_2 and H_2O were made at a temperature of 463 K and rate of 1 Hz (±1% repeatability, 0.999 linearity). At each test condition and following the stabilisation of inlet flowrates, temperatures and emissions, 120 samples were recorded over a period of two minutes. When raw readings were above the analyser's upper detection limit (~2200 ppm for NO and ~1300 ppm for NH_3), N_2 was used to dilute the sample back into range ((±10% repeatability). Samples were captured wet and normalised to dry, 15% O_2 following equation 10 in [101]. As this study focuses solely on a single blend of partially cracked ammonia with relatively constant concentrations of H_2O present in the exhaust gas, there was no need to use other emissions normalisation methodologies which account for high levels of H_2O dilution arising from hydrogen-based fuels in comparison to hydrocarbon fuels.

6.3. Results and Discussion

6.3.1. Flame Morphology and Stability

Fig. 6.3 shows direct line of sight photographs captured for each of the four swirlers for a range of equivalence ratios at a constant net thermal power of 10 kW. In general, flame length increased with equivalence ratio at rich conditions regardless of swirl number. For $0.7 < \Phi < 1.0$, flame length was relatively consistent for all cases, apart from for the Sg = 1.75 long nozzle case which presented as a nearly flat flame at the leanest equivalence ratios. Flame luminosity – largely from NH_2* – increased with equivalence ratio and was particularly low at Φ = 0.6 for all swirlers, suggesting reduced combustion efficiency here.

With a constant swirl number of S_g = 1.45, the length of the nozzles can be seen to have a significant impact on flame morphology. The S_g = 1.45 long nozzle case presented a markedly longer flame than the S_g = 1.45 short nozzle case with a higher flame base angle at all equivalence ratios. It is suggested that a longer nozzle downstream of the bluff body acts as a guide channel, restricting the flow from expanding and thus hindering the formation of the external recirculation zone (ERZ) until further downstream. Similarly, this guide channel preventing the flow from expanding radially could result in the flow returning to the central axis shortly downstream of the bluff body, resulting in the central recirculation zone (CRZ) being compressed axially. The long

nozzle case then may not properly expand radially until reaching a vortex breakdown bubble further downstream. Alternatively, the short nozzle case had less of a radial obstruction downstream of the bluff body, enabling the flow to open radially earlier, forming a stronger ERZ and CRZ. At rich equivalence ratios, this effect was even clearer, with the long nozzle flame transitioning into a near jet-like flame shape with a potential reduction of the central recirculation zone (CRZ) strength.

Comparing the two short nozzle cases, increasing swirl number also reduced flame length and flame base angle, suggesting that nozzle geometry can be equally as important as swirl number in determining flame morphology. In comparing the two long nozzle cases, the same findings of increasing swirl number were present and more noticeable. This could suggest that the nozzle design may be the dominant design factor influencing flame morphology. The S_g = 1.75 long nozzle case did not present the same flame transition to near jet-like behaviour at rich conditions as the S_g = 1.45 long nozzle case. Additionally, there was a transition at lean conditions. At $\Phi \leq 0.7$, the S_g = 1.75 long nozzle case presented an almost flat flame with an exceptionally short flame length and near zero flame base angle. At higher equivalence ratios, a more conventional V-shaped swirl flame was found. This flat flame has been previously reported in the literature, where a swirling flow can transition from an open jet flow with high swirl to a Coanda jet flow (CJF) [152]. This transition is associated with high swirl numbers causing vortex breakdown to move further upstream into the nozzle until a negative axial velocity is found within the nozzle itself, forcing a transition to a CJF [153]. This would suggest a longer nozzle like in the Sg = 1.75 long nozzle case would be more susceptible to forming a CJF as the vortex breakdown would not have to travel so far axially before triggering the transition to CJF. Furthermore, the transition to CJF has been found to be more likely to occur with higher swirl numbers, and a higher swirl number is required to form a CJF when Reynolds number increases[154]. As the thermal power is constant in this study, the Reynolds number increases with a reduction in equivalence ratio. This could explain why only the S_g = 1.75 long nozzle case formed a Coanda jet flow flame. It is the only case which has both a long enough nozzle and high enough swirl number to form a CJF at the relatively high Reynolds number found at $\Phi = 0.7$ as the vortex breakdown becomes dominant with reduced heat release rates at lean conditions. This CJF flame was observed for the S_g = 1.75 long nozzle case at 5kW thermal power, but not at 15 kW. This could be because it was not experimentally possible to reach lean enough conditions for it to form at 15 kW, or because the Reynolds number was too high at 15 kW for a CJF to form at this swirl number.

It can also be seen that both the long nozzle cases had a narrow flame root, anchored to the bluff body. In comparison the short nozzle cases both anchored on the nozzle outlet instead, resulting in a lower flame base angle and wider, more open flame. It is posited that this is a desirable characteristic for maintaining static flame stability at high thermal powers with high dump plane velocities.

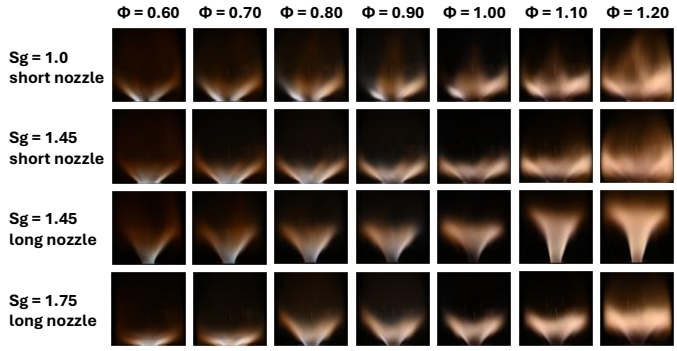

Fig. 6.3: Flame images for each of the swirlers examined at a range of equivalence ratios. Thermal Power 10 kW. Image area 160 x 160 mm.

These same conditions were examined in more detail by utilising chemiluminescence imaging of OH*, NH* and NH_2*, shown in Fig. 6.4. As expected, similar findings in terms of flame length, base angle and anchoring location as from the direct line of sight photos in Fig. 6.3 can be seen again. However, some new information can still be gained. For example, for the short nozzle cases – at stoichiometric and slightly rich conditions, the radical intensity of OH*, NH* and NH_2* was reduced in the region near the nozzle. This is clearest to see for NH_2*, with the highest intensity region being relatively far from the nozzle outlet. In comparison, both long nozzle cases and for S_g = 1.45 in particular, radical intensity is still strong near the nozzle even at Φ = 1.2. Assuming some combination of OH*, NH* and NH_2* intensity can be used to represent heat release rate [104,155–157], the short nozzle cases having this centre of intensity farther away from the nozzle may reduce thermal degradation of the nozzle material over extended periods of use.

A difference in radical distribution and density between the swirlers can be seen in Fig. 6.4. All cases had a relatively compact distribution of OH*, NH* and NH_2* radicals at Φ = 0.8. The two swirlers with short nozzles however had broadly distributed radicals with low density at Φ = 1.0 and 1.2. The S_g = 1.45 long nozzle case was the only case to maintain a high radical density with a clearly defined flame front at Φ = 1.2. These variations in distribution and density of key radicals with different swirl number and nozzle design may provide potential for controlling emissions.

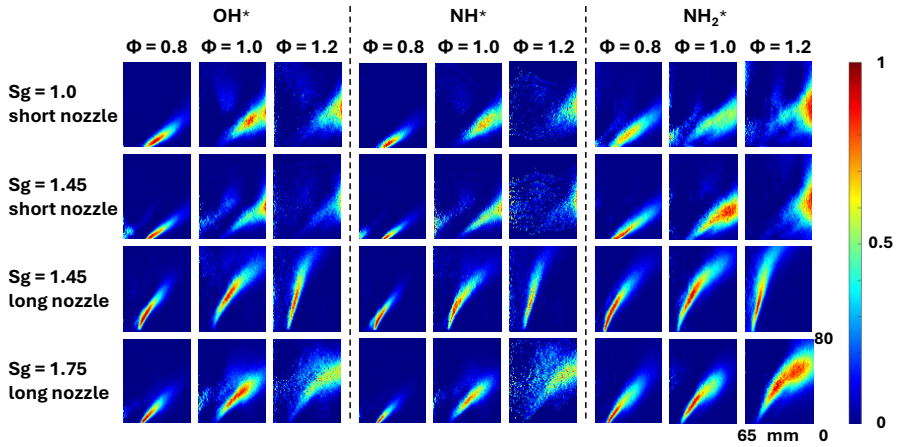

Fig. 6.4: Right half of Abel transformed chemiluminescence images (OH, NH* and NH_2*) for each of the four cases at lean, stoichiometric and rich conditions and 10 kW. Colourmap of images normalised to each image's maximum intensity.*

Fig. 6.5 below shows the static stability map for each of the swirlers at a range of thermal powers. Lean blowoff (LBO) was found to be relatively independent of swirl number and nozzle geometry, with all cases having a similar LBO limit of around Φ = 0.4 at 5 kW and 10 kW thermal power. Lean blowoff limits could not be reached here for 15 kW thermal power as the maximum flowrate of the air was 500 SLPM, representing roughly Φ = 0.5 – at which all cases still had a stable flame. This is not an unprecedented finding, with Zhang et al. [158] previously reporting changes in swirl number having no apparent effect on extending LBO limits of pure NH_3 flames. One potential explanation for this relates to Lewis number and consumption rates. Su et al. [151] found that in an 18 % cracked NH_3 blend (with Lewis number <1), consumption rates of NH_3 and H_2 in the shear layer region increased as LBO was approached. This locally increased flame temperature, strengthening combustion near LBO. The opposite was found for fuels with Lewis number greater than unity, such as propane.

The S_g = 1.45 long nozzle case had the highest rich blowoff limits (RBO) at 5 kW, likely related to its jet-like behaviour, which meant it did not have to rely on the establishment of strong recirculation zones for stability. However, as thermal power – and hence dump plane velocity – increased, the RBO limit for the S_g = 1.45 long nozzle case reduced as low as Φ = 1.46. This was due to an observed pinch-off phenomenon, where the flame separated into two parts – the long, jet like base and a more open cone shape at the head. This cone became detached from the base of the flame due to the high axial velocity at elevated thermal powers, eventually causing RBO. The beginnings of this effect can be seen at rich conditions in Fig. 6.3 and Fig. 6.4. This phenomenon was also observed for the S_g = 1.75 long nozzle case, but not to as extreme a degree. Conversely, as thermal power and dump plane velocity increased, the two short nozzle cases

were able to form strong recirculation zones – not present at rich 5 kW conditions – widening rich stability limits significantly. It is posited that the short CRZ from the long nozzle causes high local curvature and stretch just downstream of the CRZ as the flow meets the central axis. As equivalence ratio increases, this highly strained region experiences local extinction, which causes the downstream flow to detach, resulting in blow-off. This pinch-off phenomenon has been previously observed by Zhang et al. [158] in pure NH_3 and 50/50 NH_3/H_2 flames, who suggested it was due to excessive stretch causing local extinction and a reduction in heat release rate.

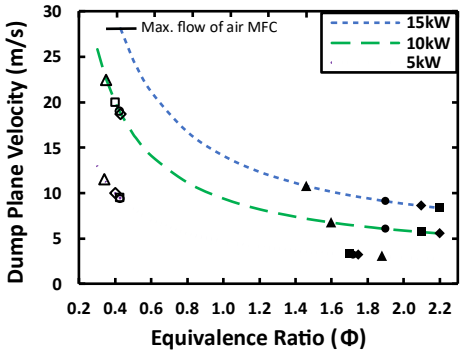

Fig. 6.5: Static stability map representing LBO and RBO for each of the swirlers at three thermal powers. Empty and filled symbols represent LBO and RBO, respectively. Squares for S_g = 1.0 short nozzle, diamonds for S_g = 1.45 short nozzle, triangles for S_g = 1.45, circles for S_g = 1.75 long nozzle.

To test the idea of the short nozzle enabling the flame to become wider with more resistance to necking and hence better performance at higher thermal powers, the swirl burner was placed into a larger combustor, as discussed in Section 6.2.1. Here, the same S_g = 1.45 long and short nozzles were tested at 100 kW and stoichiometric conditions. No modifications were made to the swirlers, nozzles nor burner architecture, the only difference was the size of the confinement downstream of the dump plane. Fig. 6.6 shows there were significant differences in flame morphology. As in Fig. 6.3 and Fig. 6.4, the S_g = 1.45 long nozzle case presented as a near jet-like flame, anchored on the bluff body and with little in terms of external recirculation zones (ERZ) visible. The 100 kW condition shown here was the upper limit of stable flame achievable for the S_g = 1.45 long nozzle case. Additionally, the blowoff mechanism of "necking" or "pinch off" is clear to see in this photo. In comparison, the short nozzle case had a much lower flame angle, and a more classic V-shape flame anchored on the nozzle outlet. This difference in anchoring position is highlighted by the white lines superimposed on to both images, which demarcates the edge of

the nozzle outlet, which was the same on both nozzles at 1.4 D. The short nozzle case also exhibits higher flame intensity, suggesting higher combustion efficiency.

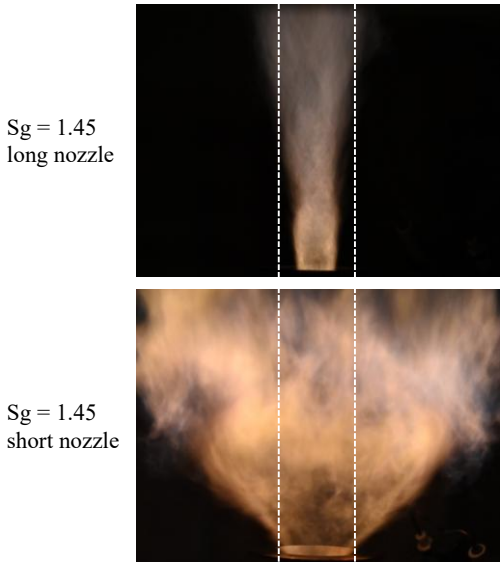

Fig. 6.6: Flame images of the Sg = 1.45 swirler with the long (top) and short (bottom) nozzles at a thermal power of 100 kW and Φ = 1.0. Aperture = F/4, exposure time = 1/400 s and ISO = 4000. Each image represents an area of 200 x 150 mm. White lines denote the diameter of the nozzle outlet, which was 1.4 D for both nozzles.

6.3.2. Exhaust Gas Emissions

Having identified the potential for the short nozzle cases to improve static flame stability at elevated powers, the emissions performance was then examined.

Fig. 6.7 shows the emissions of NO, NO_2, NH_3 and N_2O for the four swirlers at 10kW thermal power. The first noticeable result is at Φ = 0.6 where flame instabilities caused a simultaneous and trend defying increase in NO and NH_3 emissions for three out of the four swirl cases, with the S_g = 1.75 long nozzle case being seemingly unaffected. The increase in NO here is posited to be related to small flame instabilities approaching lean blowoff which may cause local extinction. This could result in regions with slightly elevated – but still lean – local equivalence ratios, resulting in higher NO production. The S_g = 1.75 long nozzle case being unaffected is likely related to the significant difference in flame morphology shown in Fig. 6.3, where S_g = 1.75 long nozzle had a short, flat flame. Although this appears to present a desirable emissions profile with low NO and low unburned NH_3, the N_2O emissions here for S_g = 1.75 long nozzle – although relatively low compared to the other three swirlers – was still prohibitively high at around 450 ppm.

For Φ > 0.7 in Fig. 6.7, overall emissions trends were more consistent. At Φ = 0.7, NO and N_2O emissions appear linked, with reverse trends in terms of best emissions performance. For NO, S_g

= 1.45 long had the lowest emissions, followed by S_g = 1.0 short, S_g = 1.45 short and then S_g = 1.75 long. This is the same order for descending flame length, as seen in Fig. 6.8, suggesting this is related to flame length and hence residence time. The exact opposite order can be seen for N_2O. NO production is related to N_2O production via the reaction shown in Equation (6-2) [85]. Fig. 6.8 shows that for the S_g = 1.75 long nozzle case at Φ = 0.7, NH* and OH* intensity is concentrated near to the nozzle, with a nearly flat flame. This suggests that the NO formed from OH and NH via the HNO pathway described in Equations (6-3) and (6-4) [85] will be formed near the nozzle. Then, for the S_g = 1.75 long nozzle case, as there is little NH concentration axially downstream of the nozzle, there is little residence time for the NO to be converted into N_2O by NH. This would account for the high NO and low N_2O emissions profile shown for the S_g = 1.75 long nozzle case and the reverse shown for the S_g = 1.45 long nozzle case at Φ = 0.7 in Fig. 6.7. Additionally, a study from Rieth et al. [159] found that high positive curvature in very lean partially cracked ammonia flames caused an increase in consumption of N_2O by the reaction show in Equation (6-5) due to fast diffusion of hydrogen. Fig. 6.3 and Fig. 6.8 show high rates of positive curvature in the region near the nozzle for the S_g = 1.75 swirler at Φ = 0.6 and 0.7, which may also contribute to the low N_2O emissions found here in Fig. 6.7. They also found that positive curvature can decrease NO emissions at very lean conditions of Φ = 0.45, while the opposite is true at Φ = 0.9. Although the authors did not suggest an exact crossover equivalence ratio for this effect, it may explain why NO emissions remained comparatively low at Φ = 0.6 but comparatively high at Φ = 0.7 for the S_g = 1.75 case in Fig. 6.7. The findings of increased NO at positively curved regions from [160] due to preferential diffusion of H_2 also support this increase at Φ = 0.7 for the S_g = 1.75 case.

$$NH + NO \leftrightarrow N_2O + H \quad (6\text{-}2)$$

$$NH + OH \leftrightarrow HNO + H \quad (6\text{-}3)$$

$$HNO + H \leftrightarrow NO + H_2 \quad (6\text{-}4)$$

$$N_2O + H \leftrightarrow OH + N_2 \quad (6\text{-}5)$$

Temperatures measured by an R-type thermocouple situated 50mm upstream of the combustor exit is shown in Fig. 6.9. Discounting the flat flame phenomenon found for the S_g = 1.75 long nozzle case at Φ < 0.8, a very clear trend can be seen. Due to the fixed location of the thermocouple, measured temperatures in the post-flame zone were a function of flame length, with the exhaust from shorter flames having a longer time for heat loss to the confinement wall to reduce temperatures. At Φ = 0.7, measured temperatures also correlated with the order of flame length for each of the cases, as shown in Fig. 6.8.

Discounting outliers due to flame instabilities at Φ = 0.6, NO emissions peaked for all cases at Φ = 0.9 and reached negligible values at Φ = 1.15. In this study, emissions were considered negligible when the gas analyser measured 0.0 ppmv. The lowest emissions of NO were found with the S_g = 1.45 long nozzle case. There are clear trends with the Sg = 1.0 short nozzle case offering the next best NO performance, followed by the other short nozzle case and then the Sg = 1.75 long nozzle case. This shows that NO emissions are dependent on both swirl number and nozzle geometry, with good performance achievable with low swirl and a short nozzle, as well as medium swirl and a long nozzle. For the S_g = 1.45 case, NO emissions were generally lower with a longer nozzle. This could potentially also relate to flame length, with the longer nozzle producing a longer flame with enhanced residence time for the consumption of NO by NH_2. Emissions of unburned NH_3 followed the opposite trend, measured at sub 5ppmv for $0.7 < \Phi \leq 1.0$ and rapidly increasing at rich conditions for all swirlers. Negligible emissions of N_2O were recorded for $\Phi > 0.9$ due to flame temperatures and residence times increasing sufficiently to consume N_2O fully. If N_2O emissions were solely temperature dependent, it could be expected for them to increase again at rich conditions, as Fig. 6.9 shows similarly low temperatures for $\Phi > 1.1$ and $\Phi < 0.8$. However, the long flames shown in Fig. 6.3 at rich conditions facilitate the conversion of N_2O back into NO, despite lower temperatures. Emissions of NO_2 followed similar trends to NO and reached negligible values at Φ = 1.05 so are therefore not discussed in detail in the present paper.

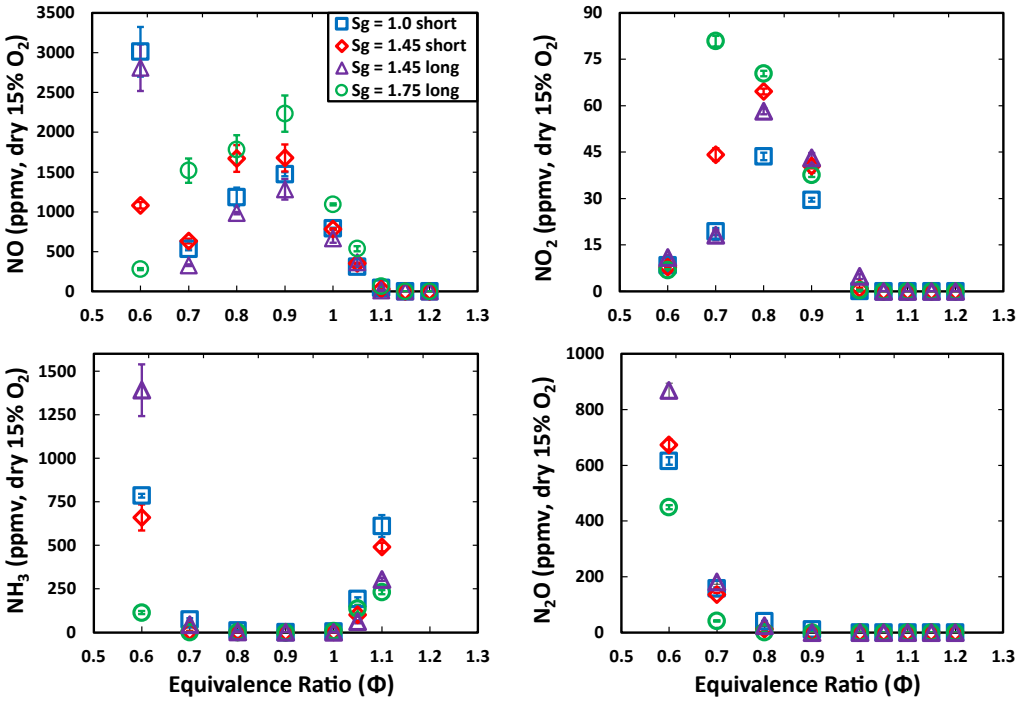

Fig. 6.7: Sampled emissions with changing equivalence ratio at 10 kW thermal power for the four swirler cases. Out of range NH_3 above Φ = 1.1 not plotted.

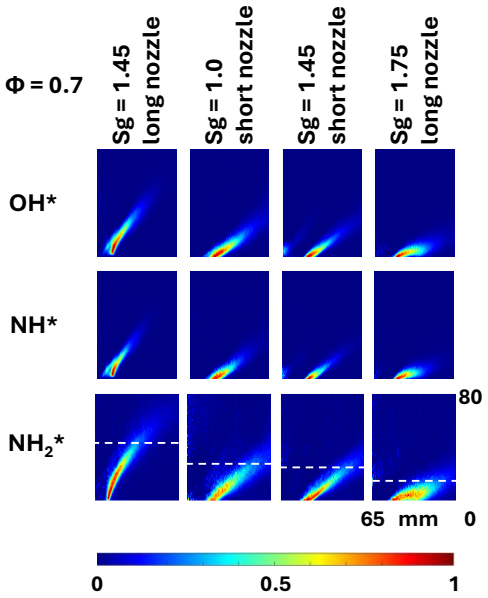

Fig. 6.8: Right half of Abel transformed chemiluminescence images (OH, NH* and NH_2*) for each of the four cases at Φ = 0.7 and 10 kW. Colourmap of images normalised to each image's maximum intensity. White dashed lines on NH_2* images denote flame height.*

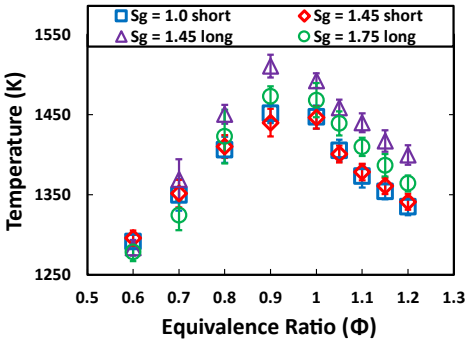

Fig. 6.9: Temperature measured in the post-flame zone 50 mm upstream of the combustor exit (corrected for radiative and convective heat loss from the thermocouple.

As the lean conditions plotted in Fig. 6.7 do not present simultaneously low NO, N_2O and NH_3 emissions, attention is turned to slightly rich conditions instead. Fig. 6.10 below shows the emissions of NO and NH_3 for the four swirlers. For $\Phi \leq 1.05$, these emissions comprise mainly of NO, and at $\Phi = 1.1$, the emissions are mainly unburned NH_3. The lower limit found for emissions at any equivalence ratio was with the $S_g = 1.45$ long nozzle case, reaching 318 ppm comprising 14 ppm NO and 304 ppm NH_3, with negligible NO_2 and N_2O emissions at $\Phi = 1.1$. This represents good potential for the primary stage of an air staged combustor, with a secondary air stage to burn the remnant NH_3. The $S_g = 1.45$ short nozzle case had 30 ppm NO emissions but 60% higher NH_3 emissions. The reason for the significant increase in unburned NH_3 for the short nozzle case may be related to the confinement diameter. Due to the short nozzle causing the flames to open significantly more than the long nozzles, flame impingement on the quartz glass cylinder may be an issue, as suggested for the $\Phi = 1.2$ images in Fig. 6.4. Flame impingement on the confinement walls would increase heat loss, hence reducing combustion efficiency. This is confirmed in Fig. 6.9, which shows the two short nozzles had the lowest measured post-flame zone temperatures. Due to these cases having equal flowrates and consequently equal adiabatic flame temperatures, the measured differences can only be due to differences in heat losses. It should be noted that the elevated NH_3 emissions measured with the short nozzles could be avoided by slightly increasing the diameter of the confinement. It is not expected to be an issue with the industrial system shown in Fig. 6.6 due to it having a confinement diameter nearly 5x larger than the lab-scale system shown in Fig. 6.1. The industrial system will also feature a scaled-up version of the burner presented in this study. Despite this, the future pairing possesses an expansion ratio from burner dump plane area to confinement area of 82.8, which is significantly higher than the expansion ratio of 50.1 in the lab-scale system. This should prevent any flame impingement on the confinement walls and associated increase in NH_3 emissions.

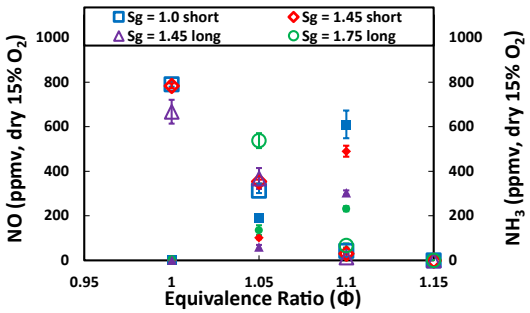

Fig. 6.10: Emissions of NO and NH_3 at slightly rich conditions and 10 kW thermal power for the four swirler cases. Out of range NH_3 above $\Phi = 1.1$ not plotted. Open and solid symbols represent NO and NH_3 respectively.

6.4. Conclusions

In this study, the effect of varying swirl number and nozzle geometry was investigated for 20 % cracked ammonia flames at a wide range of equivalence ratios ($0.3 < \Phi < 2.2$) and thermal powers of 5, 10, 15 and 100 kW.

Stable flames were achieved across a broad range of equivalence ratios with varying thermal power, swirl number and nozzle geometry. Flame morphology was strongly influenced by both swirl number and nozzle length, Notably, the case with the highest swirl number and a long nozzle exhibited a flat, Coanda jet flow flame at the leanest conditions.

Swirl number and nozzle geometry were found to have little effect on lean blowoff limits, supporting previous studies in the literature which suggest flames with a Lewis number below unity increase fuel consumption and hence increase flame temperature and burning velocity when approaching lean blowoff.

Conversely, a shorter nozzle resulted in significantly higher rich blowoff limits by widening the flame brush to avoid jet-like flames which are prone to pinching off. It is suggested that a long nozzle restricts the flow downstream of the dump plane from expanding radially, hindering the formation of the ERZ and shortening the CRZ. The confinement of the nozzle may result in a highly strained region just downstream of the CRZ which experiences local extinction as equivalence ratio increases, causing the downstream section of the flame to detach, resulting in rich blowoff. A wide flame brush was demonstrated to be a desirable characteristic in preventing this process and thus achieving higher thermal power for a given nozzle throat diameter.

While the S_g = 1.45 long nozzle case offered the lowest NO emissions, NO emissions with the Sg = 1.0 short nozzle case were not significantly higher. This shows that various permutations of nozzle geometry and swirl number can achieve similar NO emissions. For a constant geometric

swirl number of 1.45, the long nozzle generally had slightly lower emissions, potentially due to the longer nozzles providing longer flames with increased residence time for consumption of NO by NH_2. However, at rich conditions this difference was smaller, and both long and short nozzles reached negligible NO emissions by $\Phi = 1.15$. With a wider flame brush, it is important to avoid flame impingement upon confinement walls, which can lead to increased local heat loss and hence reduced combustion efficiency.

7. Conclusions and Future Work

7.1. Summary of Key Findings

This work consists of an extensive investigation into various methodologies for reducing emissions from partially cracked ammonia swirl flames, as well as an investigation into nozzle and swirler design for scaling up towards industrially useful thermal powers. The specific quantifications discussed here should not be considered universal as they are dependent on the burner architecture. The overall trends however are likely to be relatively generic and architecture neutral. Objective 1 was to determine whether the nitrogen produced during the cracking process should be separated from the hydrogen, which is an expensive process. It was addressed in Chapter 4, and a summary of those findings are below.

- Even when accounting for volumetric dilution effects, the additional nitrogen in the fuel resulted in significantly lower NOx emissions due to changes in flame morphology and reduced temperatures inhibiting HNO production.
- Lower temperatures consequently resulted in slightly narrower lean stability limits and increased emissions of unburned NH_3. However, these issues are not considered disruptive enough to warrant the expensive separation of nitrogen from the fuel blend.

Objective 2 was to identify the optimal equivalence ratio for the combustion of partially cracked ammonia flames through experimental investigation. This was discussed extensively, in all four results chapters. The findings are summarised below.

- Fuel lean combustion below $\Phi = 0.8$ has potential to reduce NO emissions, if flame instabilities can be avoided. However, lean combustion results in prohibitively high emissions of N_2O, a potent greenhouse gas. Therefore, lean combustion should be avoided.
- Fuel rich combustion can also result in low emissions of NO. For 20 % (vol.) cracked ammonia flames, $\Phi = 1.2$ consistently results in negligible NO emissions, below gas analyser detection limits. However, it also results in unburned emissions of NH_3 of the order of 1000 ppm and H_2 emissions of the order of 10,000 ppm, which are not ideal from neither safety nor efficiency perspectives.
- Slightly fuel rich combustion of $1.05 < \Phi < 1.15$ can result in regulatorily compliant NO emissions, with a smaller penalty in emissions of unburned NH_3 and H_2. This range can therefore be considered an optimal equivalence ratio for a primary stage combustor, likely requiring a secondary stage of air injection to consume the remnant fuel fully.

Objectives 3 and 4 revolved around experimentally investigating a range of NOx reduction methodologies including fuel stratification, humidification and heat loss management. The impact on emissions of unburned fuel should be quantified. Numerical chemical reactor networks were to be used to identify the key reactions responsible for any NOx reductions. This research was addressed in Chapters 3, 4 and 5, and the findings are summarised below.

Fuel stratification:

- Reduced NO emissions at stoichiometric and slightly fuel rich conditions by enhancing the consumption of NO by NH_2 and by reducing NO production from OH and HNO pathways. The increased emissions of unburned NH_3 here was offset by a larger reduction in NO.
- At slightly fuel lean conditions, NO emissions increased due to changes in OH and NH production and a reduced intensity of NH_2 resulting in lower NO consumption rates.
- A strong sensitivity to the diffusive equivalence ratio in the stratified flow was found, with slightly lean conditions resulting in the lowest overall NO emissions. This was suggested to be due the concentration of NO production near the central injector resulting in longer residence times for NO consumption by NH_2 in the swirling flow downstream.

Humidification:

- Reduced NO emissions at $\Phi = 0.9$ due to a reduced production of OH and NH and subsequently HNO. At slightly rich conditions, additional NH_2 produced from OH from the H_2O increased consumption of NO.
- N_2O emissions increased at lean conditions due to a reduction in availability of free H atoms stemming from lower temperatures.
- NH_3 emissions increased at rich conditions due to lower temperatures reducing reactivity and instigating flame instabilities.
- H_2 emissions decreased at rich conditions, posited to be due to lower post-flame temperatures thermally cracking less NH_3 into H_2 and N_2.

Heat loss management:

- Slightly increased N_2O emissions at lean conditions due to lower temperatures reducing availability of free H atoms and reduced third body reactivity.
- Significantly lowered NO emissions due to a reduction in HNO production and an increase in NO consumption by NH_2, by shifting temperatures nearer to the peak of NH_2 consumption reactivity.

- NH_3 emissions only slightly increased, representing a favourable trade-off with NO reduction. It is suggested that NH_3 emissions would have been higher if not for the chain branching NH_2 reaction providing fresh OH to consume NH_3.

The final objective was to experimentally investigate how variations in swirler and nozzle geometry influence flame structure and blowoff limits with increasing thermal power. This was addressed in Chapter 6 and the findings are summarised below.

- Flame morphology was strongly influenced by both swirl number and nozzle geometry at a range of equivalence ratios and thermal powers up to 100 kW.
- Swirl number and nozzle geometry had little impact on lean blowoff, supporting previous literature showing burning velocity increases when approaching LBO for fuels with Lewis numbers below unity. This indicates that lean blowoff is more dependent on fuel composition than burner configuration.
- A shorter nozzle increased rich blowoff limits by widening the flame brush and avoiding jet-like flames which are prone to pinching off. It is suggested that this is due to a longer nozzle restricting the flow from opening radially and forming a supporting external recirculation zone. A wide flame brush was demonstrated to be a desirable characteristic in preventing blowoff as gas velocity increased with thermal power to 100 kW. It is important to avoid these wider flames impinging on the confinement walls which can increase emissions of unburned NH_3.
- Similar NO emissions at slightly fuel rich conditions were achievable with various permutations of swirler and nozzle geometry and all configurations reached negligible NO emissions by $\Phi = 1.15$.

In summary, this work furthers the understanding of NOx reduction methodologies in partially cracked ammonia flames and their subsequent impact on combustion efficiency. It also outlines critical research findings for scaling up swirl burners to higher thermal powers for industrial applications.

7.2. Original Contributions to Field

This work advances the understanding of partially cracked ammonia as a fuel in swirl burners, with particular focus on NOx reduction strategies and scaling to higher thermal powers. For the first time, the effects of fuel stratification, humidification and heat loss management on partially cracked ammonia flames are systematically evaluated.

The influence of the diffusive equivalence ratio of H_2 in stratified flames on emissions is examined, alongside simultaneous measurements of major species – including H_2 – in humidified ammonia-based combustion. The volumetric dilution effect from steam and nitrogen addition were accounted for to isolate their true impact on emissions. An application-relevant swirl burner with integrated heat exchanger to raise steam directly from the flame – rather than external electrical heating systems – was employed. A novel approach to NOx control using heat loss management is introduced, demonstrating enhanced consumption of NO by NH_2.

Also, for the first time, an investigation of optimal swirl number and nozzle design for the scale-up of partially cracked ammonia flames towards industrially applicable thermal powers was conducted. Desirable nozzle design characteristics for mitigating blowoff risk at elevated gas velocities were identified.

7.3. Future Work

Future research on this topic should concentrate on the integration of these NOx control methodologies within an air-staged combustor to achieve simultaneously minimal NOx, NH_3 and H_2 emissions. The air injection strategy must be carefully examined to avoid the production of fresh NO or N_2O emissions within the secondary stage. A list of considerations for this future work include:

- Determination of optimal residence time between first stage and second stage. Too short a residence time and NOx consumption reactions may not have sufficient time to complete. Too long a residence time and temperatures may cool too much for autoignition.
- Investigation of optimal global equivalence ratio, or how much secondary air to inject. If too little air is injected, there is a risk of incomplete combustion. Too much air is likely to result in reduction of temperatures and an oxygen rich environment producing N_2O emissions.
- Research into air preheating, which may assist in preventing the formation of N_2O. Practical considerations here would include how to integrate the air preheating into an industrial combustion system.
- Systematic study into air injection configurations. Good mixing between the unburned fuel and additional air must occur in order to achieve full consumption of the unburned fuel.

If the above considerations are sufficiently investigated, it may be possible to achieve high combustion efficiency and low NOx emissions. A primary fuel rich stage with the above NOx reduction methodologies should be able to produce low NO and NH_3 emissions with negligible NO_2 and N_2O emissions. As a result, the exhaust gas entering the second stage should comprise mainly N_2, H_2O and a few percent H_2. In other words, the second stage could be ultra-lean hydrogen/air combustion, avoiding thermal NOx due to high dilution. Any unconsumed NH_3 from the primary stage is likely to convert to NO in this scenario, but it may be low enough concentrations to achieve regulatory compliance without after-treatment systems.

Additionally, continued development in terms of scale-up of the swirl burner presented in this study towards higher thermal powers of the order of 1 MW should be carried out.

References

[1] International Energy Agency (IEA). CO2 Emissions in 2023. Paris: 2024.

[2] Intergovernmental Panel on Climate Change (IPCC). Climate Change 2022: Impacts, Adaptation and Vulnerability. Summary for Policymakers. New York: Morgan Wairiu; 2022. https://doi.org/10.1017/9781009325844.001.

[3] United Nations Framework Convention on Climate Change (UNFCCC). Paris Agreement to the United Nations Framework Convention on Climate Change. Paris: 2015.

[4] Department for Energy Security and Net Zero. Net Zero Strategy: Build Back Greener. 2021.

[5] Office for National Statistics. Measuring UK greenhouse gas emissions. 2024.

[6] Owen A, Ivanova D, Barrett J, Cornelius S, Francis A, Matheson S, et al. Exploring the UK's contribution to climate change. London: 2020.

[7] Carbon Brief. Analysis: UK's electricity was cleanest ever in 2024 . 2025.

[8] The Crown Estate. UK Offshore Wind Report 2023. 2024.

[9] International Atomic Energy Agency (IAEA). Non-baseload Operation in Nuclear Power Plants: Load Following and Frequency Control Modes of Flexible Operation. 2018.

[10] International Renewable Energy Agency (IRENA). Flexibility in Conventional Power Plants. 2019.

[11] Barbour E, Wilson IAG, Radcliffe J, Ding Y, Li Y. A review of pumped hydro energy storage development in significant international electricity markets. Renewable and Sustainable Energy Reviews 2016;61:421–32. https://doi.org/10.1016/J.RSER.2016.04.019.

[12] Niaz H, Zarei M, Shams MH, Won W, Liu JJ. Curtailment to cashflow: Exploring BESS and hydrogen for renewable energy profitability. J Energy Storage 2024;77:109990. https://doi.org/10.1016/J.EST.2023.109990.

[13] Andersson J, Grönkvist S. Large-scale storage of hydrogen. Int J Hydrogen Energy 2019;44:11901–19. https://doi.org/10.1016/J.IJHYDENE.2019.03.063.

[14] Chatterjee S, Parsapur RK, Huang KW. Limitations of Ammonia as a Hydrogen Energy Carrier for the Transportation Sector. ACS Energy Lett 2021;6:4390–4. https://doi.org/10.1021/ACSENERGYLETT.1C02189.

[15] Cheng J, Zhang B. Experimental study on the explosion characteristics of ammonia-hydrogen-air mixtures. Fuel 2024;363:131046. https://doi.org/10.1016/J.FUEL.2024.131046.

[16] Schefer RW, Kulatilaka WD, Patterson BD, Settersten TB. Visible emission of hydrogen flames. Combust Flame 2009;156:1234–41. https://doi.org/10.1016/J.COMBUSTFLAME.2009.01.011.

[17] Weng W, Aldén M, Li Z. Visible chemiluminescence of ammonia premixed flames and its application for flame diagnostics. Proceedings of the Combustion Institute 2023;39:4327–34. https://doi.org/10.1016/J.PROCI.2022.08.012.

[18] Smeets MAM, Bulsing PJ, van Rooden S, Steinmann R, de Ru JA, Ogink NWM, et al. Odor and Irritation Thresholds for Ammonia: A Comparison between Static and Dynamic Olfactometry. Chem Senses 2007;32:11–20. https://doi.org/10.1093/CHEMSE/BJL031.

[19] Guo ZX, Shang C, Aguey-Zinsou KF. Materials challenges for hydrogen storage. J Eur Ceram Soc 2008;28:1467–73. https://doi.org/10.1016/J.JEURCERAMSOC.2007.12.019.

[20] International Energy Agency (IEA). Executive Summary – Ammonia Technology Roadmap – Analysis - IEA. Paris: 2021.

[21] International Energy Agency (IEA). Executive summary – Global Hydrogen Review 2024 – Analysis - IEA. Paris: 2024.

[22] Li S, Zhou Y, Fu X, Pedersen JB, Saccoccio M, Andersen SZ, et al. Long-term continuous ammonia electrosynthesis. Nature 2024 629:8010 2024;629:92–7. https://doi.org/10.1038/s41586-024-07276-5.

[23] Shikder MFH, Tang Y, Almehdawe E, Araújo JC. Risk incident analyses in the transportation of anhydrous ammonia as an emerging clean energy resource. Risk Analysis 2024. https://doi.org/10.1111/RISA.17634.

[24] Kojima Y, Yamaguchi M. Ammonia as a hydrogen energy carrier. Int J Hydrogen Energy 2022;47:22832–9. https://doi.org/10.1016/J.IJHYDENE.2022.05.096.

[25] Wenli D, Dam-Johansen K, Østergaard K. Widening the temperature range of the thermal DeNOx process. An experimental investigation. Symposium (International) on Combustion 1991;23:297–303. https://doi.org/10.1016/S0082-0784(06)80273-0.

[26] Blejchař T, Konvička J, Von Der Heide B, Malý R, Maier M. High Temperature Modification of SNCR Technology and its Impact on NOx Removal Process. EPJ Web Conf 2018;180:02009. https://doi.org/10.1051/EPJCONF/201818002009.

[27] Wärtsilä. Wärtsilä 25 marine engine n.d. https://www.wartsila.com/marine/products/engines-and-generating-sets/dual-fuel-engines/wartsila-25 (accessed April 16, 2025).

[28] MAN Energy Solutions. Ammonia I Future fuels n.d. https://www.man-es.com/marine/strategic-expertise/future-fuels/ammonia? (accessed April 16, 2025).

[29] Nature. Ammonia: the future fuel with sustainable potential n.d. https://www.nature.com/articles/d42473-024-00441-4 (accessed April 16, 2025).

[30] Samsung C&T is Building Korea's First Ammonia Import Terminal for Co-Firing Power Generation - Samsung C&T Newsroom n.d. https://news.samsungcnt.com/en/features/engineering-construction/2024-07-samsung-cnt-is-building-koreas-first-ammonia-import-terminal-for-co-firing-power-generation/ (accessed April 17, 2025).

[31] Kobayashi H, Hayakawa A, Somarathne KDKA, Okafor EC. Science and technology of ammonia combustion. Proceedings of the Combustion Institute 2019;37:109–33. https://doi.org/10.1016/J.PROCI.2018.09.029.

[32] Asif M, Sidra Bibi S, Ahmed S, Irshad M, Shakir Hussain M, Zeb H, et al. Recent advances in green hydrogen production, storage and commercial-scale use via catalytic ammonia cracking. Chemical Engineering Journal 2023;473:145381. https://doi.org/10.1016/J.CEJ.2023.145381.

[33] Schüth F, Palkovits R, Schlögl R, Su DS. Ammonia as a possible element in an energy infrastructure: catalysts for ammonia decomposition. Energy Environ Sci 2012;5:6278–89. https://doi.org/10.1039/C2EE02865D.

[34] Bell TE, Torrente-Murciano L. H2 Production via Ammonia Decomposition Using Non-Noble Metal Catalysts: A Review. Top Catal 2016;59:1438–57. https://doi.org/10.1007/S11244-016-0653-4/TABLES/2.

[35] Pashchenko D, Mustafin R. Ammonia decomposition in the thermochemical waste-heat recuperation systems: A view from low and high heating value. Energy Convers Manag 2022;251:114959. https://doi.org/10.1016/J.ENCONMAN.2021.114959.

[36] Syred N, Beér JM. Combustion in swirling flows: A review. Combust Flame 1974;23:143–201. https://doi.org/10.1016/0010-2180(74)90057-1.

[37] Strakey P, Sidwell T, Ontko J. Investigation of the effects of hydrogen addition on lean extinction in a swirl stabilized combustor. Proceedings of the Combustion Institute 2007;31:3173–80. https://doi.org/10.1016/J.PROCI.2006.07.077.

[38] Huang Y, Yang V. Dynamics and stability of lean-premixed swirl-stabilized combustion. Prog Energy Combust Sci 2009;35:293–364. https://doi.org/10.1016/J.PECS.2009.01.002.

[39] Claypole T, Syred N. The effect of swirl burner aerodynamics on NOx formation. Symposium (International) on Combustion 1981;18:81–9. https://doi.org/https://doi.org/10.1016/S0082-0784(81)80013-6.

[40] Lewis B, von Elbe G. Stability and structure of burner flames. J Chem Phys 1943;11:75–97. https://doi.org/10.1063/1.1723808.

[41] Fritz J, Kröner M, Sattelmayer T. Flashback in a Swirl Burner With Cylindrical Premixing Zone. J Eng Gas Turbine Power 2004;126:276–83. https://doi.org/10.1115/1.1473155.

[42] Syred N, Abdulsada M, Griffiths A, O'Doherty T, Bowen P. The effect of hydrogen containing fuel blends upon flashback in swirl burners. Appl Energy 2012;89:106–10. https://doi.org/10.1016/J.APENERGY.2011.01.057.

[43] Jeong SY, Jang D, Lee MC. Property-based quantitative risk assessment of hydrogen, ammonia, methane, and propane considering explosion, combustion, toxicity, and environmental impacts. J Energy Storage 2022;54:105344. https://doi.org/10.1016/J.EST.2022.105344.

[44] Verkamp FJ, Hardin MC, Williams JR. Ammonia combustion properties and performance in gas-turbine burners. Symposium (International) on Combustion 1967;11:985–92. https://doi.org/10.1016/S0082-0784(67)80225-X.

[45] Shrestha KP, Lhuillier C, Barbosa AA, Brequigny P, Contino F, Mounaïm-Rousselle C, et al. An experimental and modeling study of ammonia with enriched oxygen content and ammonia/hydrogen laminar flame speed at elevated pressure and temperature. Proceedings of the Combustion Institute 2021;38:2163–74. https://doi.org/10.1016/J.PROCI.2020.06.197.

[46] Kurata O, Iki N, Matsunuma T, Inoue T, Tsujimura T, Furutani H, et al. Performances and emission characteristics of NH3–air and NH3CH4–air combustion gas-turbine power

generations. Proceedings of the Combustion Institute 2017;36:3351–9. https://doi.org/10.1016/J.PROCI.2016.07.088.

[47] Okafor EC, Somarathne KDKA, Hayakawa A, Kudo T, Kurata O, Iki N, et al. Towards the development of an efficient low-NOx ammonia combustor for a micro gas turbine. Proceedings of the Combustion Institute 2019;37:4597–606. https://doi.org/10.1016/J.PROCI.2018.07.083.

[48] Hayakawa A, Arakawa Y, Mimoto R, Somarathne KDKA, Kudo T, Kobayashi H. Experimental investigation of stabilization and emission characteristics of ammonia/air premixed flames in a swirl combustor. Int J Hydrogen Energy 2017;42:14010–8. https://doi.org/10.1016/J.IJHYDENE.2017.01.046.

[49] Konnov AA. An exploratory modelling study of chemiluminescence in ammonia-fuelled flames. Part 1. Combust Flame 2023;253:112788. https://doi.org/10.1016/J.COMBUSTFLAME.2023.112788.

[50] Zhu X, Khateeb AA, Roberts WL, Guiberti TF. Chemiluminescence signature of premixed ammonia-methane-air flames. Combust Flame 2021;231:111508. https://doi.org/10.1016/J.COMBUSTFLAME.2021.111508.

[51] Han X, Wang Z, Costa M, Sun Z, He Y, Cen K. Experimental and kinetic modeling study of laminar burning velocities of NH3/air, NH3/H2/air, NH3/CO/air and NH3/CH4/air premixed flames. Combust Flame 2019;206:214–26. https://doi.org/10.1016/J.COMBUSTFLAME.2019.05.003.

[52] Mashruk S, Vigueras-Zuniga MO, Tejeda-del-Cueto ME, Xiao H, Yu C, Maas U, et al. Combustion features of CH4/NH3/H2 ternary blends. Int J Hydrogen Energy 2022;47:30315–27. https://doi.org/10.1016/J.IJHYDENE.2022.03.254.

[53] Khateeb AA, Guiberti TF, Zhu X, Younes M, Jamal A, Roberts WL. Stability limits and exhaust NO performances of ammonia-methane-air swirl flames. Exp Therm Fluid Sci 2020;114:110058. https://doi.org/10.1016/J.EXPTHERMFLUSCI.2020.110058.

[54] Lai S, Chen D, Zhang J, Xie Y, Fan M, Li X, et al. Blow-Off Limits, Flame Structure, and Emission Characteristics of Lean Partially Premixed Swirl-Stabilized Flames with NH3/CH4. Energy and Fuels 2024;38:4721–32. https://doi.org/10.1021/ACS.ENERGYFUELS.3C04304/ASSET/IMAGES/LARGE/EF3C04304_0014.JPEG.

[55] Li J, Huang H, Kobayashi N, Wang C, Yuan H. Numerical study on laminar burning velocity and ignition delay time of ammonia flame with hydrogen addition. Energy 2017;126:796–809. https://doi.org/10.1016/J.ENERGY.2017.03.085.

[56] Sato D, Davies J, Mazzotta L, Mashruk S, Valera-Medina A, Kurose R. Effects of Reynolds number and ammonia fraction on combustion characteristics of premixed ammonia-hydrogen-air swirling flames. Proceedings of the Combustion Institute 2024;40:105283. https://doi.org/10.1016/J.PROCI.2024.105283.

[57] Ji C, Wang Z, Wang D, Hou R, Zhang T, Wang S. Experimental and numerical study on premixed partially dissociated ammonia mixtures. Part I: Laminar burning velocity of NH3/H2/N2/air mixtures. Int J Hydrogen Energy 2022;47:4171–84. https://doi.org/10.1016/J.IJHYDENE.2021.10.269.

[58] Wiseman S, Gruber A, Dawson JR. Flame Transfer Functions for Turbulent, Premixed, Ammonia- Hydrogen-Nitrogen-Air Flames. J Eng Gas Turbine Power 2023;145. https://doi.org/10.1115/1.4055754/1146534.

[59] An Z, Zhang W, Zhang M, Xing J, Kai R, Lin W, et al. Experimental and Numerical Investigation on Combustion Characteristics of Cracked Ammonia Flames. Energy and Fuels 2024;38:7412–30. https://doi.org/https://doi.org/10.1021/acs.energyfuels.4c00312.

[60] Shohdy NN, Alicherif M, Lacoste DA. Transfer Functions of Ammonia and Partly Cracked Ammonia Swirl Flames. Energies (Basel) 2023;16:1323. https://doi.org/10.3390/EN16031323/S1.

[61] Miller JA, Bowman CT. Mechanism and modeling of nitrogen chemistry in combustion. Prog Energy Combust Sci 1989;15:287–338.

[62] Yan B, Wu Z, Zhou S, Lv J, Liu X, Wu W, et al. A critical review of NH3–H2 combustion mechanisms. Renewable and Sustainable Energy Reviews 2024;196:114363. https://doi.org/10.1016/J.RSER.2024.114363.

[63] Stagni A, Cavallotti C, Arunthanayothin S, Song Y, Herbinet O, Battin-Leclerc F, et al. An experimental, theoretical and kinetic-modeling study of the gas-phase oxidation of ammonia. React Chem Eng 2020;5:696. https://doi.org/10.1039/C9RE00429G.

[64] Alnasif A, Mashruk S, Hayashi M, Jójka J, Shi H, Hayakawa A, et al. Performance Investigation of Currently Available Reaction Mechanisms in the Estimation of NO

Measurements: A Comparative Study. Energies 2023, Vol 16, Page 3847 2023;16:3847. https://doi.org/10.3390/EN16093847.

[65] Hayakawa A, Hayashi M, Kovaleva M, Gotama GJ, Okafor EC, Colson S, et al. Experimental and numerical study of product gas and N2O emission characteristics of ammonia/hydrogen/air premixed laminar flames stabilized in a stagnation flow. Proceedings of the Combustion Institute 2023;39:1625–33. https://doi.org/10.1016/J.PROCI.2022.08.124.

[66] Alnasif A, Jojka J, Papp M, Szanthoffer AG, Kovaleva M, Turányi T, et al. A compact kinetic reaction mechanism for NH3/H2 flames. Journal of Ammonia Energy 2025;3. https://doi.org/10.18573/JAE.46.

[67] Jin U, Kim KT. Hybrid rich- and lean-premixed ammonia-hydrogen combustion for mitigation of NOx emissions and thermoacoustic instabilities. Combust Flame 2024;262:113366. https://doi.org/10.1016/J.COMBUSTFLAME.2024.113366.

[68] Pugh D, Runyon J, Bowen P, Giles A, Valera-Medina A, Marsh R, et al. An investigation of ammonia primary flame combustor concepts for emissions reduction with OH*, NH2* and NH* chemiluminescence at elevated conditions. Proceedings of the Combustion Institute 2021;38:6451–9. https://doi.org/10.1016/J.PROCI.2020.06.310.

[69] Abdullah M, Guiberti TF, Alsulami RA. Experimental Assessment on the Coupling Effect of Mixing Length and Methane-Ammonia Blends on Flame Stability and Emissions. Energies 2023, Vol 16, Page 2955 2023;16:2955. https://doi.org/10.3390/EN16072955.

[70] Wang S, Chong CT, Xie T, Józsa V, Ng JH. Ammonia/methane dual-fuel injection and Co-firing strategy in a swirl flame combustor for pollutant emissions control. Energy 2023;281:128221. https://doi.org/10.1016/J.ENERGY.2023.128221.

[71] Wang S, Chong CT, Józsa V, Chiong MC. Investigation of NO emissions and chemical reaction kinetics of ammonia/methane flames under dual-fuel co-combustion mode at elevated air temperature conditions. Int J Hydrogen Energy 2024;84:968–81. https://doi.org/10.1016/J.IJHYDENE.2024.08.202.

[72] Wang S, Chong CT, Sheykhbaglou S, Ng JH, Tian B, Valera-Medina A. Revealing the NO Formation Kinetics for NH3/CH4 Blends Under Dual-Flame and Premixed Swirl Flame Configurations. Energies 2024, Vol 17, Page 6090 2024;17:6090. https://doi.org/10.3390/EN17236090.

[73] Mashruk S, Alnasif A, Yu C, Thatcher J, Rudman J, Peronski L, et al. Combustion Characteristics of a Novel Ammonia Combustor equipped with Stratified Injection for Low Emissions. Journal of Ammonia Energy 2023;1. https://doi.org/10.18573/JAE.10.

[74] Larson ED, Williams RH. Steam-Injected Gas Turbines. J Eng Gas Turbine Power 1987;109:55–63. https://doi.org/10.1115/1.3240006.

[75] Nishida K, Takagi T, Kinoshita S. Regenerative steam-injection gas-turbine systems. Appl Energy 2005;81:231–46. https://doi.org/10.1016/J.APENERGY.2004.08.002.

[76] Wei C, Zang S. Experimental investigation on the off-design performance of a small-sized humid air turbine cycle. Appl Therm Eng 2013;51:166–76. https://doi.org/10.1016/J.APPLTHERMALENG.2012.08.061.

[77] Reale F, Sannino R. Water and steam injection in micro gas turbine supplied by hydrogen enriched fuels: Numerical investigation and performance analysis. Int J Hydrogen Energy 2021;46:24366–81. https://doi.org/10.1016/J.IJHYDENE.2021.04.169.

[78] Pugh D, Bowen P, Valera-Medina A, Giles A, Runyon J, Marsh R. Influence of steam addition and elevated ambient conditions on NOx reduction in a staged premixed swirling NH3/H2 flame. Proceedings of the Combustion Institute 2019;37:5401–9. https://doi.org/10.1016/J.PROCI.2018.07.091.

[79] Pugh D, Bowen P, Goktepe B, Giles A, Mashruk S, Medina AV, et al. Influence of Steam and Elevated Ambient Conditions on N2O in a Premixed Swirling NH3/H2 Flame. Proceedings of the ASME Turbo Expo 2023;3A-2023. https://doi.org/10.1115/GT2023-102452.

[80] Shi G, Li P, Liu Z, Dally B. Effect of H2O dilution on NOx emissions from the oxidation of NH3/H2 fuel mixture. Proceedings of the Combustion Institute 2024;40:105407. https://doi.org/10.1016/J.PROCI.2024.105407.

[81] Okafor EC, Tsukamoto M, Hayakawa A, Somarathne KA, Kudo T, Tsujimura T, et al. Influence of wall heat loss on the emission characteristics of premixed ammonia-air swirling flames interacting with the combustor wall. Proceedings of the Combustion Institute 2021;38:5139–46. https://doi.org/10.1016/J.PROCI.2020.06.142.

[82] Zhang M, Xu W, Wang R, Wei X, Wang J, Huang Z, et al. Wall heat loss effect on the emission characteristics of ammonia swirling flames in a model gas turbine combustor. Combust Flame 2023;256:112955. https://doi.org/10.1016/J.COMBUSTFLAME.2023.112955.

[83] Correa SM. A review of NOx formation under gas-turbine combustion conditions. Combustion Science and Technology 1993;87:329–62. https://doi.org/https://doi.org/10.1080/00102209208947221.

[84] Valera-Medina A, Pugh DG, Marsh P, Bulat G, Bowen P. Preliminary study on lean premixed combustion of ammonia-hydrogen for swirling gas turbine combustors. Int J Hydrogen Energy 2017;42:24495–503. https://doi.org/10.1016/J.IJHYDENE.2017.08.028.

[85] Mashruk S, Okafor EC, Kovaleva M, Alnasif A, Pugh D, Hayakawa A, et al. Evolution of N2O production at lean combustion condition in NH3/H2/air premixed swirling flames. Combust Flame 2022;244:112299. https://doi.org/10.1016/J.COMBUSTFLAME.2022.112299.

[86] Park YK, Kim BS. Catalytic removal of nitrogen oxides (NO, NO2, N2O) from ammonia-fueled combustion exhaust: A review of applicable technologies. Chemical Engineering Journal 2023;461:141958. https://doi.org/10.1016/J.CEJ.2023.141958.

[87] Khateeb AA, Guiberti TF, Zhu X, Younes M, Jamal A, Roberts WL. Stability limits and NO emissions of technically-premixed ammonia-hydrogen-nitrogen-air swirl flames. Int J Hydrogen Energy 2020;45:22008–18. https://doi.org/10.1016/J.IJHYDENE.2020.05.236.

[88] Mashruk S, Kovaleva M, Alnasif A, Chong CT, Hayakawa A, Okafor EC, et al. Nitrogen oxide emissions analyses in ammonia/hydrogen/air premixed swirling flames. Energy 2022;260:125183. https://doi.org/10.1016/J.ENERGY.2022.125183.

[89] Pugh D, Valera-Medina A, Bowen P, Giles A, Goktepe B, Runyon J, et al. Emissions performance of staged premixed and diffusion combustor concepts for an NH3 air flame with and without reactant humidification. J Eng Gas Turbine Power 2021;143. https://doi.org/10.1115/1.4049451/1093903.

[90] Pugh D, Bowen P, Navaratne R, Goktepe B, Giles A, Medina AV, et al. Influence of Variable Swirl on Emissions in a Non-Premixed Fuel-Flexible Burner at Elevated Ambient Conditions. J Eng Gas Turbine Power 2024;146. https://doi.org/10.1115/1.4063786/1169389.

[91] Khateeb AA, Guiberti TF, Wang G, Boyette WR, Younes M, Jamal A, et al. Stability limits and NO emissions of premixed swirl ammonia-air flames enriched with hydrogen or methane at elevated pressures. Int J Hydrogen Energy 2021;46:11969–81. https://doi.org/10.1016/J.IJHYDENE.2021.01.036.

[92] Ditaranto M, Saanum I. Experimental study on the effect of pressure on single and two stage combustion of decomposed ammonia (NH3 H2 N2) blends over a swirl stabilized burner. Combust Flame 2024;262:113368. https://doi.org/10.1016/J.COMBUSTFLAME.2024.113368.

[93] Srinivasarao M, Kumar S, Jik Lee B, Giri BR, Shrestha KP, Mahendra Reddy V. Experimental and numerical analysis on influence of air staging in a tangential flow burner for pure ammonia combustion. Appl Therm Eng 2025;266:125580. https://doi.org/10.1016/J.APPLTHERMALENG.2025.125580.

[94] Salmon N, Bãnares-Alcántara R. Green ammonia as a spatial energy vector: a review. Sustain Energy Fuels 2021;5:2814–39. https://doi.org/10.1039/D1SE00345C.

[95] Valera-Medina A, Xiao H, Owen-Jones M, David WIF, Bowen PJ. Ammonia for power. Prog Energy Combust Sci 2018;69:63–102. https://doi.org/10.1016/j.pecs.2018.07.001.

[96] Okafor EC, Naito Y, Colson S, Ichikawa A, Kudo T, Hayakawa A, et al. Experimental and numerical study of the laminar burning velocity of CH4–NH3–air premixed flames. Combust Flame 2018;187:185–98. https://doi.org/10.1016/J.COMBUSTFLAME.2017.09.002.

[97] Giddey S, Badwal SPS, Munnings C, Dolan M. Ammonia as a Renewable Energy Transportation Media. ACS Sustain Chem Eng 2017;5:10231–9. https://doi.org/https://doi.org/10.1021/acssuschemeng.7b02219.

[98] Mei B, Zhang J, Shi X, Xi Z, Li Y. Enhancement of ammonia combustion with partial fuel cracking strategy: Laminar flame propagation and kinetic modeling investigation of NH3/H2/N2/air mixtures up to 10 atm. Combust Flame 2021;231:111472. https://doi.org/10.1016/J.COMBUSTFLAME.2021.111472.

[99] Zhu X, Khateeb AA, Guiberti TF, Roberts WL. NO and OH* emission characteristics of very-lean to stoichiometric ammonia–hydrogen–air swirl flames. Proceedings of the Combustion Institute 2021;38:5155–62. https://doi.org/10.1016/J.PROCI.2020.06.275.

[100] Franco MC, Rocha RC, Costa M, Yehia M. Characteristics of NH3/H2/air flames in a combustor fired by a swirl and bluff-body stabilized burner. Proceedings of the Combustion Institute 2021;38:5129–38. https://doi.org/10.1016/J.PROCI.2020.06.141.

[101] British Standards Institute. British Standard ISO 11042-1:1996, Gas turbines. Exhaust Gas Emission Measurement and Evaluation. 1996.

[102] Douglas CM, Shaw SL, Martz TD, Steele RC, Noble DR, Emerson BL, et al. Pollutant Emissions Reporting and Performance Considerations for Hydrogen-Hydrocarbon Fuels in Gas Turbines. J Eng Gas Turbine Power 2022;144. https://doi.org/10.1115/1.4054949/6896265/GTP-22-1225.PDF.

[103] Mashruk S. Nitric oxide formation analysis using chemical reactor modelling and laser induced fluorescence measurements on industrial swirl flames. Cardiff University, 2020.

[104] Mashruk S, Xiao H, Pugh D, Chiong MC, Runyon J, Goktepe B, et al. Numerical Analysis on the Evolution of NH2 in Ammonia/hydrogen Swirling Flames and Detailed Sensitivity Analysis under Elevated Conditions. Combustion Science and Technology 2023;195:1251–78. https://doi.org/10.1080/00102202.2021.1990897.

[105] Chaturvedi S, Santhosh R, Mashruk S, Yadav R, Valera-Medina A. Prediction of NOx emissions and pathways in premixed ammonia-hydrogen-air combustion using CFD-CRN methodology. Journal of the Energy Institute 2023;111:101406. https://doi.org/10.1016/J.JOEI.2023.101406.

[106] Mazzotta L, D'Alessio F, Meloni R, Morris S, Goktepe B, Lamioni R, et al. Modelling Ammonia-Hydrogen-Air Combustion and Emission Characteristics of a Generic Swirl Burner. Proceedings of the ASME Turbo Expo, 2023. https://doi.org/10.1115/GT2023-102803.

[107] van Oijen J, de Goey P. Modelling of premixed laminar flames using flamelet-generated manifolds. Combustion Science and Technology 2000;161:113–37. https://doi.org/10.1080/00102200008935814.

[108] Otomo J, Koshi M, Mitsumori T, Iwasaki H, Yamada K. Chemical kinetic modeling of ammonia oxidation with improved reaction mechanism for ammonia/air and ammonia/hydrogen/air combustion. Int J Hydrogen Energy 2018;43:3004–14. https://doi.org/10.1016/J.IJHYDENE.2017.12.066.

[109] Zimont V, Polifke W, Bettelini M, Weisenstein W. An efficient computational model for premixed turbulent combustion at high reynolds numbers based on a turbulent flame speed closure. J Eng Gas Turbine Power 1998;120:526–32. https://doi.org/10.1115/1.2818178.

[110] Mashruk S, Zitouni S, Brequigny P, Mounaim-Rousselle C, Valera-Medina A. Combustion performances of premixed ammonia/hydrogen/air laminar and swirling flames for a wide

range of equivalence ratios. Int J Hydrogen Energy 2022;47:41170–82. https://doi.org/10.1016/J.IJHYDENE.2022.09.165.

[111] Nicoud F, Poinsot T. Thermoacoustic instabilities: Should the Rayleigh criterion be extended to include entropy changes? Combust Flame 2005;142:153–9. https://doi.org/10.1016/J.COMBUSTFLAME.2005.02.013.

[112] Valera-Medina A, Amer-Hatem F, Azad AK, Dedoussi IC, Joannon M De, Fernandes RX, et al. Review on Ammonia as a Potential Fuel: From Synthesis to Economics 2021. https://doi.org/10.1021/acs.energyfuels.0c03685.

[113] Kang L, Pan W, Zhang J, Wang W, Tang C. A review on ammonia blends combustion for industrial applications. Fuel 2023;332:126150. https://doi.org/10.1016/J.FUEL.2022.126150.

[114] Chai WS, Bao Y, Jin P, Tang G, Zhou L. A review on ammonia, ammonia-hydrogen and ammonia-methane fuels. Renewable and Sustainable Energy Reviews 2021;147:111254. https://doi.org/10.1016/J.RSER.2021.111254.

[115] Elbaz AM, Wang S, Guiberti TF, Roberts WL. Review on the recent advances on ammonia combustion from the fundamentals to the applications. Fuel Communications 2022;10:100053. https://doi.org/10.1016/J.JFUECO.2022.100053.

[116] Mukherjee S, Devaguptapu S V, Sviripa A, Lund CRF, Wu G. Low-temperature ammonia decomposition catalysts for hydrogen generation. Appl Catal B 2018;226:162–81. https://doi.org/10.1016/J.APCATB.2017.12.039.

[117] Božo MG, Vigueras-Zuniga MO, Buffi M, Seljak T, Valera-Medina A. Fuel rich ammonia-hydrogen injection for humidified gas turbines. Appl Energy 2019;251:113334. https://doi.org/10.1016/J.APENERGY.2019.113334.

[118] Hayashi M, Hayakawa A, Kudo T, Kobayashi H. Effects of Water Vapor Dilution on the Laminar Burning Velocity and Markstein Length of Ammonia/Water Vapor/Air Premixed Laminar Flames. Energy and Fuels 2022;36:12341–9. https://doi.org/https://doi.org/10.1021/acs.energyfuels.2c01749.

[119] Valera-Medina A, Vigueras-Zuniga MO, Shi H, Mashruk S, Alnajideen M, Alnasif A, et al. Ammonia combustion in furnaces: A review. Int J Hydrogen Energy 2024;49:1597–618. https://doi.org/10.1016/J.IJHYDENE.2023.10.241.

[120] Berwal P, Kumar S, Khandelwal B. A comprehensive review on synthesis, chemical kinetics, and practical application of ammonia as future fuel for combustion. Journal of the Energy Institute 2021;99:273–98. https://doi.org/10.1016/J.JOEI.2021.10.001.

[121] Teel RB. Stress-corrosion cracking of steels in ammonia with consideration given to OTEC design: a survey. Argonne, IL (United States): 1980. https://doi.org/10.2172/5305036.

[122] Kovaleva M, Dziedzic D, Mashruk S, Evans S, Valera-Medina A, Galindo-Nava E. The Evaluation of Ammonia/Hydrogen Combustion on the H Permeation and Embrittlement of Nickel-Base Superalloys. Proceedings of the ASME Turbo Expo, vol. 7, Rotterdam: American Society of Mechanical Engineers Digital Collection; 2022. https://doi.org/10.1115/GT2022-82239.

[123] Wang D, Ali MA, Sharma K, Almojil SF, Alizadeh A, Alali AF, et al. Multiphase numerical simulation of exergy loss and thermo-hydraulic behavior with environmental cosiderations of a hybrid nanofluid in a shell-and-tube heat exchanger with twisted tape. Eng Anal Bound Elem 2023;147:1–10. https://doi.org/10.1016/J.ENGANABOUND.2022.11.024.

[124] Chen K, Seo D, Canteenwalla P. The Effect of High-Temperature Water Vapour on Degradation and Failure of Hot Section Components of Gas Turbine Engines. Coatings 2021, Vol 11, Page 1061 2021;11:1061. https://doi.org/10.3390/COATINGS11091061.

[125] Najafi SBN, Mokhov A V, Levinsky HB. Investigation of the stability, radiation, and structure of laminar coflow diffusion flames of CH4/NH3 mixtures. Combust Flame 2022;244:112282. https://doi.org/10.1016/J.COMBUSTFLAME.2022.112282.

[126] Hayakawa A, Goto T, Mimoto R, Kudo T, Kobayashi H. NO formation/reduction mechanisms of ammonia/air premixed flames at various equivalence ratios and pressures. Mechanical Engineering Journal 2015;2:14–402. https://doi.org/10.1299/MEJ.14-00402.

[127] Zitouni S-E, Mashruk S, Mukundakumar N, Brequigny P, Zayoud A, Pucci E, et al. Ammonia blended fuels–energy solutions for a green future. 10th International Gas Turbine Conference, 2021.

[128] Glarborg P, Miller JA, Ruscic B, Klippenstein SJ. Modeling nitrogen chemistry in combustion. Prog Energy Combust Sci 2018;67:31–68. https://doi.org/10.1016/J.PECS.2018.01.002.

[129] Tu Y, Xu S, Liu H. Combustion and emission characteristics of NH3/CH4/air in a model swirl combustor: Comparison between premixed and non-premixed modes. Int J Hydrogen Energy 2023;48:17311–23. https://doi.org/10.1016/J.IJHYDENE.2023.01.235.

[130] Zhang M, An Z, Wang L, Wei X, Jianayihan B, Wang J, et al. The regulation effect of methane and hydrogen on the emission characteristics of ammonia/air combustion in a model combustor. Int J Hydrogen Energy 2021;46:21013–25. https://doi.org/10.1016/J.IJHYDENE.2021.03.210.

[131] Wang G, Liu X, Li P, Shi G, Si J, Liu Z, et al. Influence of the H2 proportion on NH3/H2/air combustion in hot and low-oxygen coflows. Int J Hydrogen Energy 2024;63:480–90. https://doi.org/10.1016/J.IJHYDENE.2024.03.212.

[132] Intergovernmental Panel on Climate Change (IPCC). AR6 Synthesis Report: Climate Change 2023 2023. https://www.ipcc.ch/report/sixth-assessment-report-cycle/ (accessed May 20, 2025).

[133] Kim JH, Kim TW, Kim YH, Kwon OC. Combustion characteristics of premixed ammonia-hydrogen/air swirl flames at elevated pressure. Int J Hydrogen Energy 2024;74:423–33. https://doi.org/10.1016/J.IJHYDENE.2024.06.134.

[134] Vigarinho de Campos D, Guiberti TF, Es-sebbar E touhami, Lacoste DA. Effects of reactants stratification and pre-heating on the stabilization and emissions of partially cracked ammonia swirl flames. Proceedings of the Combustion Institute 2024;40:105231. https://doi.org/10.1016/J.PROCI.2024.105231.

[135] Zhang K, Shen YZ, Palulli R, Ghobadian A, Nouri J, Duwig C. Combustion characteristics of steam-diluted decomposed ammonia in multiple-nozzle direct injection burner. Int J Hydrogen Energy 2023;48:16083–99. https://doi.org/10.1016/J.IJHYDENE.2023.01.091.

[136] Li Z, Li S. Effects of inter-stage mixing on the NOx emission of staged ammonia combustion. Int J Hydrogen Energy 2022;47:9791–9. https://doi.org/10.1016/J.IJHYDENE.2022.01.050.

[137] Zhou J, Duan F. Kinetic modeling and emission characteristics of multi-staged partially cracked ammonia/ammonia-fueled gas turbine combustors. Int J Hydrogen Energy 2025;122:44–56. https://doi.org/10.1016/J.IJHYDENE.2025.03.162.

[138] Somarathne KDKA, Okafor EC, Hayakawa A, Kudo T, Kurata O, Iki N, et al. Emission characteristics of turbulent non-premixed ammonia/air and methane/air swirl flames

through a rich-lean combustor under various wall thermal boundary conditions at high pressure. Combust Flame 2019;210:247–61. https://doi.org/10.1016/J.COMBUSTFLAME.2019.08.037.

[139] Cafiero M, Dias V, Iavarone S, Coussement A, Jeanmart H, Parente A. Investigation of temperature correction methods for fine wire thermocouple losses in low-pressure flat premixed laminar flames. Combust Flame 2022;244:112248. https://doi.org/10.1016/J.COMBUSTFLAME.2022.112248.

[140] Kramers H. Heat transfer from spheres to flowing media. Physica 1946;12:61–80. https://doi.org/10.1016/S0031-8914(46)80024-7.

[141] Dasch CJ. One-dimensional tomography: a comparison of Abel, onion-peeling, and filtered backprojection methods. Applied Optics, Vol 31, Issue 8, Pp 1146-1152 1992;31:1146–52. https://doi.org/10.1364/AO.31.001146.

[142] Clees S, Rault TM, Zaczek LT, Hanson RK. Simultaneous OH and OH∗ measurements during NH3 oxidation in a shock tube. Proceedings of the Combustion Institute 2024;40:105286. https://doi.org/10.1016/J.PROCI.2024.105286.

[143] Shi X, Lian T, Zhang Y, Liu Z, Li W, Xi Z, et al. Enhanced ammonia combustion by partial pre-cracking strategy in a gas turbine model combustor: Flame macrostructures, lean blowout characteristics and exhaust emissions. Applications in Energy and Combustion Science 2024;17:100247. https://doi.org/10.1016/J.JAECS.2024.100247.

[144] Monge-Palacios M, Zhang X, Morlanes N, Nakamura H, Pezzella G, Sarathy SM. Ammonia pyrolysis and oxidation chemistry. Prog Energy Combust Sci 2024;105:101177. https://doi.org/10.1016/J.PECS.2024.101177.

[145] Valera-Medina A, Morris S, Runyon J, Pugh DG, Marsh R, Beasley P, et al. Ammonia, Methane and Hydrogen for Gas Turbines. Energy Procedia 2015;75:118–23. https://doi.org/10.1016/J.EGYPRO.2015.07.205.

[146] Valera-Medina A, Gutesa M, Xiao H, Pugh D, Giles A, Goktepe B, et al. Premixed ammonia/hydrogen swirl combustion under rich fuel conditions for gas turbines operation. Int J Hydrogen Energy 2019;44:8615–26. https://doi.org/10.1016/J.IJHYDENE.2019.02.041.

[147] Wang G, Guiberti T, Roberts W. Exploring the Effects of Swirl Intensity on NO Emission in Ammonia-Methane-Air Premixed Swirling Flames. Journal of Ammonia Energy 2023;1. https://doi.org/10.18573/JAE.14.

[148] Chen D, Li J, Li X, Guo Y, Huang H, Kobayashi N. Experimental studies on the OH∗ chemiluminescence and structure characteristics in NH3/H2 and NH3/cracked gas swirl flames. Int J Hydrogen Energy 2024;52:1370–9. https://doi.org/10.1016/J.IJHYDENE.2023.06.185.

[149] Zitouni S, Bréquigny P, Mounaïm-Rousselle C. Turbulent partially cracked ammonia/air premixed spherical flames. Fuel Communications 2024;20:100126. https://doi.org/10.1016/J.JFUECO.2024.100126.

[150] Su T, Xu B, Bastiaans RJM, Worth NA. Lean Blow-Off Behaviour of Premixed Bluff-Body Stabilized Hydrocarbon-Air Flames and Ammonia/Hydrogen/Nitrogen-Air Flames. J Eng Gas Turbine Power 2024;146. https://doi.org/10.1115/1.4065908/1201481.

[151] Su T, Xu B, Bastiaans RJM, Worth NA. The behaviour of NH3/H2/N2, CH4 and C3H8 turbulent premixed bluff-body stabilized flames near lean blow-off. Proceedings of the Combustion Institute 2024;40:105739. https://doi.org/10.1016/J.PROCI.2024.105739.

[152] Vanierschot M, Van den Bulck E. Hysteresis in flow patterns in annular swirling jets. Exp Therm Fluid Sci 2007;31:513–24. https://doi.org/10.1016/J.EXPTHERMFLUSCI.2006.06.001.

[153] Holemans T, Yang Z, De Greef J, Vanierschot M. Swirl-induced hysteresis in a sudden expansion flow. Physics of Fluids 2024;36:105193. https://doi.org/10.1063/5.0231799/3318267.

[154] Singh NK, Ramamurthi K. Formation of Coanda jet from sharp-edged swirl nozzle with base plate. Exp Therm Fluid Sci 2009;33:675–82. https://doi.org/10.1016/J.EXPTHERMFLUSCI.2009.01.008.

[155] Cosway B, Talibi M, Balachandran R. Investigation of NO production and flame structures in ammonia-hydrogen flames. Journal of Ammonia Energy 2023:106–17. https://doi.org/10.18573/jae.20.

[156] Xing J, Pillai AL, Kurose R. Heat release rate surrogate for ammonia–hydrogen premixed flames under various conditions. Applications in Energy and Combustion Science 2023;15:100193. https://doi.org/10.1016/J.JAECS.2023.100193.

[157] Wei Y, Zhu X, Tian B, Zhou H, Issayev G, Cheng YB, et al. Excited Species as Heat Release Rate Markers in Laminar Premixed Ammonia-Hydrogen-Air Flames. Energy and Fuels 2024;38:11311–20. https://doi.org/10.1021/ACS.ENERGYFUELS.4C01501/ASSET/IMAGES/LARGE/EF4C01501_0012.JPEG.

[158] Zhang M, Wei X, Wang J, Huang Z, Tan H. The blow-off and transient characteristics of co-firing ammonia/methane fuels in a swirl combustor. Proceedings of the Combustion Institute 2021;38:5181–90. https://doi.org/10.1016/J.PROCI.2020.08.056.

[159] Rieth M, Gruber A, Chen JH. A direct numerical simulation study on NO and N2O formation in turbulent premixed ammonia/hydrogen/nitrogen-air flames. Proceedings of the Combustion Institute 2023;39:2279–88. https://doi.org/10.1016/J.PROCI.2022.07.266.

[160] Chi C, Han W, Thévenin D. Effects of molecular diffusion modeling on turbulent premixed NH3/H2/air flames. Proceedings of the Combustion Institute 2023;39:2259–68. https://doi.org/10.1016/J.PROCI.2022.08.074.